Optical Meta-structures for Exceptional Points, Bound States in the Continuum, and Polarization Control

Haoye Qin

Electrical Engineering and Computer Sciences
University of California, Berkeley

May 1, 2023

Acknowledgement

Optical Meta-structures for Exceptional Points, Bound States in the Continuum, and Polarization Control

by Haoye Qin

Research Project

Submitted to the Department of Electrical Engineering and Computer Sciences, University of California at Berkeley, in partial satisfaction of the requirements for the degree of **Master of Science, Plan II**.

Approval for the Report and Comprehensive Examination:

Committee:

Boubacar Kante
Boubacar Kante (Nov 23, 2021 16:11 PST)

Professor Boubacar Kante
Research Advisor

Nov 23, 2021

* * * * * * *

Professor Connie Chang-Hasnain
Second Reader

Nov 29, 2021

Optical Meta-structures for Exceptional Points, Bound States in the Continuum, and
Polarization Control

by

Haoye Qin

A thesis submitted in partial satisfaction of the

requirements for the degree of

Master of Science

in

Electrical Engineering and Computer Sciences

in the

Graduate Division

of the

University of California, Berkeley

Committee in charge:

Professor Boubacar Kante, Co-chair
Professor Connie Chang-Hasnain, Co-chair

Fall 2021
Delay publication until May 2023

Optical Meta-structures for Exceptional Points, Bound States in the Continuum, and
Polarization Control

Abstract

Optical Meta-structures for Exceptional Points, Bound States in the Continuum, and Polarization Control

by

Haoye Qin

in Electrical Engineering and Computer Sciences

University of California, Berkeley

Professor Boubacar Kante, Co-chair

Professor Connie Chang-Hasnain, Co-chair

Optical nanostructures like high contrast gratings and metasurfaces have received increasing interests for their capability in tailoring wave propagation with optical flatness. Basics optical properties (amplitude, phase, and polarization) can be effectively tuned and controlled by a designed nanostructures, which is beneficial for applications in science and engineering. Here we investigate the optical metasurfaces for realization of bound states in the continuum (BICs) and exceptional points (EPs), and employ the polarization selective feature in high contrast grating to reach high performance linear and circular polarizers. Optical BICs are demonstrated in enhancing optical forces, chirality, nonlinear harmonics generation, and nonlinear chirality. Optical EPs are explored with eigenmodes and transmission matrix, and proposed to improve sensitivity in refractive index change and gyroscopes. Silicon nitride HCG and metal grating are designed and verified for polarization generation and control.

Contents

List of Figures

Acknowledgments

I would like to express my gratitude to my advisors, Prof. Boubacar Kante and Prof. Constance J. Chang-Hasnain, for their support and guidance over the one and a half years. I am impressed by their devotion in both science and technology. It is a pride and a privilege to have ever been their student. I would also like to thank Dr. Walid Redjem, Zhetao Jia, Yipeng Ji, Xiangli Jia, Yertay Zhiyenbayev, Mingyue Guan, and Mutasem Odeh. I likewise thank the members from Kante group and Prof. Chang's group.

I am leaving halfway. A master degree at Berkeley is not what I firstly expected. While witnessing the dramatic changes along with COVID-19 and bilateral relation, it suddenly appears to me that life is not supposed to be a well-planned routine. Try to be open-minded, seek new opportunities, and reshape the unexpected experience.

Chapter 1

Introduction

General periodic nanostructures include 1D periodic grating [1] and 2D periodic metasurface or plasmonics meta-structure [2]. The grating is periodic along x direction with infinite length in y direction, while metasurface has a unit cell that repeats infinitely in both x and y direction. In order to modeling periodic nanostructures, periodic boundary condition is introduced in simulation assuming an infinite repeat for the specific unit cell. Periodic boundary condition allows one to calculate the response of the entire system by only simulating one unit cell. Computational methods include finite difference time domain (FDTD) and finite element method (FEM), with representative demonstrations in Lumerical Solutions and COMSOL Multiphysics, respectively. Basically, FDTD solves Maxwell's curl equations in non-magnetic materials [3]:

$$\frac{\partial D}{\partial t} = \nabla \times H$$

$$D(\omega) = \epsilon_0 \epsilon_r(\omega) E(\omega)$$

$$\frac{\partial H}{\partial t} = -\frac{1}{\mu_0} \nabla \times E$$

where H, E, and D are the magnetic, electric, and electric displacement fields, respectively. $\epsilon_r(\omega)$ is the relative frequency-dependent dielectric constant. In three dimensions, Maxwell equations have six electromagnetic field components which can be analysed under TE (transverse electric), and TM (transverse magnetic) conditions. For TM case, Maxwell's equations reduce to

$$\frac{\partial D_z}{\partial t} = \frac{\partial H_y}{\partial z} - \frac{\partial H_x}{\partial y}$$

$$D_z(\omega) = \epsilon_0 \epsilon_r(\omega) E_z(\omega)$$

$$\frac{\partial H_x}{\partial t} = -\frac{1}{\mu_0} \frac{\partial E_z}{\partial y}$$

$$\frac{\partial H_y}{\partial t} = -\frac{1}{\mu_0} \frac{\partial E_z}{\partial x}$$

In FDTD method, "Yee lattice" is used to discretize Maxwell's equations in space, involving the placement of electric and magnetic fields on a staggered grid. The FDTD method solves these equations on a discrete spatial and temporal grid. Each field component is solved at a slightly different location within the grid cell (Yee cell, Figure 1.1). The resulting finite-difference equations are solved in a leapfrog manner: at first the electric field components are solved at a given time in a specific volume of space; then in the same spatial volume the magnetic field components are solved at the next step in time; and the process is repeated over and over again until the electromagnetic field within the settled time and space is fully evolved. In Lumerical Solution, FDTD solver runs and reconstructs the equation and simulation data automatically, and thus the user does not have to deal with the physics during usage.
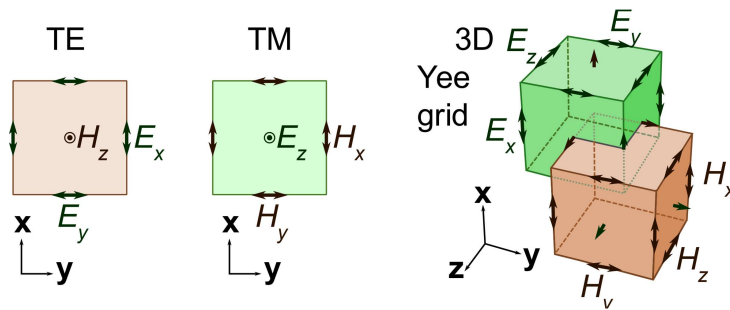
Figure 1.1: A "Yee lattice" involving electric and magnetic fields can be used to discretize Maxwell's equations in space. In three dimensions, the lattice consists of a multiplicity of Yee cells. Reproduced under a Creative Commons Attribution (CC BY) license [4]. Copyright 2015.

The finite element method (FEM) is a widely used method for numerically solving space- and time-dependent problems that are usually given in terms of partial differential equations (PDEs). Assume a function u is dependent variable in a PDE. The function u can be approximated by a function u_h using linear combinations of basis functions $u \simeq u_h = \sum_i u_i \psi_i$, where ψ_i is the the basis function and u_i is the coefficient. The benefit of FEM method is that the discretization can be uniform or nonuniform [5], offering great freedom in the selection of discretization (Figure 1.2).

Gratings and metasurfaces with subwavelength thickness enable manipulation of wave propagation and a spatially varying optical response like amplitude, phase, and polarization [6]. These advantages have contributed to various applications:

- Arbitrary phase gradient and beam forming

- Polarization conversion and control

- Nonlinearity and harmonic generation

- Optical chirality, asymmetric transmission, and nonreciprocity

- Wave guidance and radiation

- Active and tunable metasurfaces

- Thermal-optics and heat transfer

- Quantum optics and photonics

Especially, high contrast gratings have been extensively employed as broadband reflector in vertical-cavity surface-emitting lasers due to its high performance and reduced thickness [1, 7]. Holography and metalens take advantage of tunable phase gradient and amplitude from designed metasurface [8, 9]. Birefringence metasurface can serve as linear and circular polarizers with arbitrary input state [10]. With nonlinear metarials at hand, enhanced harmonic generation [11] and nonlinear hologram are explored using bound state in the continuum and Pancharatnam-Berry (PB) phase [12]. Plasmonics and dielectric metasurfaces have revealed three-dimensional chirality and nonlinearity induced nonreciprocity [13]. Thriving investigations are going into electrically-tunable metasurfaces and thermal effect in plasmonics metasurfaces [14].
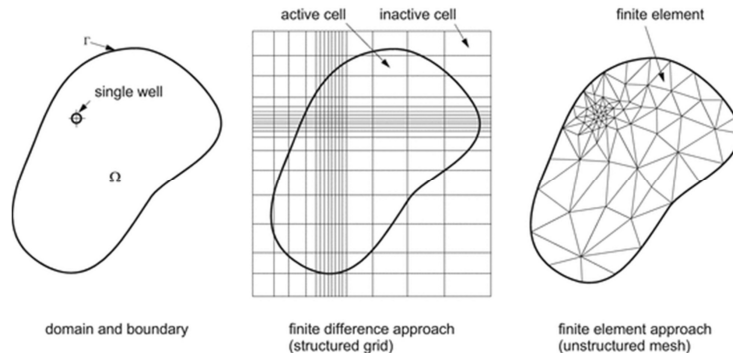
Figure 1.2: Comparison between discretization and mesh used in FDTD and FEM. Used with permission from [5] copyright 2013 by Springer Nature

This thesis will focus on demonstrations and applications of exceptional points (EPs), bound states in the continuum (BICs), and polarization control using both all-dielectric and plasmonics metasurfaces (high contrast gratings). Chapter 2 will introduce optical BICs and applications of BICs to enhanced optical forces, chirality, and nonlinearity. Chapter 3 will discuss different arrangements for realizing exceptional points in eigenmodes via coupled modes and transmission matrix. It will also involve hybrid modes where plasmonics and photonics modes are coupled to form BICs and EPs. In Chapter 5 and Chapter, HCGs are designed to work as a flat-optics, high performance linear and circular polarizers. Nanofabrication of HCGs are included in Chapter 5.

Chapter 2

Optical bound state in the continuum

2.1   Bound state in the continuum for trapping waves

In 1929, von Neumann and Wigner showed that Schrödinger's equation can have bound states above the continuum threshold , which is called bound states in the continuum (BICs), showing resonances without decay [15]. For several decades afterwards the idea lay dormant, regarded primarily as a mathematical curiosity. BICs arise naturally from Feshbach's quantum mechanical theory of resonances, and are thus more physical than initially realized. Recently, it was realized that BICs are intrinsically a wave phenomenon and are thus not restricted to the realm of quantum mechanics. They have since been shown to occur in many different fields of wave physics including acoustics, microwaves and nanophotonics. The seminal work demonstrating trapped light was presented by Chia Wei Hsu and coworkers [16]. The PhC slab supports guided resonances where the frequencies lie within the continuum of radiation modes in free space. These resonances typically have infinite lifetime and thus infinite quality factor. While at the k point, light becomes perfectly confined in the slab with quality factor reaching infinity. They verify and demonstrate this photonics BIC with experiments, FDTD simulation, and coupled mode theory. By changing incident angle on the slab, radiative quality factor can be tuned from infinite to finite, opening intense investigation on BICs in the linear wave phenomenon. In meta-optics and nanophotonics associated with BICs, nanoparticle resonators and metasurfaces receive great attention [17]. Quasi-BICs in isolated subwavelength nanoparticles have been explored by employing the mode coupling between Mie-like mode and Fabry–Pérot mode [18]. In-plane symmetry and broken symmetry in periodic structures result in BIC and quasi-BIC with very high quality factor and enhanced field localization [19], contributing to improving optical chirality and nonlinear harmonic generation. It's exciting to observe the formation of BIC in hybrid plasmonic-photonic systems, where lossy plasmonics mode is pushed towards BIC with increasing quality factor [20]. Recently, BIC is also realized in an open acoustic resonator for sound trapping, extending BIC to the acoustic wave [21].

2.2   Tunable and enhanced optical force with QBIC

Light-actuated motors, vehicles, and even space sails have drawn tremendous attention for practical and exciting applications in space exploration, biomedical, and sensing. Optical bound state in the continuum (BIC) is known to be capable of trapping light and improving light-matter interaction. Herein, we propose an incorporation of BIC for generation of enhanced and tunable optical forces and torques in metasurfaces. A sharp lineshape is observed in forces and torques spectrum when approaching BIC mode induced by the high-Q resonance. Wavelength and polarization tunability are also illustrated for sensitive direction switch associated with BIC.

The concept of bound state in the continuum (BIC) has attracted considerable interest for its ability of trapping waves inside the continuum without radiation loss1. First proposed in quantum mechanics, BIC has been observed in various wave phenomenon from optics and acoustics to water and elastic waves. Especially, the emerging periodic optical platforms such as metasurfaces, gratings, and photonics crystal enable practical demonstrations and applications of BIC, which provides a simple avenue for realizing high-Q resonances. Symmetry-protected bound states have been demonstrated in coupled waveguide array, photonics crystal slab, waveguides coupled to resonators, and dielectric spheres. Lasing action from an optically pumped BIC cavity have enabled arbitrarily high Q factors with directional output and single-mode operation. There is also formation of BIC in lossy plasmonics system, such as the hybrid plasmonics-photonics system with a plasmonics grating coupled to dielectric optical waveguide8, and the anisotropic plasmonics metasurfaces governed by BIC collective resonant modes. In practice, Fano-like quasi-BIC mode with a broken in-plane symmetry in all-dielectric metasurfaces shows extending applications for enhancement of nonlinear effects, biosensing, and lasing. Recently, the concept of BIC is enriched with chirality to break the limitation of linear polarizations and provide chiral engineering. It's well known that light can exert forces and torques as illustrated in optical tweezers [22] and particle-trapping devices [23]. Metasurfaces provide unprecedented opportunities to engineer and manipulate light, thus leading to the conception of light-based propulsion for space travel, i.e., laser and solar-driven spacecraft [24, 25]. Recently, novel studies on optical force contribute to the proposal of meta-vehicles [26], plasmonics motors [27, 28], self-stabilizing photonics structure for levitation and propulsion, and lightsails, which rely on asymmetric scattering of light [24]. However, there still lack demonstrations on metasurfaces enabled large tunibility and enhancement of optical forces and torques, which is beneficial for building up effective light vehicles/motors/sails with full controllability via properties of incident light.

Therefore, in this section, focusing on the need of the two features, a distinctive quasi-BIC feature is used to enhance the generation of optical forces and torques with highly tuning capability, which aims at providing controllable and improved optical manipulation and new design method of meta-motors or vehicles. The quasi-BIC is formed through introducing an asymmetry ratio between two coupled dielectric particles, and the calculated optical force and torque show significant enhancement. By controlling wavelength and/or polarization of

the incident light, generated force and torque can switch direction and intensity, which is useful for on-demand all-optical manipulation.
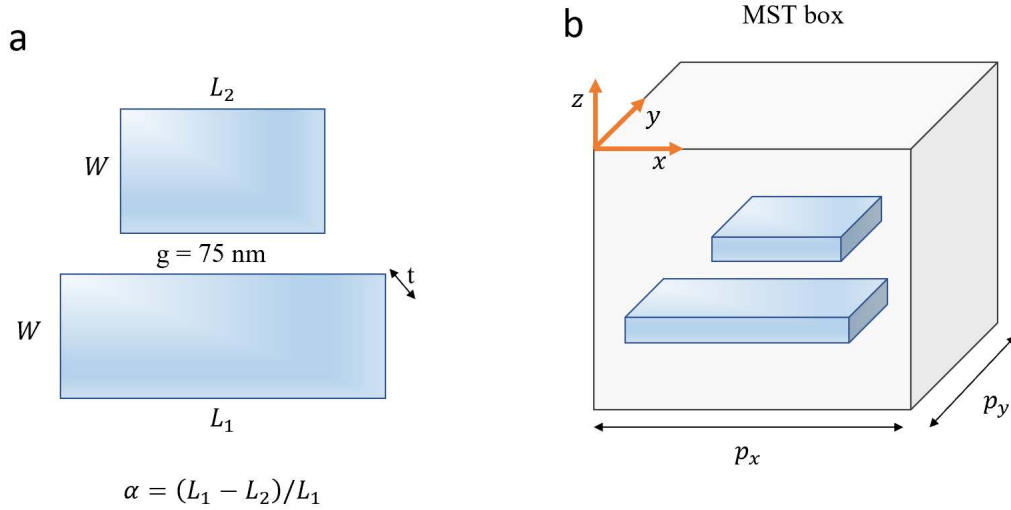
Figure 2.1: Schematic of the proposed coupled particles showing BIC mode for enhanced optical force. (a) Top view of the asymmetric silicon bars with length L_1 (fixed at 280 nm) and L_2. Both bars have width W of 200 nm. The gap between them g is 75 nm and thickness t is 250 nm. The asymmetry ratio α is defined as $(L_1 - L_2)/L_1$. (b) Simulation domain for calculating the optical force and torque. The stress tensor is integrated over the boundary of the Maxwell stress tensor (MST) box. Periodic boundary condition is applied in x and y direction with a lattice constant $p_x = 200$ nm and $p_y = 530$ nm respectively.

The designed metasurface unit-cell for quasi-BIC mode is shown in Figure 2.1. Two silicon bars with the same width (200 nm) and length L_1 (fixed at 280 nm) and L_2 are placed in free space. The gap is 75 nm and thickness 250 nm. Periodic boundary condition is applied in x and y direction. L_2 can be tuned to get different asymmetry ratio which is defined as $\alpha = (L_1 - L_2)/L_1$. When $\alpha = 0$, both bars have the same length the in-plane symmetry is fulfilled, and a BIC mode is present. Reducing the length of the one bar breaks this symmetry and a quasi-BIC mode will appear with a sharp spectral resonance. To investigate the optical force and torque associated with the high-Q quasi-BIC mode, we employ a method of integrating the Maxwell stress tensor (MST) around a box enclosing the unit cell (Figure 2.1(b)). The expressions for calculating time-averaged force and torque are given by [29]

$$F = (T \cdot \hat{n}) \, dA \tag{2.1}$$

$$Tor = r \ \times \ (T \cdot \hat{n}) \, dA \tag{2.2}$$

where S is the surface of the MST box, $\hat{n}$ is the unit vector normal to the surface, r is the position vector regarding the original point. T is the stress tensor with its elements defined as $T_{ij} = \epsilon_0 \left(E_i E_j - \frac{1}{2} |E|^2 \delta_{ij} \right) + \frac{1}{\mu_0} \left(B_i B_j - \frac{1}{2} |B|^2 \delta_{ij} \right)$, where E_i and B_i is the ith component of the electric and magnetic field respectively which can be obtained by solving the electric and magnetic fields with a conventional method. All numerical electromagnetic simulations were performed using the commercial finite-element-method solver COMSOL Multiphysics.

Figure 2.2 illustrates the optical characterization of the metasurface with two asymmetric particles as a unit cell. In Figure 2.2(a), the evolution of transmission spectrum is shown for different asymmetry ratio. As anticipated, at $\alpha = 0$, in-plane symmetry produces BIC mode with disappeared linewidth. Increasing α leads first to a sharp resonance dip (grey square marker) that keeps degrading, broaden and blue-shifted wavelength. Figure 2.2(b) shows the exponentially decreasing Q factor of the collective mode extracted with a rational fit method for the complex S_{21} parameter. An interesting phenomenon accompanied with the "visible" collaborative quasi-BIC mode is that two individual quasi-BIC modes have emerged. The latter two modes can be seen in the enlarged view of the spectrum (Figure 2.2(c)), featuring sharp lineshape but poor transmission. They arise from the in-plane symmetry of individual particle instead of the two interactive particles and are then perturbed by the mode coupling to reveal quasi-BIC feature. The individual mode 2 is more responsive in resonant wavelength than the individual mode 1 because the length of one the bar is reduced, thus increasing its resonant frequency, while the other is kept unchanged. Electric and magnetic field profiles for individual mode 1 and 2 plotted in Figure 2.2(d) confirm this explanation with a mode localization in only one particle. Figure 2.2(e) shows the near-field distributions of the electric and magnetic fields for the collaborative quasi-BIC mode in a unit cell with an asymmetry ratio of 0.05, where the strongly confined profile indicates a high-Q resonance. It is named as a collaborative mode as there is a clear interaction between the two resonant particles.

In Figure 2.3, a clear enhancement of optical forces F_x and F_y assisted by the high-Q resonance of quasi-BIC mode is shown when the structure is in small asymmetry. In addition to the significant enhancement, tunability can be achieved by sweeping the wavelength. Especially there exists a sharp peak switch from positive to negative F_y, which indicates a negative feedback region for the wavelength-force relation, offering improved controllability. This sensitive direction switch is attributed to the quasi-BIC mode.

Figure 2.4(a,b) demonstrates an enhancement of optical force generated from the collective mode in x and y direction with quasi-BIC mode. For instance, at $\alpha = 0.05$ the optical force is enhanced by over 10 times as compared to $= 0.20$. As asymmetry ratio increases, the optical force reduces exponentially. However, the forces coming from the individual modes 1 and 2 have no clear trend since they are not directly associated with the collaborative asymmetry. Tunability of optical forces can be achieved through varying wavelength and/or polarization of the incident light as shown in Figure 2.4(c,d). Around 1140 nm, 1075 nm, and 1055 nm, there is force enhancement, corresponding to the two individual modes and one collaborative mode. Changing the polarization from 0.5π (y polarization) to an angle of 0.3π and 0.1π results in a drop of the collective mode-induced force and an increase of force from individual modes. The direction of optical force can also be switched by tuning
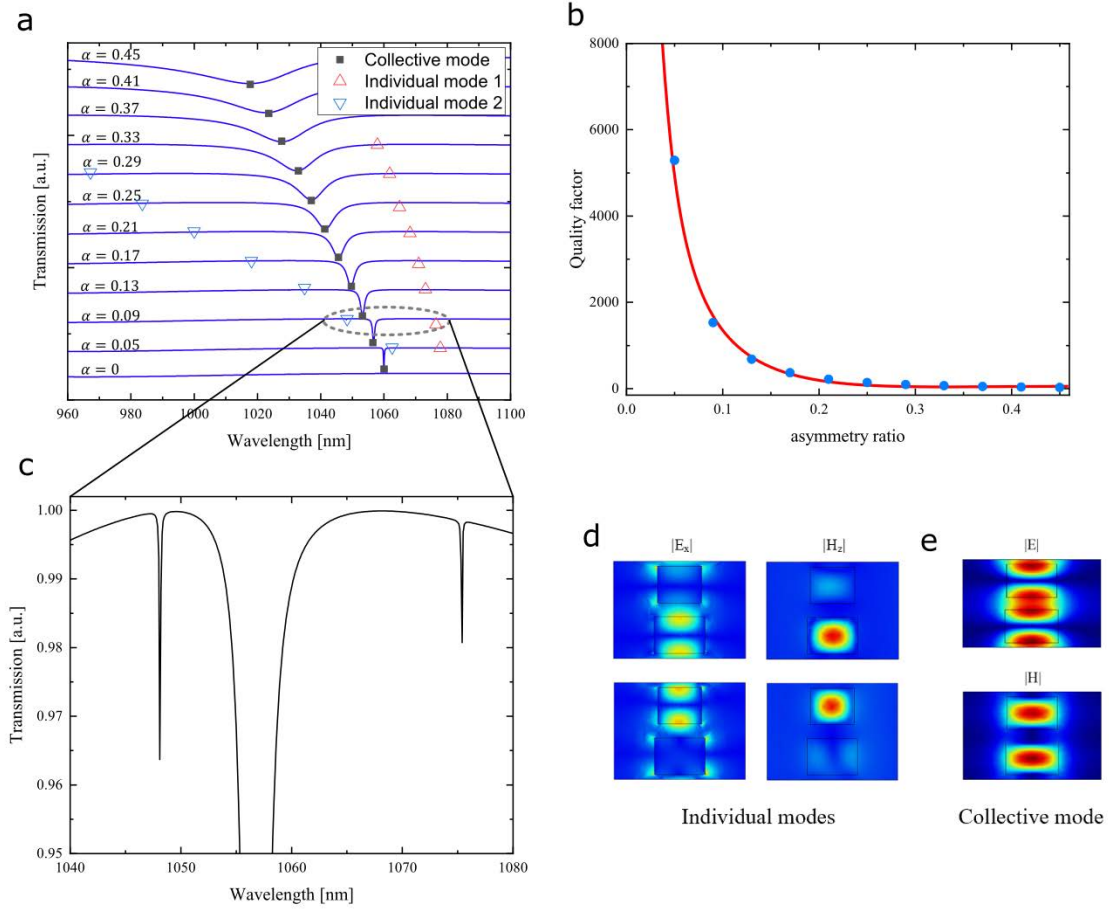
Figure 2.2: Optical characteristics of collaborative and individuals quasi-BIC modes. (a) Transmission spectrum for different asymmetry ratio. For $\alpha = 0$, there is no resonance dip. By breaking the in-plane symmetry, quasi-BIC modes reveal as observed in the spectrum (denoted as different markers). (b) Quality factor as a function of asymmetry ratio for the collective mode. The blue dots are the extracted quality factor through rational fitting. The red line is an exponential fit. A drop in Q factor is shown by increasing the asymmetry ratio. (c) Enlarged view of the two inappreciable individual BIC modes. Corresponding distribution of electric (d) and magnetic field (e) for individual BIC modes and for collective BIC mode, respectively. For individual modes field is localized in either the top or bottom particle.

the incident light wavelength.

Optical torque in z direction (Tor_z) is obtained from Eq.2. Figure 2.5(a) presents the enhanced optical torque from collaborative mode as a function of asymmetry ratio. A suppression is observed for $\alpha < 0.13$, which is attributed to the competition between the two
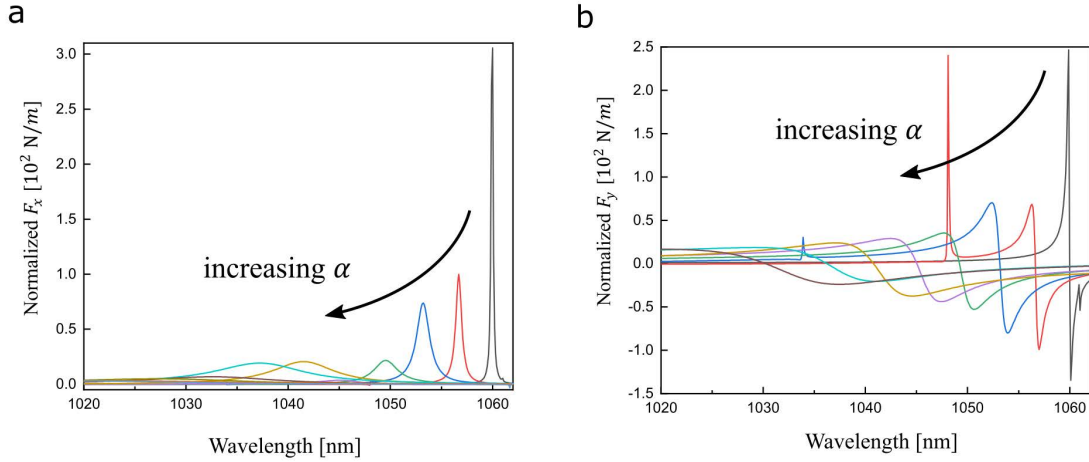
Figure 2.3: Optical force in x (a) and y (b) direction as a function of wavelength for different asymmetry ratios. The forces calculated from MST box are normalized to the period of the unit cell.

individual modes as illustrated by their crossing (Figure 2.2(a)). The torque enhancement is still significant at $\alpha = 0.13$. In Figure 2.5(b), Tor_z as a function of wavelength is plotted for different values. Two peaks on the side, whose positions agree well with the dips in transmission spectrum, again originate from the individual modes. The center peak degrades with an increasing , although direction of the torque switches. The direction of the forces can be tuned with the asymmetry ratio, wavelength, and polarization angle (Figure 2.5(c)), enabling a full control of the structure's rotation and angular position. The effect of circular polarized light (LCP, RCP) is evaluated in Figure 2.5(d). In addition to the peaks induced by quasi-BIC modes, there is a smooth wavelength region where the torque is stable. For the collaborative mode, a switch from LCP to RCP also symmetrically switches the direction of the torque, hence the direction of rotation.

A practical design with 20×20 unit cell and glass substrate added to the quasi-BIC element is proposed and verified. The finite size structure incorporates a bottom layer of glass $0.5\mu m$ thick and previously studied asymmetric particles with asymmetry ratio of 0.09. Simulated transmission of Figure 2.6(a) shows a quasi-BIC resonance dip corresponding to a Q-factor of 1135, which is comparable with the Q-factor previously extracted from an infinite structure which is 1528 (Figure 2.2(b)). Figure 2.6(c) shows the enhancement and tunability of optical forces and torque as expected. For this quasi-BIC enhanced metasurface as an optical motor in water, due to the large aspect ratio (∼20:1) for parallel surface and frontal area, the friction drag coefficient is considered as the total drag coefficient CD, which can be estimated from the local skin coefficient. Under Laminar flow approximation,
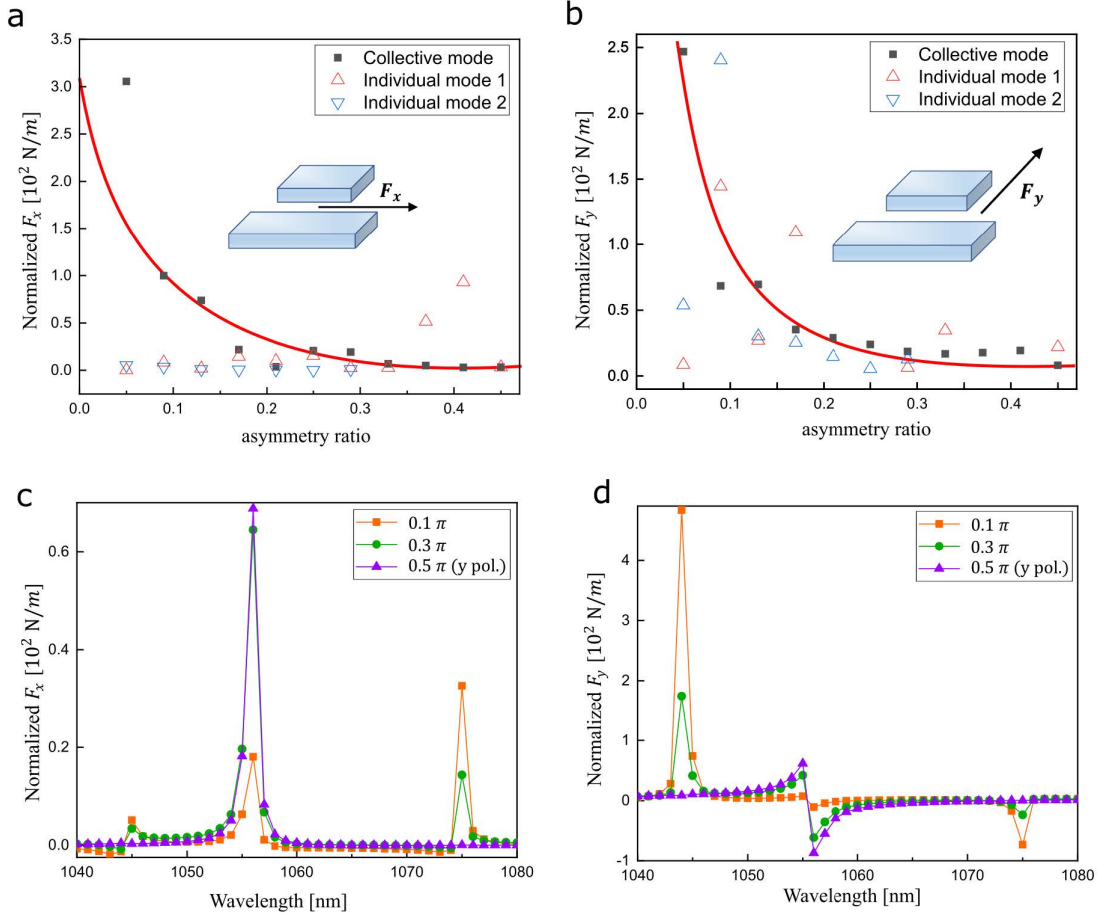
Figure 2.4: On-resonance optical force for the three BIC modes. Normalized optical force in x direction F_x (a) and in y direction F_y (b). Different modes are plotted with different markers. Blue squares indicate the collaborative mode tuned via asymmetry ratio, where an exponential decrease of optical force is observed. (c,d) Optical force F_x and F_y with $\alpha = 0.13$ for different polarization of incident light. The optical force can be switched from positive to negative value via tuning the incident light wavelength and force intensity via polarization angle.

$$C_D = \frac{1}{bL} \int_0^L 0.664 \left(\frac{U}{\nu}\right)^{-0.5} x^{-0.5} b dx = 1.33 \left(\frac{\upsilon}{UL}\right)^{0.5} \tag{2.3}$$

or,

$$C_D = \frac{1.33}{\sqrt{Re_L}} \tag{2.4}$$
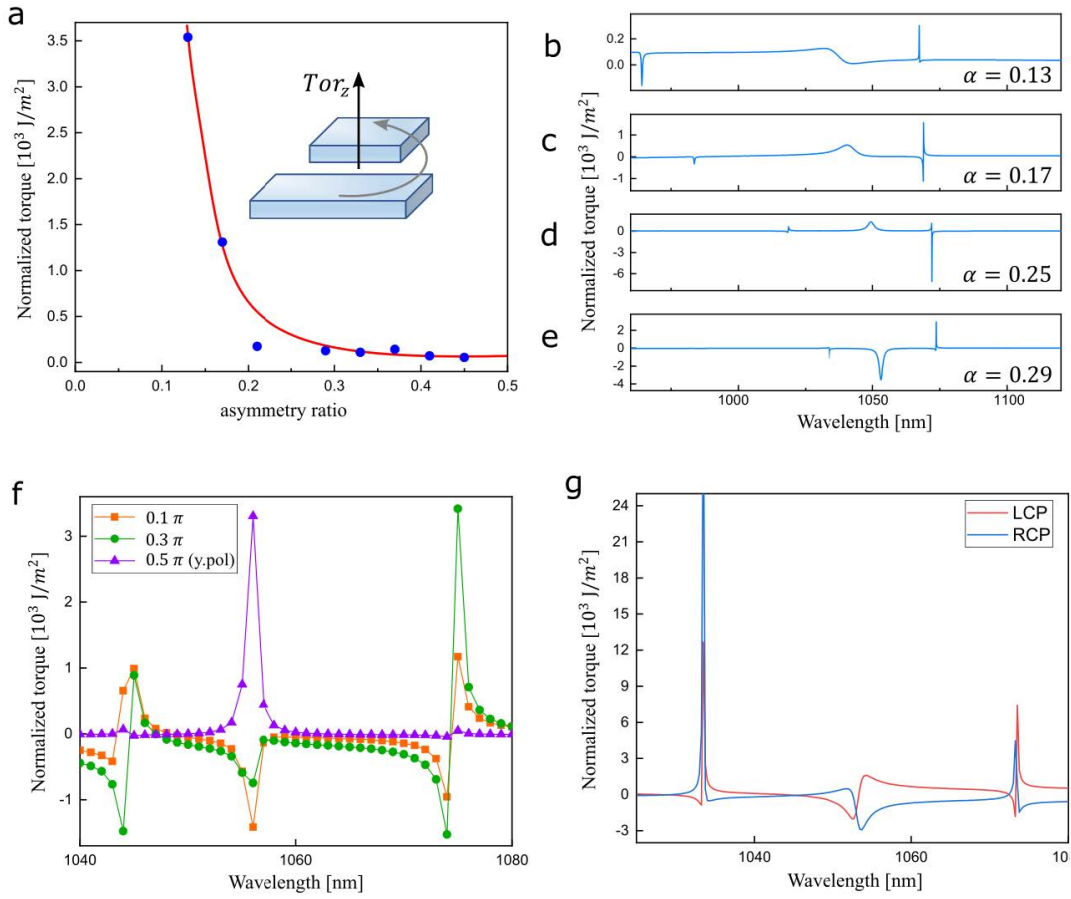
Figure 2.5: Generated optical torque in z direction. (a) Normalized Tor_z as a function of asymmetry ratio, where an enhancement is shown at $\alpha = 0.13$. Inset: schematic shows the optical torque and its direction. (b) Tor_z as a function of wavelength for $\alpha = 0.13$, 0.17, 0.25 and 0.29. The central peak corresponds to the collective modes. (c) Torque for different polarization angles. (d) Evaluation of optical torque under left and right circular polarized light.

where $Re_L = \frac{UL}{v}$ is called Reynolds number, and U, L, b, ν represents the flow velocity, length, depth of the metasurface, and kinematic viscosity of the flow, respectively. Especially, for water at room temperature, $\nu = 8.917 \times 10^{-7} m^2/s$ results in $Re_L = 16.26U$ and $C_D = \frac{0.3798}{\sqrt{U}}$ for propulsion in y direction. To allow for other drag effects under real experiments, the final drag coefficient is multiplied by an additional drag ratio. Assuming a balanced force at final state, the achieved velocity per illumination intensity with optical propulsion in y direction is shown in Figure 2.6(d) for different addition ratios at peak optical force. Figure 2.6(d) plots the velocity per illumination intensity as a function of wavelength at the
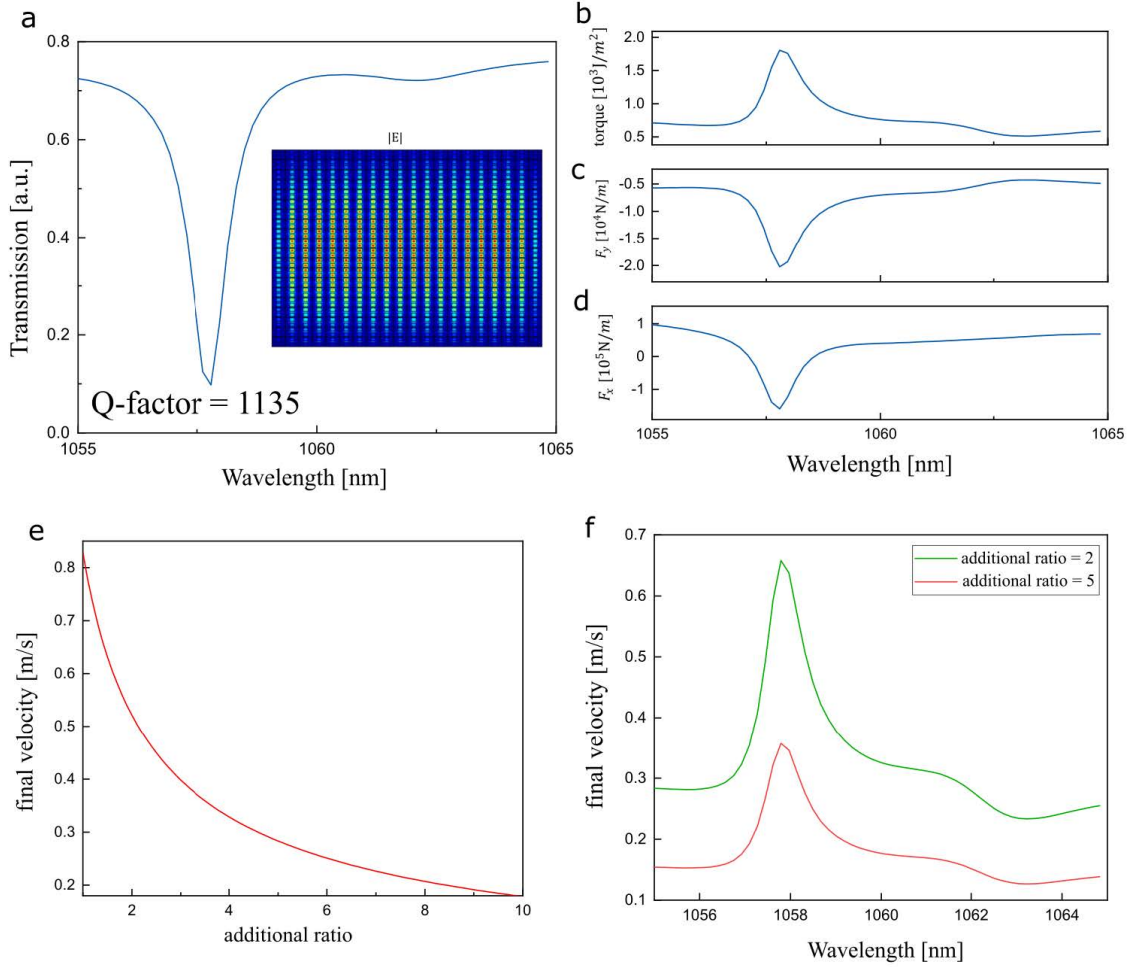
Figure 2.6: Proposed meta-motor on glass substrate. (a) Transmission spectrum from finite-size simulation showing a Q factor of 1135. Inset shows the electric filed distribution of the corresponding high-Q mode present in the transmission spectrum. (c) Calculated optical force and torque from finite-size simulation. (d) Estimated final-state velocity per illumination intensity for propulsion in y direction as a relation of additional ratio for the drag coefficient. (e) Estimated final-state velocity per illumination intensity for propulsion in y direction as a relation of wavelength with additional ratio of 2 (top) and 5 (bottom).

additional ratio of 2 and 5.

In conclusion, we have presented the incorporation of quasi-BIC mode into metasurface for enhancement of optical forces and torques with large tunability. By changing the asymmetry of two-bar structure, high-Q quasi-BIC mode can be revealed showing enhanced force in x, y direction and torque in z direction. Along with this enhancement, wavelength

and polarization tuning of force (torque) direction and amount can be realized. Hence, the proposed metasurface may contribute to on-demand control of light vehicles/motors/sails for applications in space exploration, medical, sensing, and actuators by only modulating properties of incident light.

2.3   Enhanced harmonic generation and circular dichroism at QBIC

Periodic cylinder pattern has been demonstrated to reveal BIC with InGaAsP [30] and perovskite [31] for lasing and quasi-BIC (QBIC) with AlGaAs for enhanced second harmonic generation and low-threshold optical self-switching [32]. In this section, evaluation is conducted on nonlinear harmonic generation and chirality related to QBIC. It's noteworthy that the chirality, characterized by circular dichroism (CD), is not limited to the fundamental response against circular polarizations, but second-harmonic CD and third-harmonic CD. The greatly enhanced field localization at QBIC leads to enhanced linear CD, harmonic generation, and nonlinear CD.
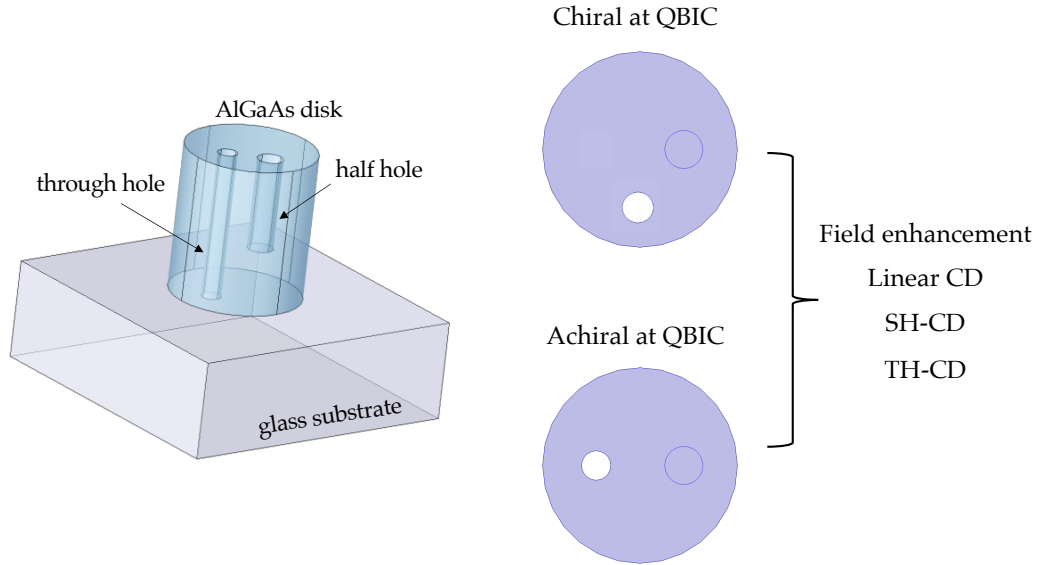
Figure 2.7: Unit cell of the AlGaAs metasurface consisting of a disk and two asymmetric air holes. The height of the through hole is equal to the height of the disk, and the height of the half hole is half the height of the disk. Periodic condition is applied in x and y direction. By changing the relative angle of the two holes, chiral and achiral state can be reached with QBIC. The chiral QBIC results in enhanced harmonic generation and enhanced linear and nonlinear CD.

The QBIC under investigation follows the AlGaAs cylinder design due to its large non-linear coefficient (Figure 2.7). The cylinder is placed on the top of glass substrate. In simulation, AlGaAs and glass are modeled as lossless material with index of 3.2 and 1.5, and periodic boundary condition is applied in x and y direction with a lattice constant of 550 nm. Two asymmetric air holes are etched in the disk, and chiral effects can be observed when their relative angle is not equal to 180°. And at exactly 180°, CD will vanish. Without insertion of air hole, the metasurface of AlGaAs disks shows typical Lorentz dip and unobservable BIC mode. The through air hole is added to induced symmetric breaking effect of the BIC mode, resulting in QBIC, as plotted in Figure 2.8(a). The sharp Fano-like lineshape indicates the occurrence of QBIC. However, the structure is now still achiral showing the same response to excitation of LCP and RCP light. Therefore, a half hole is employed to introduce chirality. With x polarized light, red line in Figure 2.7(a) shows that the half hole does not form QBIC but instead shifts the resonance frequency with 28 nm.
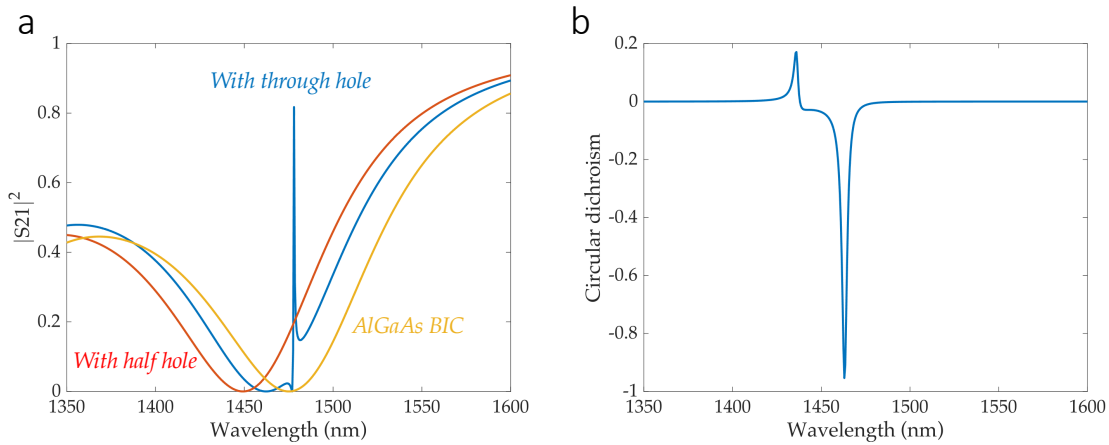
Figure 2.8: (a) Amplitude of S21 without holes (orange), with only through hole (purple), and with only the half hole (red). The input polarization is in x direction. (b) Circular dichroism from linear simulation as a function of wavelength.

After observing the QBIC induced by through hole and frequency shift induced by half hole, optical chirality of this design is examined with CD, which can be defined as the transmission difference between LCP and RCP input, explicitly, $CD = (T_{RCP} - T_{LCP})/(T_{RCP} + T_{LCP})$ [33]. Figure 2.8(b) shows the enhancement of CD at QBIC, where a sharp dip reaches -0.95. The peak at smaller wavelength is due to the Lorentz resonance. The position of the QBIC related CD peak is not the same as the peak in Figure 2.8(a), since QBIC is shifted by the additional half hole. The wavelength difference is about 28 nm, agreeing well with the Lorentz dip shift.

The large local electric field enhancement at QBIC and second-order nonlinear susceptibility $\chi^{(2)}$ contributes to efficient harmonic generation process. The cubic AlGaAs crystal
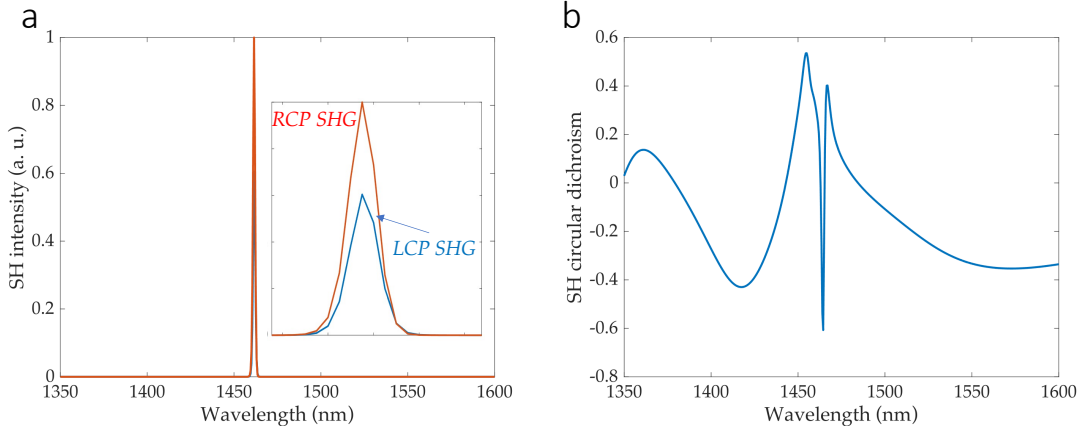
Figure 2.9: (a) Simulated SH intensity for RCP and LCP excitation. (b) SH circular dichroism as a function of fundamental wavelength.

belongs to the $\bar{4}3m$ symmetry group, which can be characterized by non-zero nonlinear tensor $\chi_{ijk}^{(2)} = \chi^{(2)}$ only when $i \neq j \neq k$ [34]. The value of $\chi^{(2)}$ is set as 200 pm/V. Then the second-order nonlinear polarization can be given as

$$P_i^{SHG}(2\omega) = \varepsilon_0 \chi_{ijk}^{(2)} \left[E_y E_z + E_x E_z + E_x E_y \right] \tag{2.5}$$

Since the SHG process is enhanced, SH filed will affect the fundamental field. Therefore, a coupled polarization $P_i(\omega)$ is involved to reflect this coupling when conducting linear simulation.

The simulated SH signal is plotted in Figure 2.9(a) at fundamental wavelength with the structure in a chiral state (Figure 2.7). Giant enhancement of SH intensity is observed at the QBIC wavelength for the excitation of both LCP and RCP light. Also, as expected, SHG from LCP and RCP is different, leading to nonlinear CD (SH-CD) in Figure 2.9(b). A sharp change shows in SH-CD spectrum at the QBIC position, with the value reaching -0.6.

While for the case of THG, only four tensor elements are independent, and all nonzero components of the $\chi^{(3)}$ tensor are assigned the value of 10^{-19} m^2/V^2. Then the third-order nonlinear polarization can be given as [35]

$$P_i^{THG}(3\omega) = \varepsilon_0 [\chi_{iiii}^{(3)} E_i^3(\omega) + 3\chi_{iijj}^{(3)} E_i(\omega) E_j^2(\omega) + 3\chi_{iikk}^{(3)} E_i(\omega) E_k^2(\omega)] \tag{2.6}$$

where $i \neq j \neq k$ are the Cartesian components x, y, and z.

TH intensity is shown in Figure 2.10(a) for both LCP and RCP excitation, which also demonstrates the QBIC empowered THG. The discrepancy at QBIC between LCP and RCP is significantly larger than SH case, since for SH polarization only cross term like $E_x E_y$ is involved, while TH polarization has the involution term like E_x^3. Figure 2.10(b) plots the
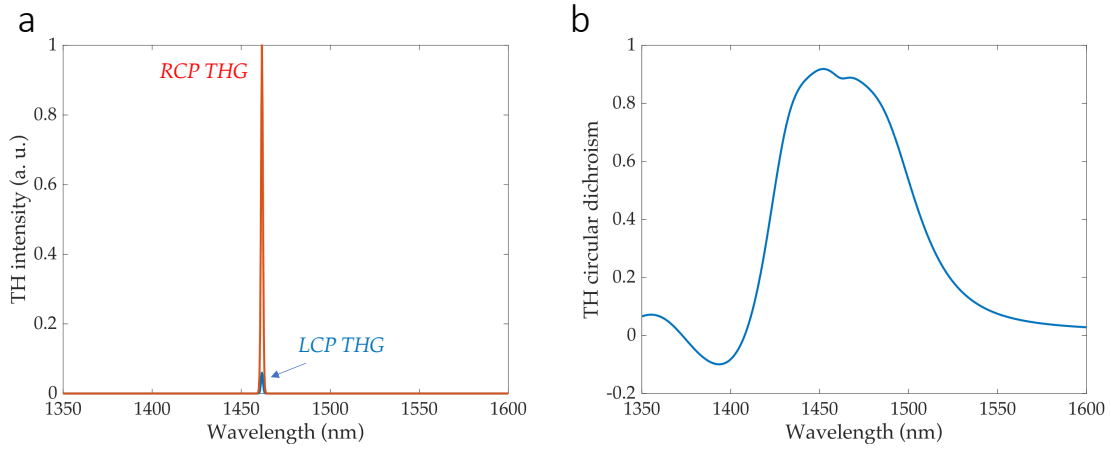
Figure 2.10: (a) Simulated TH intensity for RCP and LCP excitation. (b) TH circular dichroism as a function of fundamental wavelength.
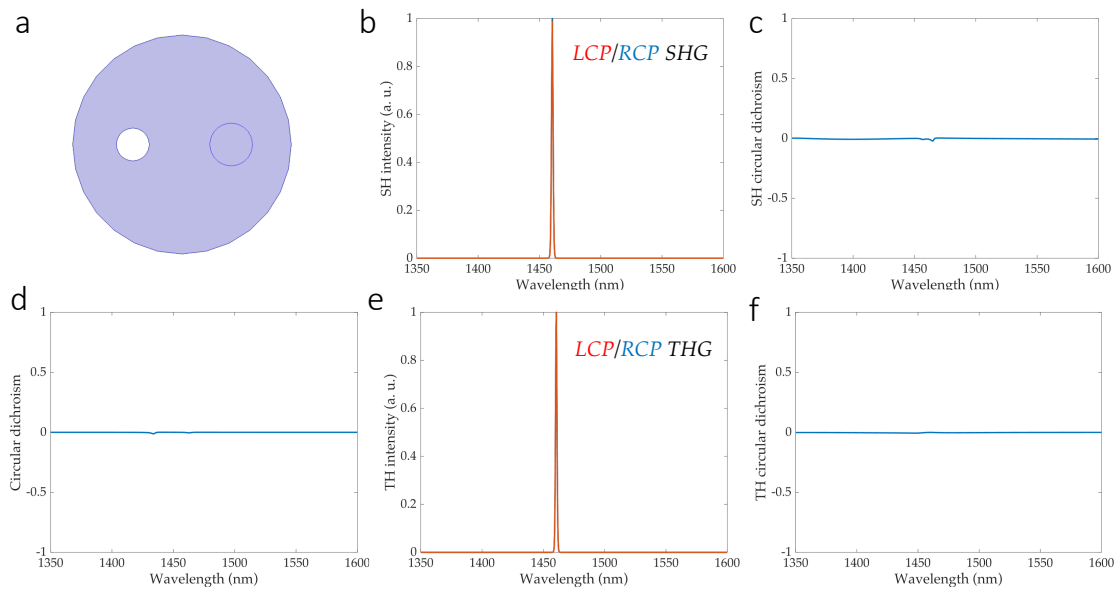
Figure 2.11: (a) Achiral state at QBIC (b) SH intensity and (e) TH intensity from RCP and LCP excitation. (c) SH-CD and (f) TH-CD as a function of the fundamental wavelength.

TH-CD, and the chirality enhancement is shown to appear in a large range around QBIC. The maximum TH-CD approaches as large as 0.94.

Hence, the metasurface consisting of AlGaAs disks with chiral feature at QBIC verify the QBIC-enhanced linear CD, harmonic generation, and nonlinear CD.

This QBIC can also be converted to achiral state by rotating the relative angle of two holes to 180°(Figure 2.11(a)). Under this condition, CD is near zero at QBIC in Figure 2.11(d). Although QBIC enhanced SHG and THG is observed in Figure 2.11(b,e), the intensity coming from LCP and RCP excitation is the same, resulting in near-zero SH-CD and TH-CD (Figure 2.11(c,f)).

With this metasurface composed of AlGaAs disks and asymmetric air holes, QBIC at chiral and achiral state can be realized. Nonlinear process like SHG and THG is enhanced greatly at the QBIC wavelength. At chiral state, linear CD, SH-CD and TH-CD are also observed with enhancement.

2.4   Plasmonics BIC with Al cylinder in InGaAsP disk

In 2017, the first demonstration of BIC laser is reported with InGaAsP multiple quantum wells cylindrical nanoresonator array suspended in air [15]. Single-mode lasing for various radii and array sizes is achieved to demonstrate the scalability and robustness of this new kind of microlasers. This mechanism is then employed to possess vortex behaviors with different topological charges with ultrafast control using perovskite metasurface [31]. In the following, BIC mode in the cylindrical nanoresonator array is firstly evaluated, and then modification is involved to realized plasmonics BIC for new possibility of a plasmonics BIC lasers.
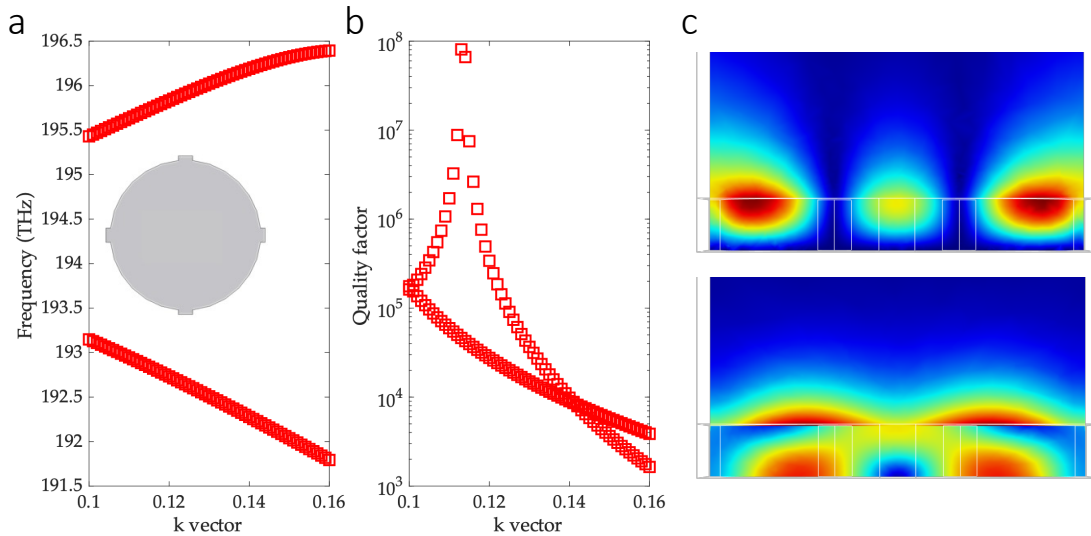
Figure 2.12: Realization of photonics BIC. (a) Frequency and (b) quality factor obtained from eigenfrequency simulation. Inset in (a) shows top view of this design. (c) Corresponding field profile at k = 0.154 for the high-Q (top) and low-Q (bottom) mode.

Inset of Figure 2.12(a) shows the unit cell design of the first-reported BIC laser, where the cylinder is made of InGaAsP with a refractive index of 3.4. Eigenfrequency simulation is conducted to obtain the frequency and corresponding quality factor, as plotted in Figure 2.12(a,b). Around k = 0.154, quality factor of one mode goes to infinity, indicating the existence of a BIC mode. Figure 2.12(c) shows the electrical field distribution for the high-Q (top) and low-Q (bottom) mode at the BIC point.
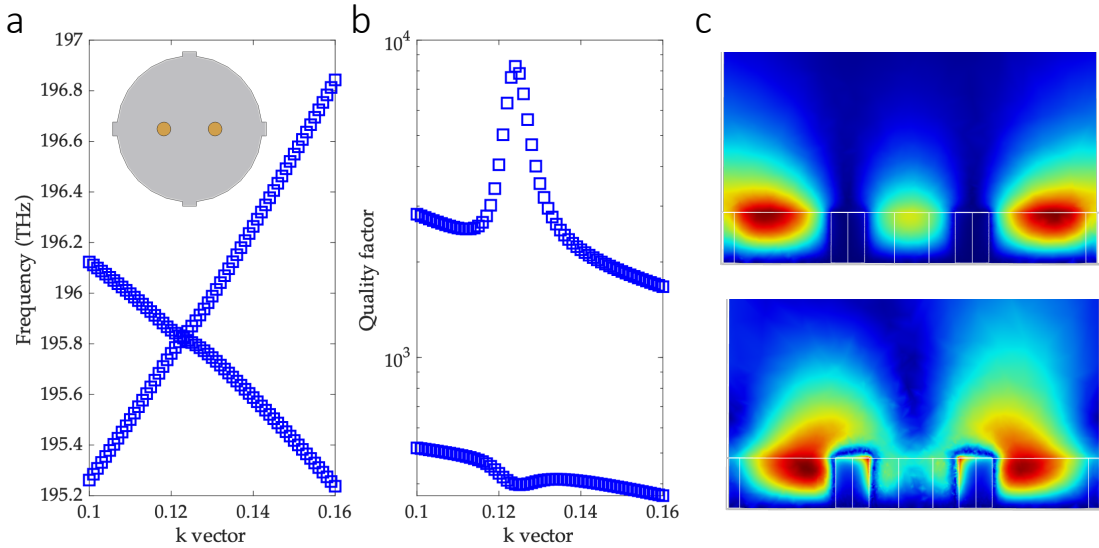
Figure 2.13: Realization of photonics quasi-BIC. (a) Frequency and (b) quality factor obtained from eigenfrequency simulation. Inset in (a) shows top view of this design. The metal cylinder is made of gold, with a radius of 50 nm and separation of 185 nm. (c) Corresponding field profile k = 0.126 for the high-Q (top) and low-Q (bottom) mode.

For the purpose of plasmonics BIC, metal materials need to be involved within this photonics design. Initially, two gold nanocylinders are inserted in the InGaAsP. Perfect electrical conduction is applied to evaluate only the TM mode. The resultant eigenfrequencies and corresponding Q factor is shown in Figure 2a,b. In contrast to Figure 2.12, the maximum Q factor is reduced, and its position is shifted towards a larger k vector. The Q factor does not increase to infinite since the slope become smoother as approaching the climax. An inspection of the mode profile in Figure 2.13(c) indicates that. The low-Q mode is plasmonics mode, and the high-Q mode is photonics mode. Therefore, this design can be understood as that the introduction of two gold cylinders perturbs original BIC in Figure 1, leading to the photonics quasi-BIC mode rather than forming plasmonics BIC.

This explanation is verified by changing the size of the metal cylinder. With the k vector of 0.154, a smaller cylinder radius can result in larger quality factor. When the radius is 0, it corresponds to the photonics BIC mode.
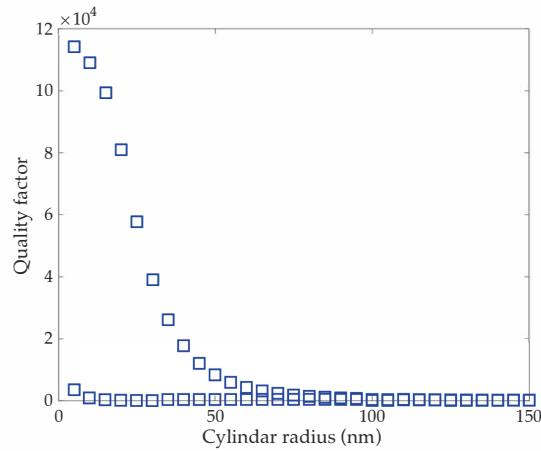
Figure 2.14: Quality factor as a function of cylinder radius at k = 0.154.
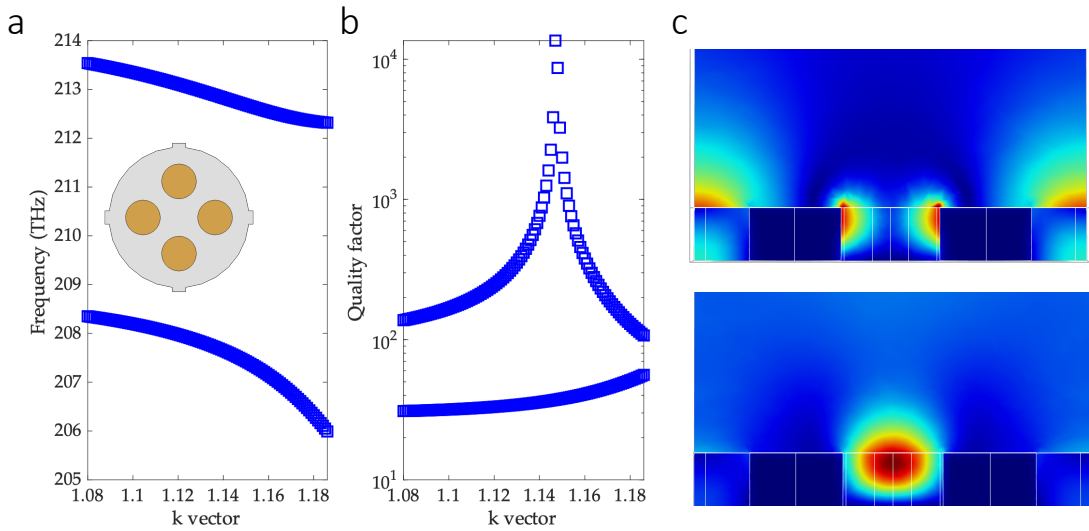
Figure 2.15: Realization of TM plasmonics BIC. (a) Frequency and (b) quality factor obtained from eigenfrequency simulation. Inset in (a) shows top view of this design. The metal cylinder is made of aluminum, with a radius of 130 nm and separation of 270 nm. The four cylinders are centrosymmetric. (c) Corresponding field profile k = 0.147 for the high-Q (top) and low-Q (bottom) mode.

Due to the failure of realizing plasmonics BIC with two gold nanocylinders, a new design with four symmetric aluminum nanocylinders is proposed, as shown in the inset of Figure 2.15(a). Perfect electrical conduction is applied to evaluate only the TM mode. Eigenfre-

quencies and Q factor are plotted in Figure 2.15(a,b), respectively. The main difference between Figure 2.13 and Figure 2.15 is that in Figure 2.15 the Q factor goes to infinity with nearly infinite slope, indicating a BIC mode. To verify its plasmonics nature, Figure 2.15(c) shows the mode profiles. Top panel corresponds to the high-Q mode, and it's related to the plasmonics mode. Bottom panel is the low-Q photonics mode. Therefore, TM plasmonics BIC is achieved in this design.
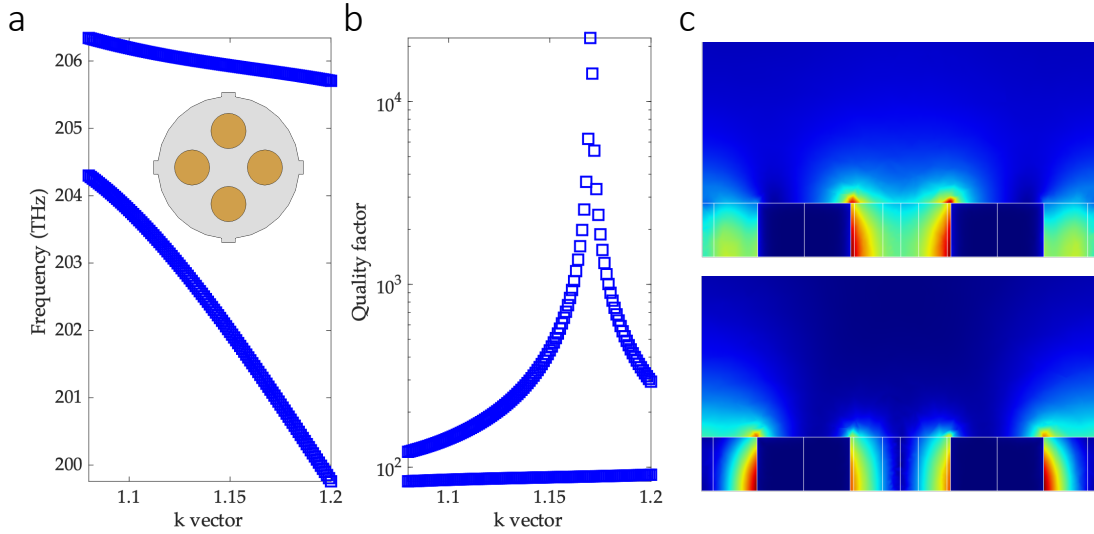
Figure 2.16: Realization of TE plasmonics BIC. (a) Frequency and (b) quality factor obtained from eigenfrequency simulation. Inset in (a) shows top view of this design. The metal cylinder is made of aluminum, with a radius of 130 nm and separation of 270 nm. The four cylinders are centrosymmetric. (c) Corresponding field profile k = 1.17 for the high-Q (top) and low-Q (bottom) mode.

While for the TE mode, perfect magnetic conduction is applied. Results from eigenfrequency simulation are shown in Figure 2.16(a,b). When k vector is equal to 1.17, BIC mode emerges with Q factor going towards infinity. An inspection of mode profiles at this point shows that this BIC is related with the plasmonics mode, leading to TE plasmonics BIC.

By simply inserting 4 centrosymmetric aluminum bars into InGaAsP multiple quantum wells cylindrical nanoresonator, plasmonics BIC for both TM and TE can be realized. This finding may contribute to research and development of the plasmonics BIC microlasers and applications of hybrid modes.

Chapter 3

Optical exceptional point

3.1 Basis and demonstrations of exceptional points

The past few years have seen the development of non-Hermitian optics [36] and the introduction of promising physical systems, which contribute to both theoretical and experimental demonstration of parity-time ($\mathcal{PT}$) symmetry, anti-$\mathcal{PT}$ symmetry, and exceptional points (EPs) [37]. As a distinctive candidate for exploring lightmatter interaction, optical whispering gallery mode (WGM) resonators have been employed to realize EPs by either tuning the gainloss ratio or manipulating backscattering [38]. Regarding the latter method, precisely tuning two external nanoparticles evanescently coupled with optical resonators can push the counter-propagating modes to the vicinity of EP [39].

The basics of EP can be understood from the coupled mode theory for a two-level system, with the dynamics equation given as

$$\frac{d}{dt} = -i \begin{pmatrix} \omega_1 - i\gamma_1 & \kappa \\ \kappa & \omega_2 - i\gamma_2 \end{pmatrix} \begin{pmatrix} a_1 \\ a_2 \end{pmatrix}$$

where ω is the resonance frequency of the two coupled modes, κ is the coupling coefficient, and γ is their decay rate. Eigenvalues of the 2×2 Hamiltonian are $\omega_\pm = \omega_0 - iA \pm \sqrt{\kappa^2 + B^2}$, where $\omega_0 = (\omega_1 + \omega_2)/2$, $A = (\gamma_1 + \gamma_2)/2$, and $B = [\omega_1 - \omega_2 + i(\gamma_1 - \gamma_2)]/2$. The two eigenvalues can be tuned to coincide at a specific point, that is, exceptional point with the fulfilment of $\kappa^2 + B^2 = 0$. At an EP, the eigenvalues coincide in both real and imaginary parts, and also the eigenvectors become completely parallel. The fascinating features of pushing systems to EPs can be enhanced sensing capability [39, 40], enhanced nonlinearity [41], EP encircling induced mode conversion (dynamics) [42, 43], EP encircling induced phase change (steady) [44]. To start, EP sensors have enhanced response toward small perturbation due to square-root relation of the perturbation and response. EP sensors have been successfully demonstrated in temperature sensing with three coupled cavities at third-order EP [45], nanoparticle detection with counter-propagating modes in a single cavity [39, 46], laser gyroscopes for enhanced Sagnac effect [47, 48], and plasmonics metasurface for refractive index change [49].

EP encircling results in interesting mode conversion effect in coupled waveguides with modulated loss(gain). This extends to polarizer with EP encircling [50]. Recently, steady EP encircling has been utilized to decouple P-B phase between the conversion of circularly polarized lights, based on the encircling induced 2π phase change [44]. EP in optomechanics and quantum systems is also under exploration [51, 52].

3.2 L-shaped chiral metasurface revealing EPs and BICs in scattering matrix

Exceptional points and bound states in the continuum (BICs) are two distinctive conditions showing coalesced eigenvalues and lossless eigenstate. Here, we propose a single layer L-shape chiral metasurface that can reveal asymmetric EPs for forward and backward interrogation and BICs at the same time in the transmission matrix. Giant optical chirality is demonstrated with asymmetry transmission up to 58 dB for circular polarizations. This metasurface can also perform as a polarizer for elliptical polarizations by employing eigenpolarizations at the BIC condition.

Exceptional points (EPs) are spectral degeneracies appearing in an open system where two eigenstates and their corresponding eigenvalues of a non-Hermitian Hamiltonian coalesce. EP has led to a variety of intriguing phenomena, such as stopped light, improved sensing capability, enhanced nonlinear Purcell effect, and asymmetric mode conversion. EP may be directly achieved with balanced gain-loss arrangement in parity time ($\mathcal{PT}$) symmetry, and by tuning parameters of two lossy components. Specifically, the metasurface, based on its high designability and large capability of controlling wave propagation, provides a practical platform for realizing EP in transmission matrix. First experimental demonstration employs asymmetric loss in materials and split ring resonators to reach the EP coupling condition. On the other hand, bound states in the continuum (BICs) refer to waves remaining localized despite their existence with radiating waves that loss energy [15,16]. From the view of a 2-by-2 Hamiltonian, BIC occurs when one eigenvalue has zero imaginary part, implying a lossless eigenmode with infinity quality factor. Optical (quasi-) BIC modes have been applied to microlasers, chirality, nanoscale fingerprint sensing, empowering harmonic generation. In this section, an L-shaped chiral metasurface is presented for its capability of showing both asymmetric EPs and BICs in the transmission matrix. Large optical chirality is demonstrated for circular polarized light with asymmetric transmission up to 54 dB, and the revealed BIC can be employed to form polarizers for elliptical polarizations.

The EPs and BICs under investigation are demonstrated in the transmission matrix. With linear polarization basis, the matrix T_{lin} can be defined as $E_t = T_{lin}E_i$, where E_i, E_t are the incident and transmitted field amplitudes under normal incidence. Explicitly, T_{lin} is given as

$$T_{lin} = \begin{pmatrix} t_{xx} & t_{xy} \\ t_{yx} & t_{yy} \end{pmatrix} \tag{3.1}$$

and the subscript notation xy refers to input y polarization and output x polarization. By using LCP and RCP basis, the transmission matrix can be re-expressed as $T_{circ} = \begin{pmatrix} t_{LL} & t_{LR} \\ t_{RL} & t_{RR} \end{pmatrix} = \Lambda T_{lin}\Lambda^{-1}, where \Lambda = \frac{1}{\sqrt{2}}\begin{pmatrix} 1 & 1 \\ i & -i \end{pmatrix}$ is the conversion matrix, t_{RR}, etc., hold similar meaning as element in T_{lin}.
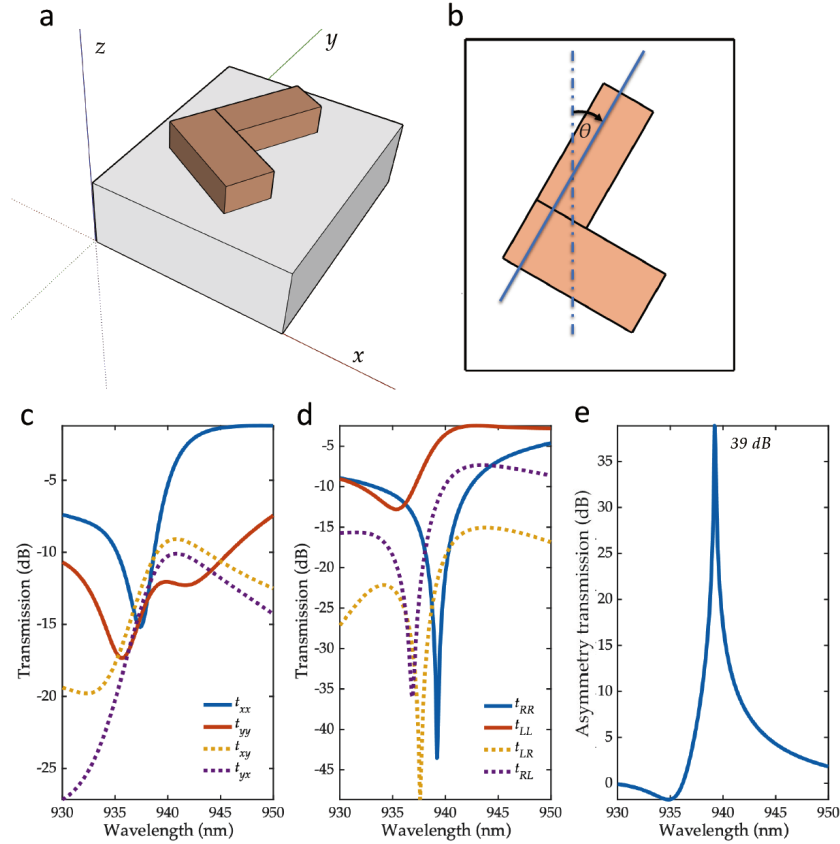
Figure 3.1: (a) Schematic of the L shaped metasurface with periodic condition in x and y direction. (b) Layout shows the orientation angle θ with regard to y axis. (c) Transmission of the four terms in Jones matrix under linear polarization basis, circular polarization basis and corresponding asymmetry transmission for LCP and RCP.

Figure 3.1(a,b) show the unit cell layout of the L-shaped chiral metasurface with the silicon "L" placed on a glass substrate. The unit cell is periodic in x and y direction, with a lattice constant of 700 nm. The "L" is orientated at an angle of θ with regard to the y axis, and with a thickness of 250 nm, the two rectangular elements have a width and length of 200 nm, 93 nm, and 280 nm, 250 nm, respectively. Scattering properties of this structure can be characterized with typical Jones matrix, with a basis of either linear polarizations or circular polarizations. Four terms in Jones matrix with linear polarization basis are measured in

Figure 3.1(c) when the angle θ is at 58°. It's important to note that the structure has unequal off-diagonal terms, i.e., $t_{xy} \neq t_{yx}$, which indicates an asymmetric feature since the oriented "L" is not mirror-symmetry and the thickness is not optically flat. To illustrate chirality of this structure, the polarization basis is changed to circular one, as shown in Figure 3.1(d). Large difference of transmission for RCP and LCP light can be observed, and the corresponded circular dichroism (CD) is plotted in Figure 3.1(e), demonstrating that the highest CD reaches 39 dB around 940 nm. The conversion from LCP to RCP and RCP to LCP are also asymmetric and exhibits dips at different wavelengths. Therefore, the orientated "L" structure reveals the both chiral and asymmetric features.
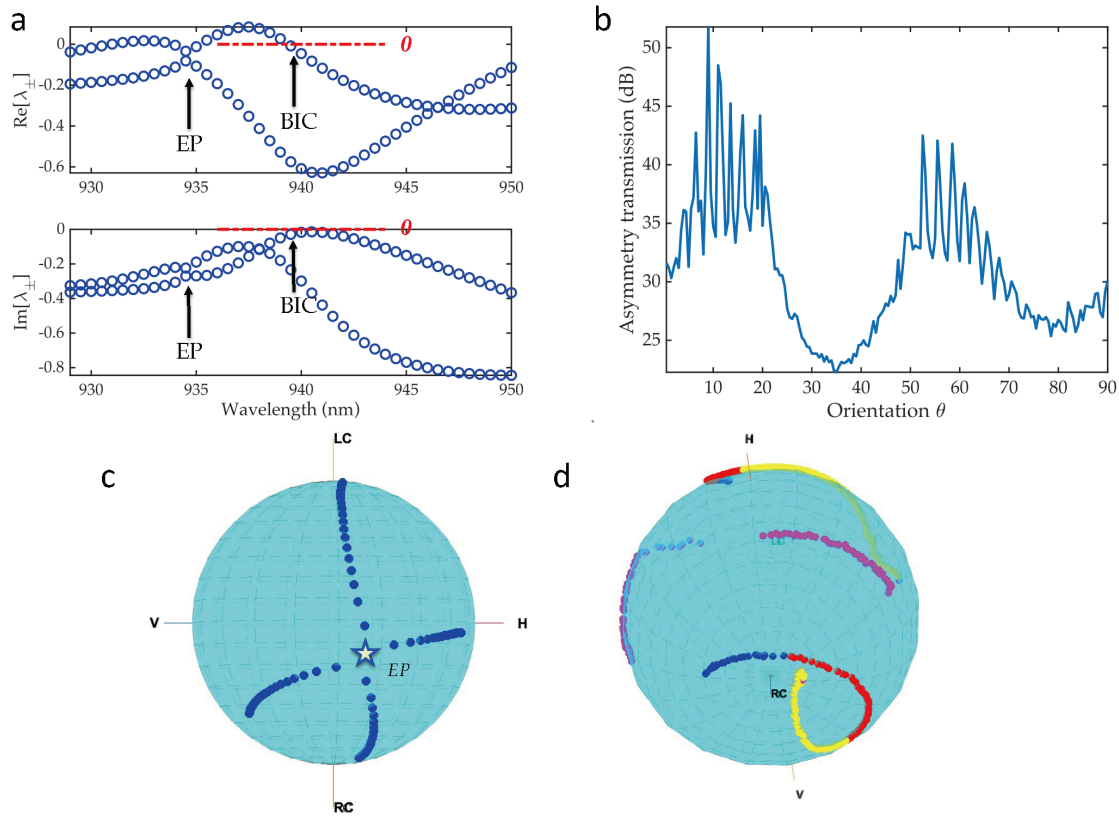
Figure 3.2: (a) Eigenvalue spectrum for real (top) and imaginary (bottom) part. Position of EP and BIC is marked with arrow. (b) Evolution of asymmetry transmission for LCP and RCP versus orientation angle. (c) Eigenpolarizations near EP are plotted on a Poincare sphere as a function of wavelength. (d) Eigenpolarizations on a Poincare sphere at RCP resonance.

In Figure 3.2(a), by tuning the orientation angle to 58.5°, exceptional points and bound state in the continuum can be observed in the spectrum by calculating eigenvalues of the scattering matrix. EP condition is realized when real and imaginary parts of the eigenval-

ues become coalesced, while for the BIC, here we only focus on a specific case when one eigenvalue reaches zero in both real and imaginary parts, which is a non-resonant state for its eigenpolarization. In the eigenvalue spectrum, EP is located around 935 nm and BIC is located around 940 nm, where the dashed lines refer to the value of zero. There is another cross point in real eigenvalues and no crossing for the imaginary, analogue to the Fano resonance condition in the coupled-resonator model. The coalesced feature of EP can also be illustrated from the perspective of eigenpolarization. In Figure 3.2(c), the calculated eigenpolarizations are indicated by blue dots on a Poincare sphere, and the four arrays converge toward one EP point, denoted by a star marker. Chiral structure can be characterized with circular dichroism, and CD is highly dependent on the shape. Figure 3.2(b) demonstrates the maximum CD as a function of orientation angle. Although there exist several zigzag peaks, the main trend shows a periodic peak-valley profile when changing θ from 0 to 90 degrees. This can be explained by a close inspection of the eigenpolarizations corresponding to the maximum CD, as plotted in Figure 3.2(d). For the curve around RCP point, the blue part has an approaching trend to the RCP point, which is related with the first CD peak in 10~20 degrees. And the red section shows a leaving trend, therefore, the resonant condition for RCP becomes harder to reach, reducing the discrepancy between LCP and RCP transmission. Then the yellow section from 40 to 62 degrees evolves again towards the RCP point, agreeing well with the peak religion in the maximum CD plot. A transition happens for the end part, making the eigenpolarizations jump far away from the RCP point (pink curve), leading to the valley around 80°.
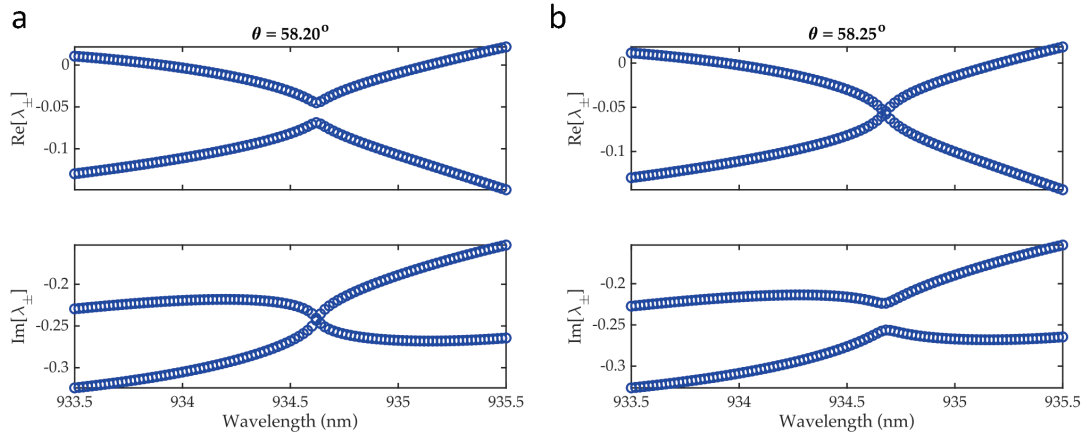
Figure 3.3: Verification of EP with crossing and anti-crossing. (a) At 58.20°, anti-crossing in real and crossing in imaginary. (b) At 58.25°, crossing in real and anti-crossing in imaginary.

EP can be further verified by observing switch in crossing and anti-crossing through modifying one parameter. In Figure 3.3(a), the orientation angle is 58.20°, real spectrum shows anti-crossing at 934.6 nm, and imaginary spectrum has the crossing feature. While

only by increasing angle to $58.25°$, the anti-crossing in real switches to imaginary, and crossing in imaginary changes to real (Figure 3.3(b)). Hence, EP unambiguously presents in the scattering matrix by simply rotating the L structure at a certain angle.
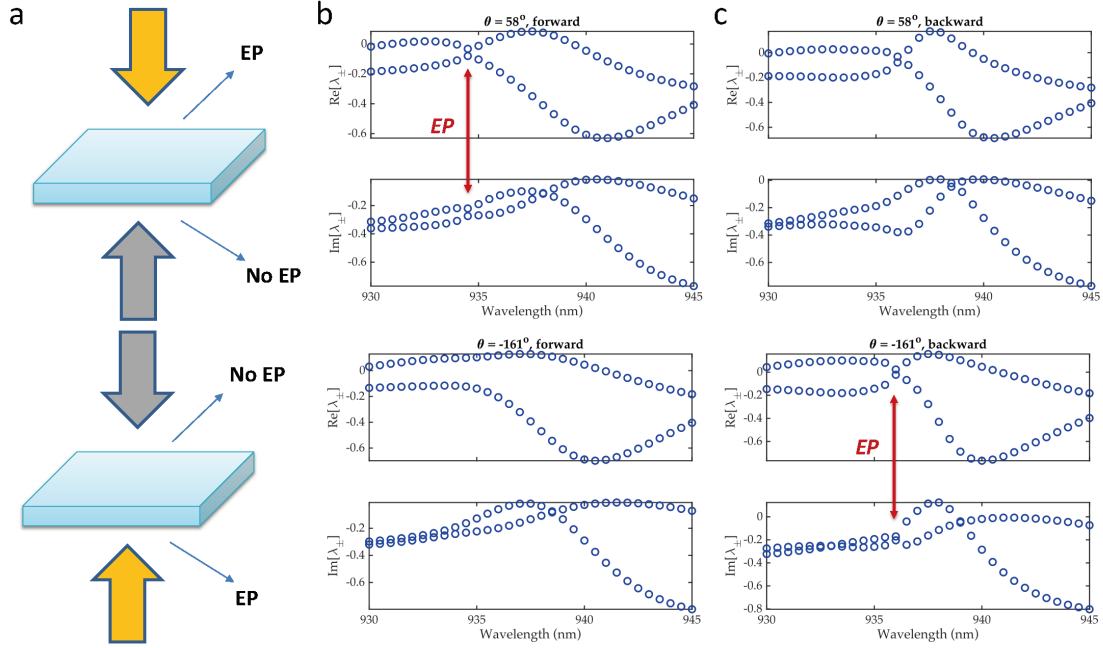
Figure 3.4: (a) Schematic of the asymmetric EP for forward and backward interrogation. (b) Eigenvalue spectrum for forward and backward interrogation around the orientation angle at forward EP. (c) Eigenvalue spectrum for forward and backward interrogation around the orientation angle at forward EP.

An intriguing characteristic of this EP is its asymmetry in forward and backward interrogation due to the deviation of the two off-diagonal terms in Jones matrix. Figure 3.4(a) demonstrates the meaning of this asymmetric EP, referring to that if EP is realized for the forward interrogation, then the backward interrogation shows no EP, or vice versa. We demonstrate this by first tuning the orientation angle to achieve forward EP at $\theta = 58°$ (Figure 3.4(a)), and EP is indicated by the arrow. However, for the backward case at the same angle in Figure 3.4(b), there exhibits no coalesce of eigenvalues. Then in Figure 3.4(c), the orientation angle is changed to the condition fulfilling EP for backward interrogation, which results in the EP in the backward spectrum and no EP in the forward spectrum. Therefore, EP in this rotated L-shaped structure can be concluded as a both chiral and asymmetric EP.

The BIC condition can be utilized for applications in forming polarizer for elliptical polarizations. An example at $\theta = 40°$ is illustrated in Figure 3.5. Figure 3.5(a) plots
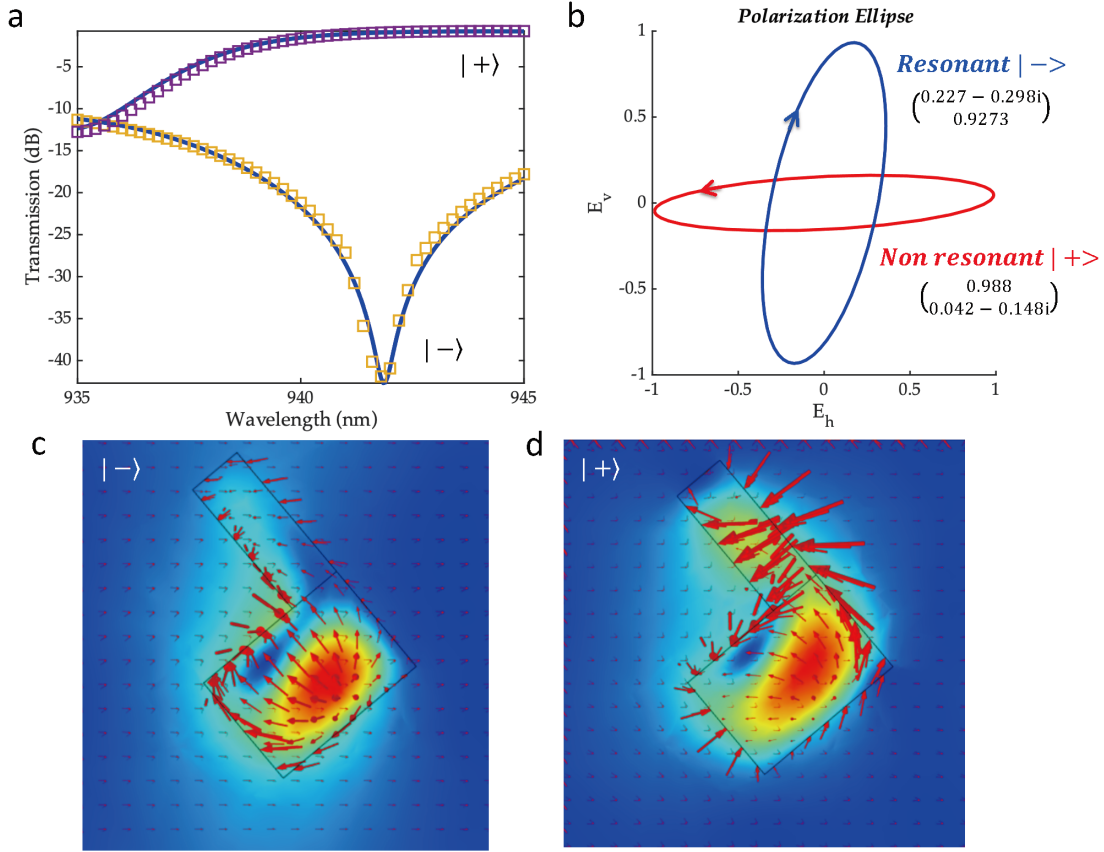
Figure 3.5: (a) BIC in transmission matrix and eigenvalues for two eigenpolarizations at = 40°. (b) Polarization ellipses of the two eigenpolarizations. Magnetic field distribution for the minus state (c) and plus state (d) at 942 nm.

the modulus of eigenvalues versus wavelength in dB scale with blue line, which is also the transmission spectrum with eigenpolarization input. At the dip of minus state, the plus state shows a high transmission. This can be attributed with zero value for one eigenvalue in both real and imaginary part. The minus state is a resonant state which strong interacts with this chiral structure, and the plus state is nearly non-resonant thus showing high transmission rate. Solving the scattering matrix results in two eigenpolarization states: (0.227-0.298i, 0.9273) and (0.988, 0.042-0.148i), as shown in Figure 3.5(b) with polarization ellipses. A verification is conducted by performing a simulation with input of the two states and measure their transmission. The results are plotted in Figure 3.5(a) with square dots, which are in good agreement with the line. Figure 3.5(c,d) demonstrate the magnetic field distribution at 942 nm which is the resonance dip for minus sate, with arrows showing field direction. Figure 3.5(c) shows for minus state, the field resonance is localized in the bottom rectangular, and for

the plus state, the field is "dragged" towards the smaller rectangular, therefore leading to a resonance shift between plus and minus state. This shift helps form the enhanced selectivity for the two input polarizations. The large asymmetric transmission for two polarization states can be employed to realize high-efficiency polarizer for elliptical polarizations.

In conclusion, we have proposed a L-shaped chiral metasurface capable of showing EP, BIC, and asymmetry in the transmission matrix. Due to its chirality, extremely large circular dichroism of over 40 dB can be realized in a large range of orientation angle. By tuning the angle θ, eigenvalues of the transmission matrix can coalesce and become zero, generating the conditions for EP and BIC. Since the structure does not meet the requirement of optically flat, off-diagonal terms in the transmission matrix are not equal, leading to the chiral and asymmetric EP. BIC state has been employed to realize polarizer for elliptical polarizations. This single layer, all-dielectric based metasurface may provide a platform for studying diverse phenomena involving chirality, asymmetry, EP, and BIC.

3.3   Exceptional points with coupled QBIC modes

Exceptional points (EPs) in metasurfaces have been extensively explored in the transmission matrix or Jones matrix. However, there still lacks proposal of eigenmode EP realized with low-loss photonics modes. Here we design a metasurface consisting of unit cell with two asymmetric silicon bars embedded in the glass. Two intrinsic coupled quasi-BIC modes can be formed with the in-plane asymmetry of silicon and glass. By fine tuning this asymmetry and bar separation, EP condition can be reached with high Q factor. This metasurface with eigenmode EP is then employed for EP enhanced refractive index sensing and optical gyroscope. Phenomena like electromagnetically induced transparency (EIT) at EP and nearly stopped light are also demonstrated.

Optical metasurfaces play the vital roles of beam shaping, polarization control, harmonic generation, chiral effect, and hologram, due to their large design freedom and capability of tailoring light propagation. Recent demonstrations also show the applications of metasurfaces in quantum optics, opening up new ways for control of non-classical nature of light, like quantum state superposition, quantum entanglement and single-photon detection. Typically, exceptional points (EPs) are the spectral degeneracy where two or more eigenmodes become coalesced with equal frequency and loss, or described by the matrix when two eigenvalues become the same. Many intriguing effects have been investigated associated with EP, for instance, enhanced sensing, chiral mode switching, Purcell enhancement, and $\mathcal{PT}$ symmetric microlasers. EP sensors have been proposed for nanoparticle detection, gyroscopes, refractive index change, thermal mapping, and tomography reconstruction.

Exceptional points (EPs) in metasurfaces have been mostly demonstrated in the transmission matrix or Jones matrix, which focuses on the input-output amplitude relation rather than the eigenmodes. The first experimental work employs the concept of $\mathcal{PT}$ symmetry and orthogonally coupled split ring resonators to achieve EP and symmetry breaking in polarization space. Although eigenmode EP has been explored in plasmonics metasurfaces with
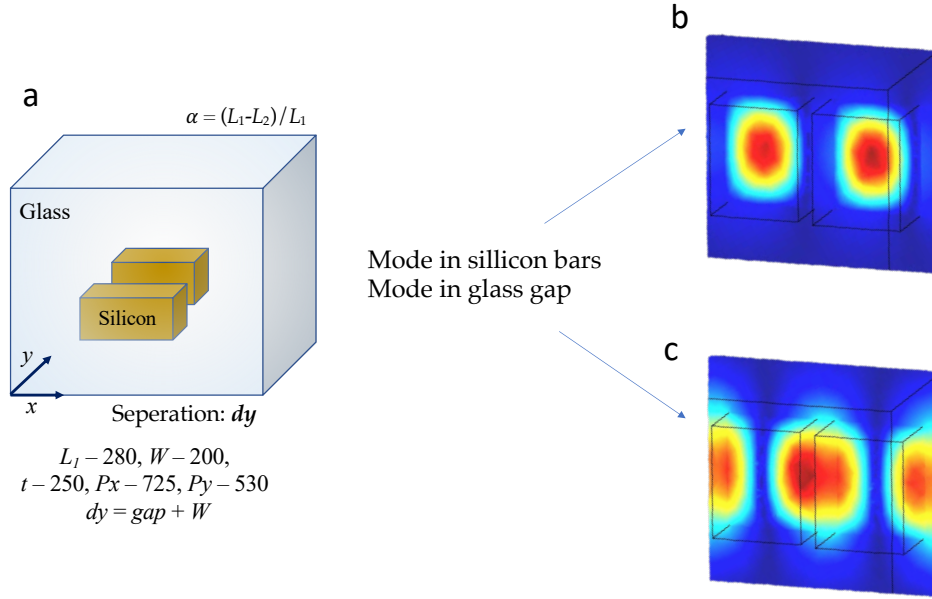
Figure 3.6: Schematic of the metasurface's unit cell with periodic boundary condition in x (P_x) and y (P_y) direction. Two silicon bars are embedded in the glass. $L_{1,2}$, W, t is the length, width, and thickness of the bar. Length asymmetry is defined by $\alpha = (L_1 - L_2)/L_1$. (b) Simulated electrical field profile of the xz cross section for the quasi-BIC mode contained in the silicon bars. (c) Stimulated electrical field profile of the xz cross section for the second quasi-BIC mode centered in the glass gap and extending to the silicon bars.

simulation and recently realized in experiments, high loss introduced by metal resonances is always a concern. Hence, we take advantage of the photonics metasurface and arrangement of quasi-BIC mode to realize a lower-loss eigenmode EP in metasurface. The two quasi-BIC modes are intrinsically coupled due to the asymmetry of silicon and its induced asymmetry of glass. The formed EP is then demonstrated as EP index sensor and EP optical gyroscope, which benefits from EP's square-root relation for high sensitivity. Finally, the metasurface shows the spectrum feature of electromagnetically induced transparency (EIT) at EP, and achieves nearly stopped light in the group delay.

It has been well demonstrated that the BIC and quasi-BIC modes can be realized with in-plane symmetric structure and by breaking this symmetry, respectively. Here the metasurface consists of unit cell with two asymmetric silicon bars embedded in the glass. The two bars have the same dimension in width W and thickness t, except their length L_1, L_2. The asymmetry is characterized by α, which is defined as ratio of the length difference. The two bars are separated with a distance of dy. To obtain the structure's transmission spectrum and

field distribution, FEM simulation software COMSOL is employed with periodic condition applied in the x and y direction with lattice constant of P_x and P_y. The incident polarization is parallel with y direction. Figure 3.6(a) shows detailed parameters used in simulation, and refractive index of glass and silicon is taken as 1.5 and 3.5. Figure 3.6(b,c) show the cross section of field distribution of the two quasi-BIC modes, one of which mainly remains in the silicon bars, and the other has mode pattern overlapping the glass and silicon. Forming quasi-BIC with two asymmetric particles has been presented in previous studies, but the surrounding is mainly air. While using this embedded arrangement, the asymmetry of silicon also leads to asymmetry of the glass, therefore, another quasi-BIC mode appears in the glass gap and extends to the silicon bars. The two modes can be mutually coupled with tunable features by modifying the asymmetry and separation between two bars. It's noteworthy that the two modes are geometrically non-separable, which is quite different from mode coupling in paired nanoparticles.

Figure 3.7 demonstrates the frequency and loss switch between the two quasi-BIC modes through changing the parameters of α and dy. The peaks with number in the spectrum correspond to the electrical field distribution in the right. In Figure 3.7(a), with the separation dy chosen as 245 nm, increasing α from 0.09 to 0.17, the relative frequency position between the two modes crosses and switches, where I, IV and II, III are the same mode with reference to the field pattern. In Figure 3.7(b), by keeping the asymmetry ratio α constant and tuning dy from 240 to 250 nm, I, III and II, IV are the same mode presenting no frequency switch. While the linewidth switches between the two modes as clearly revealed by the spectrum since the high Q mode move from I to IV. Therefore, simultaneously tuning the two parameters α and dy can result in both frequency and loss crossing of the two quasi-BIC modes, which fulfils the requirement of forming an EP.

Figure 3.8 verifies there exists an EP with the switch dynamics of crossing and anti-crossing in frequency and loss. A series of complex transmission spectrum is obtained by sweeping different dy values, and then rational fitting Is employed to extract the eigenfrequencies and corresponding loss rates. Figure 3.8(a,b) plot the eigenfrequencies (top) and losses (bottom) as a function of dy for $\alpha = 0.09$ and 0.14, respectively. A close inspection of Figure 3.8(a) shows that there is a crossing feature in frequency and anti-crossing feature in loss at $dy = 247$ nm, and in comparison, this dynamic switches in Figure 3.8(b), where crossing emerges in loss and anti-crossing in frequency. This dynamic switch phenomenon by changing one parameter marks the unambiguous existence of an EP. This resonant frequency crossing and linewidth crossing can be intuitively observed by looking at the evolution of transmission spectrum in Figure 3.8(c,d). The lineshape of S21 amplitude is plotted from top to bottom with increasing dy value, and a clear cross emerges by the two resonant peaks. Also, at $dy = 265$ nm, the loss of one eigenmode vanishes and the linewidth becomes zero, indicating the realization of BIC condition. Although not shown here, BIC for the other mode can be achieved at $dy = 234$ nm, as implied by the dropping trend in loss before $dy = 245$ nm.

From Figure 3.8, the EP is predicted to appear between $\alpha = 0.09$ and $\alpha = 0.14$. In Figure 3.9, a narrow range of 0.12~0.13 is chosen to demonstrate this EP more clearly.
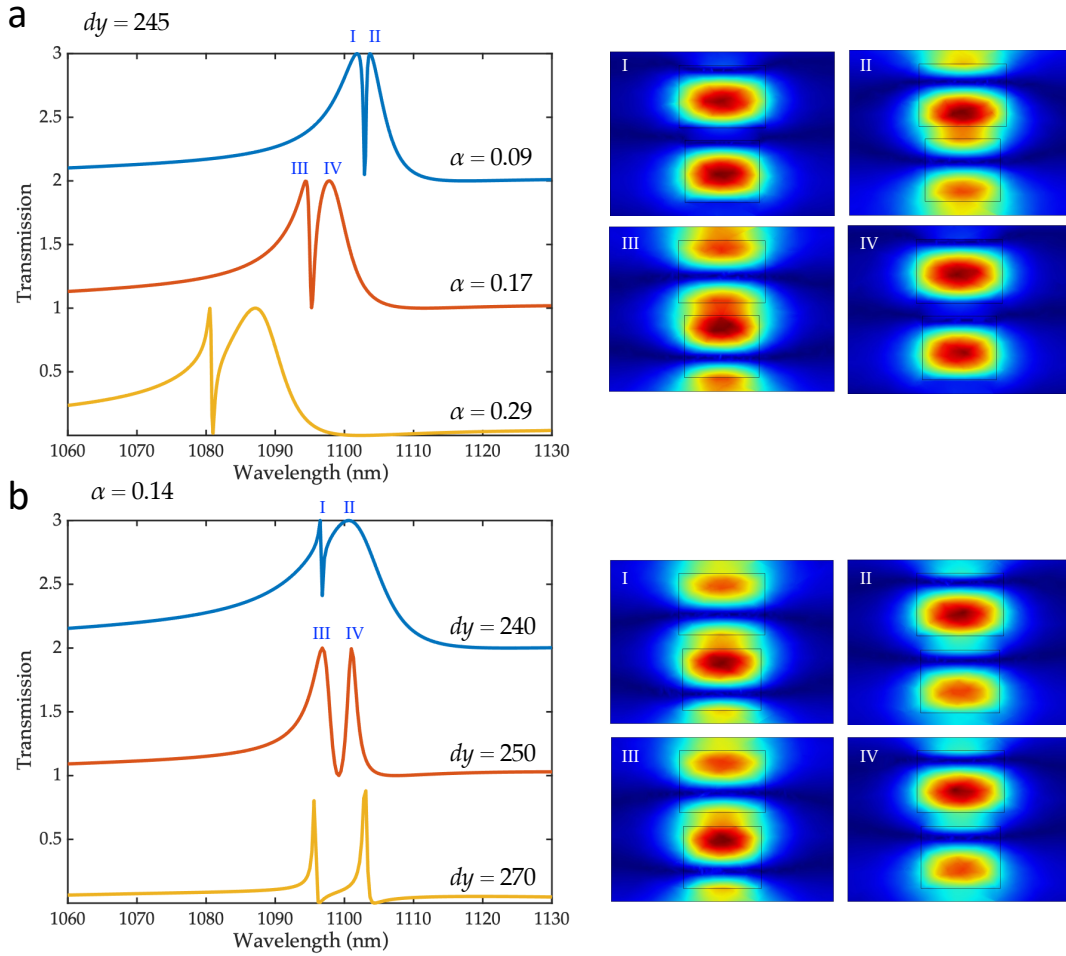
Figure 3.7: Amplitude of S21 with increasing asymmetry ratio and constant dy showing frequency crossing. Inferred from mode profiles, I,IV and II,II correspond to the same mode. (b) Amplitude of S21 with increasing separation and constant alpha showing linewidth crossing. Inferred from mode profiles, I,III and II,IV correspond to the same mode.

Figure 3.9(a,b) demonstrate the same crossing and anti-crossing features as those in Figure 3.8(a,b). Examination in Figure 3.9(c,d) of the real and imaginary part of the residues from rational fitting also shows the diverging effect near EP, which is an additional confirmation of the presence of EP. By fine tuning the value of α in simulation, the EP is found to locate at $\alpha = 0.123$, where the frequency and loss extracted from the two modes exactly coalesce.

To push EP useful in real-world applications, two sensing mechanisms are proposed with enhanced sensitivity due to the square-root perturbation-response relation near EP. Figure 3.10(a) demonstrates the schematic of an EP refractive index (RI) sensor, in which the
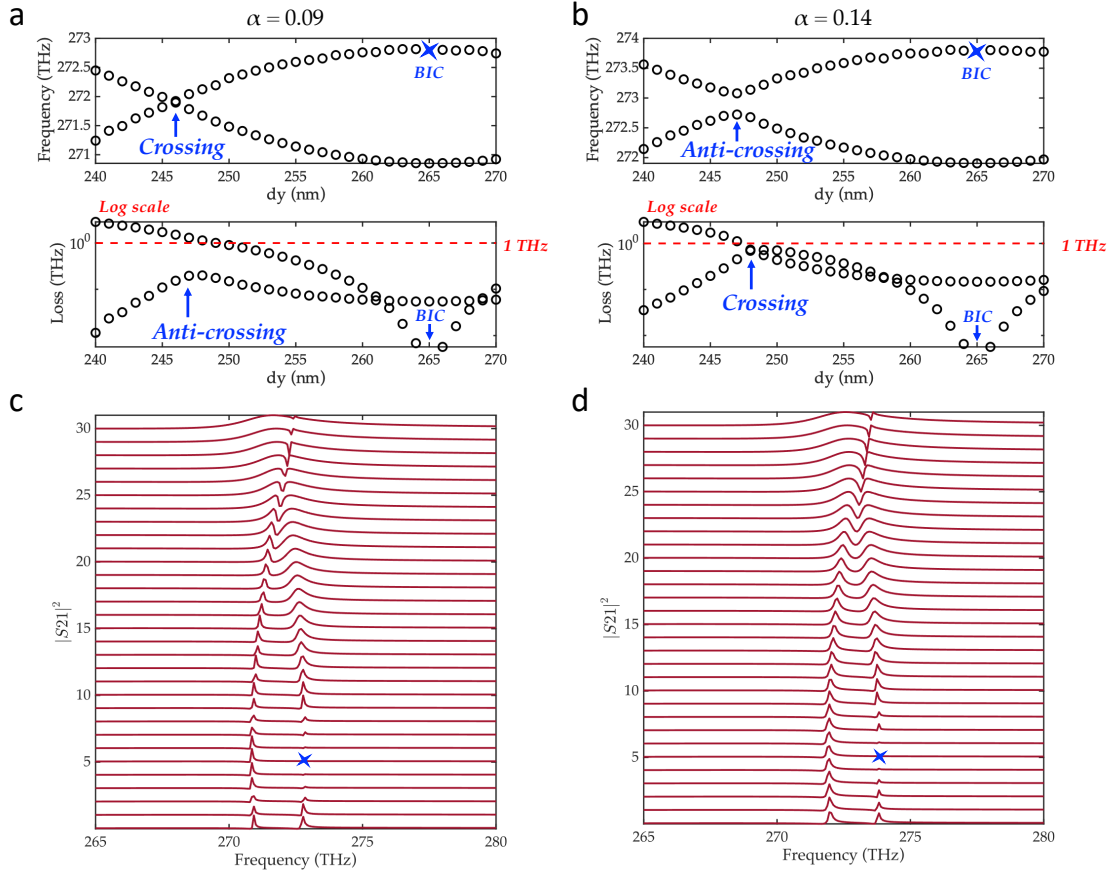
Figure 3.8: (a) At $\alpha = 0.09$, two coupled quasi-BIC modes show crossing in frequency and anti-crossing in loss. (b) At $\alpha = 0.14$, two coupled quasi-BIC modes show crossing in loss and anti-crossing in frequency. EP unambiguously exists between $\alpha = 0.09$ and 0.14 due to the dynamic switch in crossing and anti-crossing. One BIC mode appears at $dy = 265$ nm, where the loss becomes zero. The other BIC mode is verified to appear at $dy = 234$, as revealed by the dropping trend in loss. (c) Corresponding evolution of transmission spectrum with increasing dy in (a) and frequency crossing. (d) Corresponding evolution of transmission spectrum with increasing dy in (b) and linewidth crossing. BIC mode is denoted with blue marker.

system's modes are responsive to the RI change (Δn) in the surrounding material, glass. This can also be applied for stress and thermal sensing, since the applied stress and thermal will induce a RI change in the glass on the scale of 10^{-3}. Figure 3.10(b) illustrates the design's capability of working as an EP enhanced optical gyroscope. In the presence of a x-polarized incident light, rotation vertical to the z direction (top) or x,y direction (bottom) can introduce perturbation to the transmission spectrum and eigenmodes, and positioned at
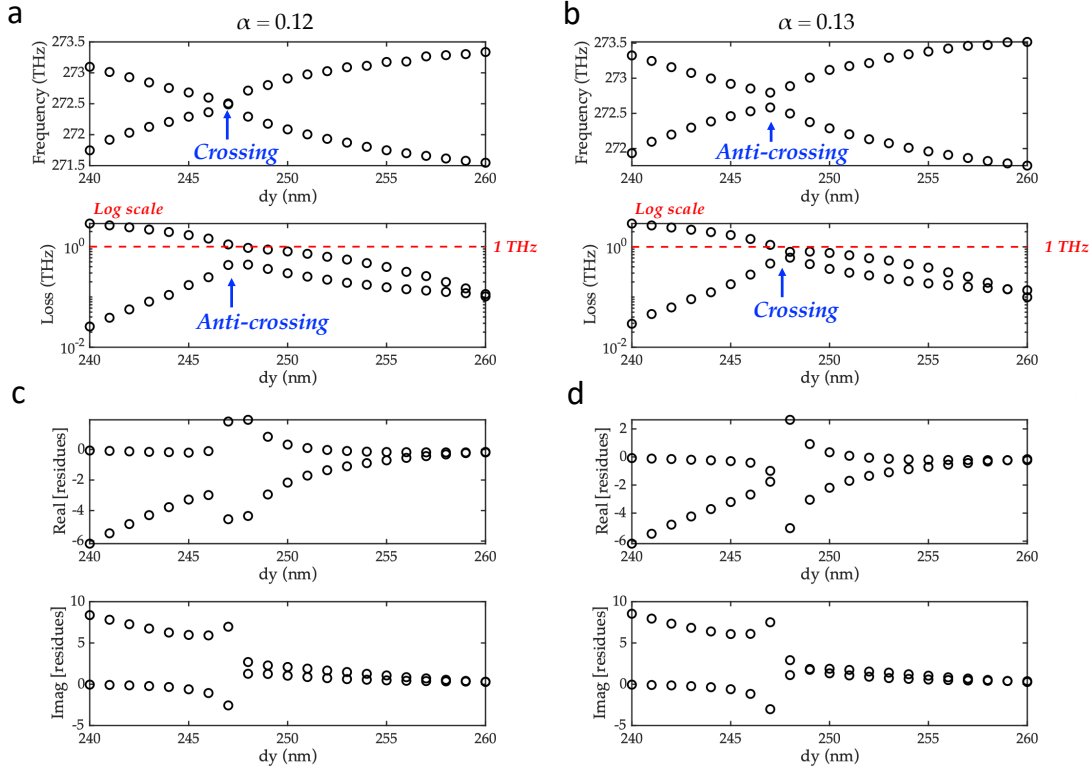
Figure 3.9: Verification of EP with a narrow range of α. (a) At $\alpha = 0.12$, crossing appears in frequency and anti-crossing in loss. (b) At $\alpha = 0.13$, crossing appears in loss and anti-crossing in frequency. (c) Real part (top) and imaginary part (bottom) of the residues from rational fitting in (a). (d) Real part (top) and imaginary part (bottom) of the residues from rational fitting in (b). Diverging effect around the crossing/anti-crossing point confirms the existence of EP.

EP, this perturbation can be detected with a square-root enhancement of sensitivity. This mechanism may greatly contribute to the improved 3D position and rotation sensing for space applications.

Figure 3.11 verify the EP enhanced sensing capability with square-root relation corresponding to the RI sensing and EP gyroscope in Figure 3.10. In Figure 3.11(a), the perturbation is the RI change , and the frequency splitting is calculated as a function of RI change, showing good agreement with the square-root fitting. Inset plots the curve in log scale and verifies the slope is 0.5, corresponding with typical EP sensors. As for the gyroscope case, the perturbation is $\Delta\theta$, defined as the deviation of incident polarization from the x direction. Increasing the perturbation angle results in a square-root improvement of frequency splitting, thus confirming the performance of EP optical gyroscope. It's important to note that detection of the angle is not limited to in-plane rotation, but also works for rotation
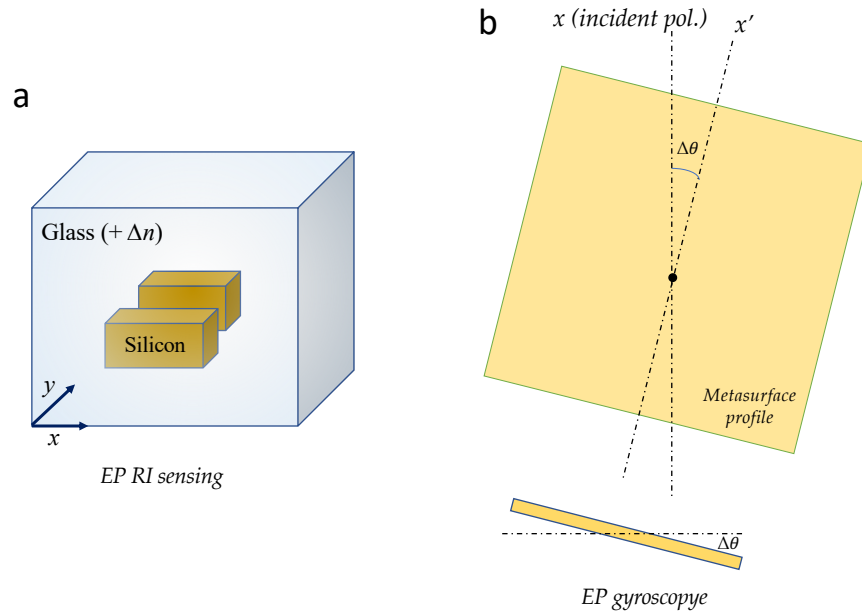
Figure 3.10: Proposed schematic for EP enhanced refractive index (RI) sensing. A small RI change δn happens in the surrounding materials of silicon bars. (b) Proposed schematic for a EP optical gyroscope for rotation angle detection. The metasurface has a small rotation angle $\delta\theta$ against the incident polarization, leading to a perturbation and resultant mode splitting. This mechanism can also be extended to 3D rotation.

vertical to x and y direction, or for the detection of incident light angle on the metasurface, which only results in different ratio in square-root fitting.

In the following, slow light effect is investigated around the coupled quasi-BIC induced EP. The slow light can be characterized by the group delay, defined as, where. Figure 3.12(a,b) plot the transmission spectrum and group delay versus frequency for parameters fine-tuned at EP, showing the lineshape of electromagnetically induced transparency (EIT), and slightly deviated from EP, showing the Fano lineshape. There emerges a sharp peak in the group delay, indicating the slowing of light. Especially for the group delay at EP, Figure 3.12(c) shows an enlarged view of the group delay around this peak, where a discrete positive value (denoted by the blue marker) appears among continuous negative values. This discrete value may be due to the simulation, and it also implies a value of zero, corresponding to a group delay of zero, that is, the stopped light. By decreasing the frequency interval to very small value as shown in Figure 3.12(d), this EIT at EP induces a nearly stopped light with a small group velocity $v_g = 4.62 \times 10^{-8}$ and an extremely large group index $n_g = 21645000$. Therefore, the designed coupled quasi-BIC modes assisted EIT at EP can be employed for realizing nearly stopped light propagation. Figure 3.12(e) demonstrates the
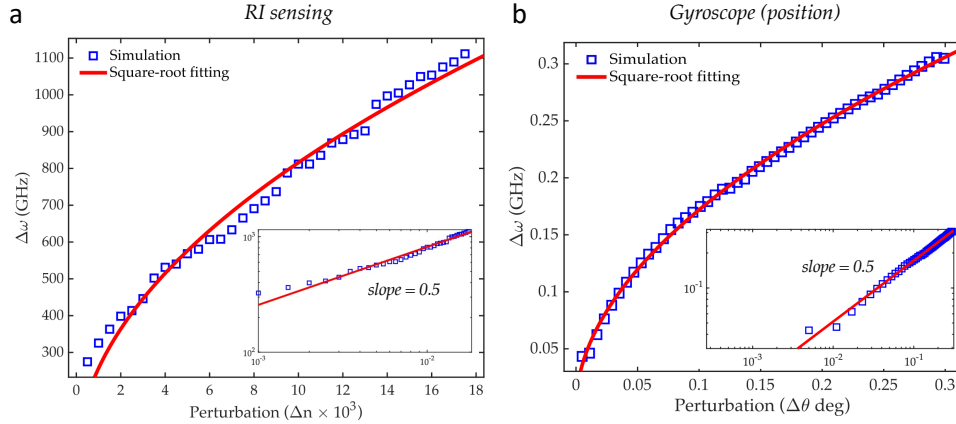
Figure 3.11: Characterization of the (a) EP RI sensor and (b) EP gyroscope in Figure 5. A square-root response associated with EP is clearly observed. Inset shows the plot in log scale and a fitted slope of 0.5.

phase of transmission with very small simulation interval, and the slope of phase is going to infinity, confirming the near-zero group delay. It's also intriguing that stopped light at EP has been previously theoretically verified with $\mathcal{PT}$-symmetric coupled waveguides using numerical simulation [35].

In conclusion, by simply embedding two asymmetric silicon bars in glass, two coupled quasi-BIC modes can be formed with high Q factor. Fine tuning the asymmetric ratio and bar separation can lead to the fulfilment of EP condition, where the resonant frequency and loss of the two quasi-BIC modes become coalesced. With EP at hand, sensitivity enhanced EP sensors are proposed for RI sensing and optical gyroscope to detect the rotation angle. Associated with high-Q resonances, EIT lineshape at EP and Fano lineshape away from EP can be revealed with slow light effect. For EIT at EP, simulation results demonstrate the realization of nearly stopped light with extremely large group index.

3.4   Chiral plasmonics at EP

Plasmonics exceptional points have been demonstrated in experiments with a two-bar structure by introducing asymmetry to their resonance frequency [49]. The first design is two gold bars having different lengths in the same layer and with the same surrounding material. The second one is a two-layer structure shown in Figure 3.13, where the bottom bar is placed in the spacer of index equal to 1.58 (slightly larger than SiO_2 of 1.5), and the top bar is surrounded by the air. For both setups, changing the period in y direction (P_y) and position shift between two bars (dx) can result in the condition of EP in plasmonics system. The asymmetry, either the length difference, or the surrounding difference, leads to different
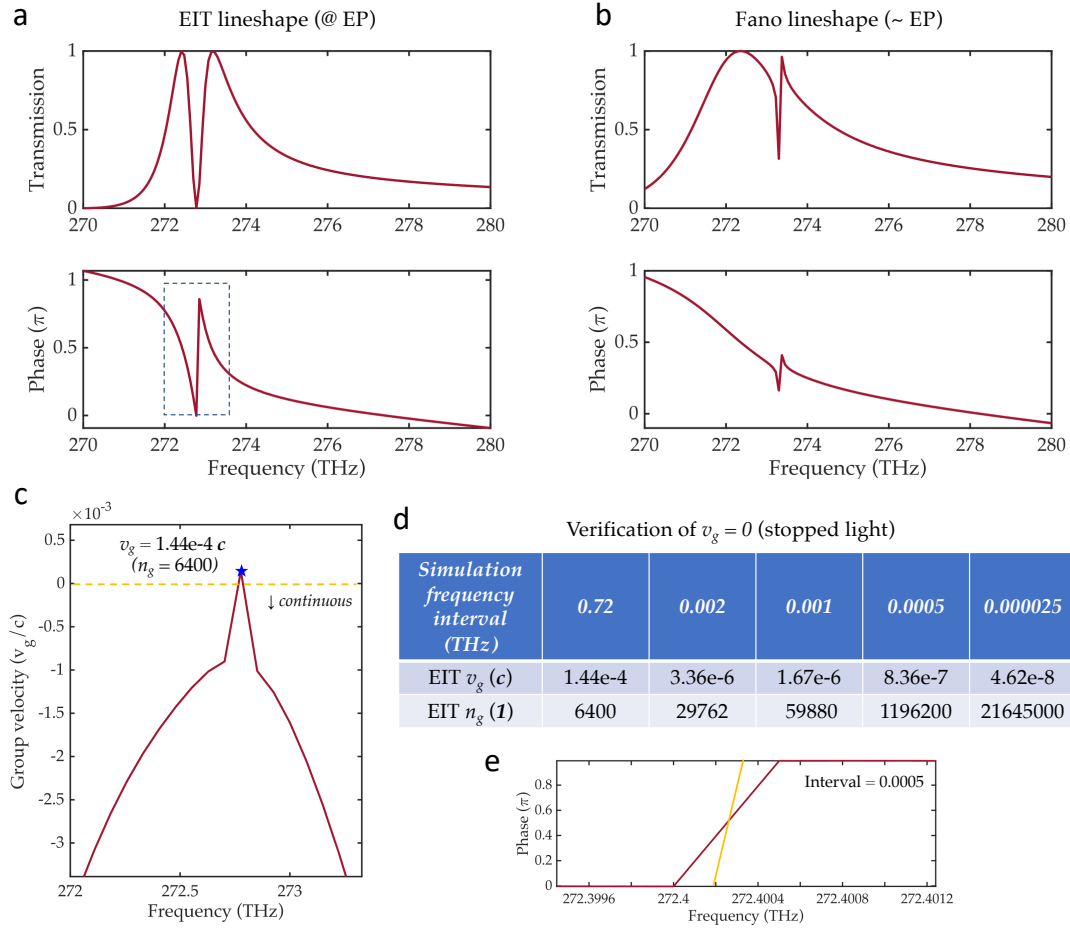
Figure 3.12: (a) EIT at EP, EIT-like lineshape when EP condition is reached. (b) Deviated from EP, the Fano-like lineshape appears. Top panel is the S21 amplitude, bottom panel is the phase relation. Dashed line indicates a much sharper phase change for EIT at EP. (c) Enlarged view of the group velocity versus frequency for EIT at EP, where the blue marker is a discrete positive value. (d) Table shows increasing the simulation frequency interval leads to larger group index and smaller group velocity up to near zero. Nearly stopped light can be realized with EIT at EP. (e) Phase-frequency relation with interval equal to 0.0005 THz. The slope is going to infinity.

resonant frequencies of the two modes, which is the prerequisite due to the nearly same loss rate. For the purpose of illustration, the period in x direction (P_x) is set as constant of 400 nm, and dx shifts from 80 nm to 200 nm. With periodic condition applied, the incident polarization is parallel to the x direction.

Firstly, plasmonics EP is demonstrated with the two bars aligned parallel as shown in
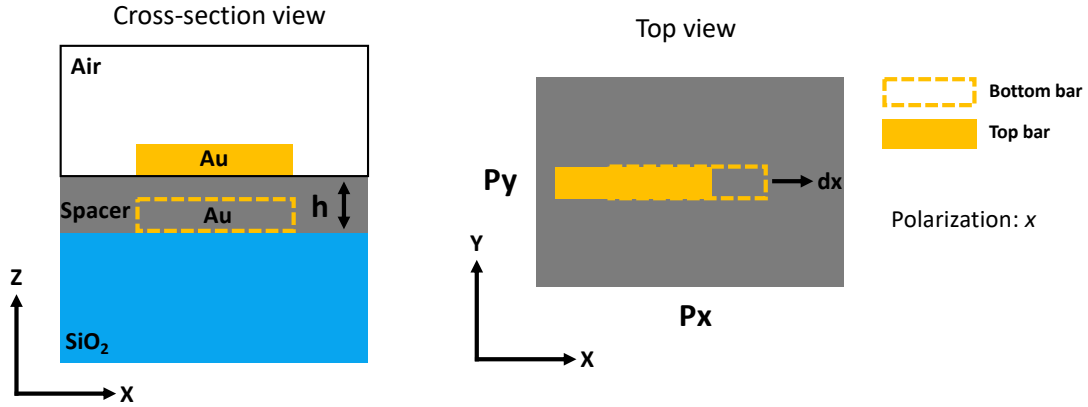
Figure 3.13: Cross-section and top view of the unit cell of the plasmonics metasurface with two bars exhibiting no chirality. The spacer is made of SU8 with index 1.58, and the thickness h is 100 nm. Periodic condition is applied in x and y direction. dx is the position shift between the two bars. Incident polarization is parallel to the x direction.
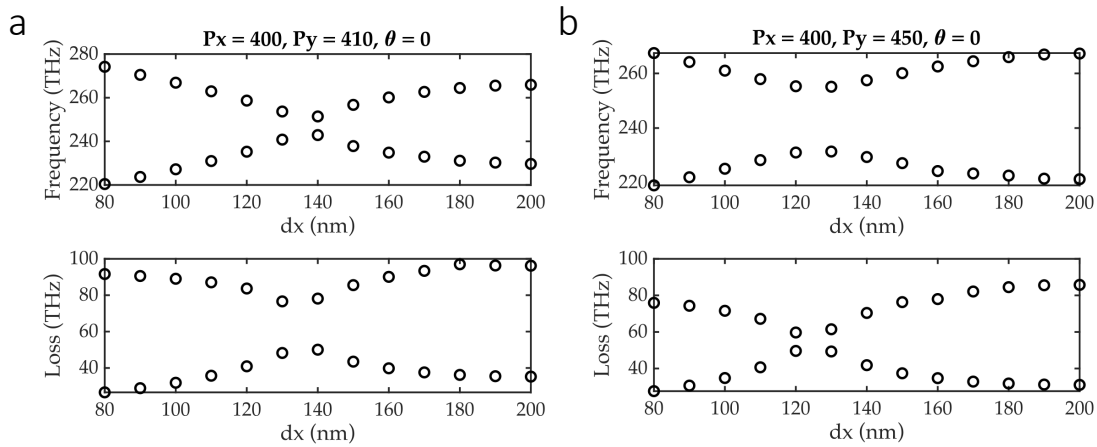
Figure 3.14: EP in achiral plasmonics. Resonant frequency (top) and loss (bottom) extracted from rational fitting for achiral plasmonics at (a) $P_y = 410$ nm and (b) $P_y = 450$ nm.

Figure 3.13. By sweeping dx, the complex transmission S21 is recorded and rational fitting is employed to extract resonances information (frequency and loss) for the two coupled plasmonics modes. Figure 3.14 shows the eigen-frequency (top) and loss (bottom) for P_y = 410 and 450 nm. Figure 3.13(a) shows the dynamic of frequency crossing and loss anti-crossing, while by just changing P_y, the trend inverts to frequency anti-crossing and loss

crossing. This switch actually indicates the existence of an EP between 410 and 450 nm for P_y. Therefore, plasmonics EP for this achiral structure is realized.
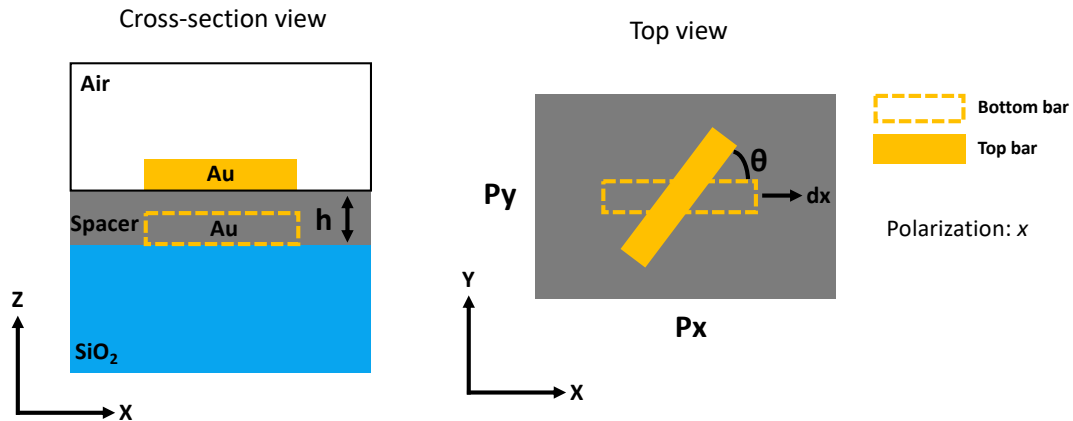
Figure 3.15: Cross-section and top view of the unit cell of the chiral plasmonics metasurface. The top bar is rotated with an angle of θ to introduce 3D chirality. Other conditions are the same with Figure 1.

This plasmonics EP benchmark can be modified to reveal chiral effects by simply rotating the top bar with an angle of θ, which breaks the mirror symmetry. Figure 3.15 shows the cross section and top view of this chiral plasmonics structure.
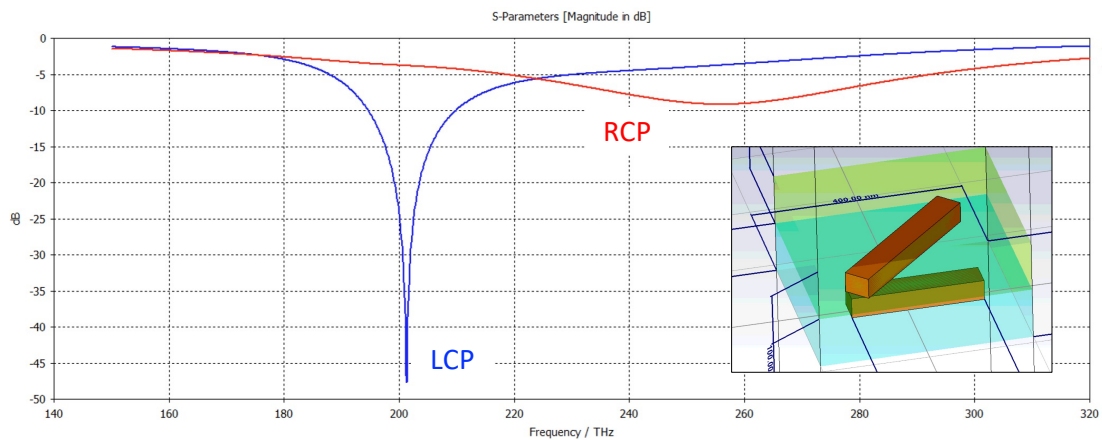
Figure 3.16: Asymmetric transmission for circularly polarized light (LCP, RCP). Inset shows the CST simulation setup for the two rotated bars.

Chirality indicates a very different response between RCP and LCP interrogation. Figure 3.16 illustrates this chiral effect from the transmission rate of RCP and LCP. In dB scale, the two-bar structure shows a large circular dichroism with the maximum occurs at transmission dip of LCP, where the difference reaches 40 dB. This discrepancy resembles the spectrum of a notch filter, excluding LCP light and maintain most RCP at one frequency point. The RCP resonance is comparably smooth.
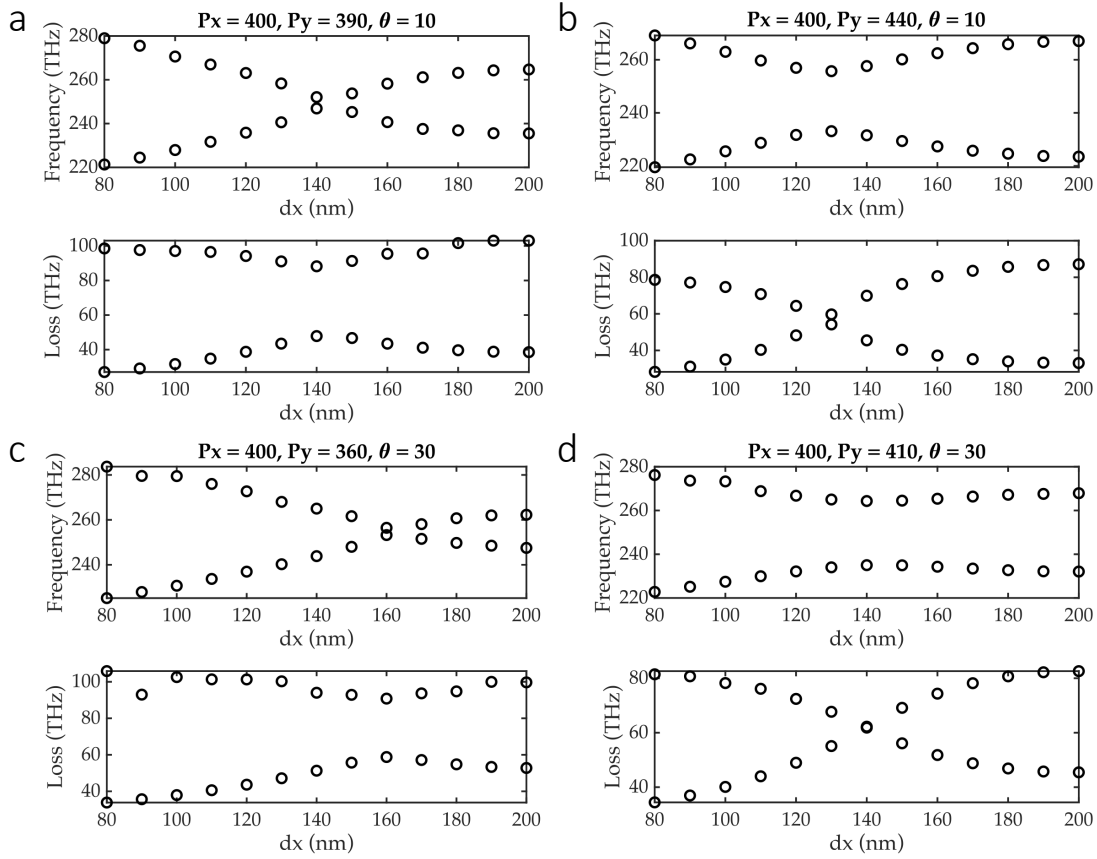
Figure 3.17: EP in chiral plasmonics. At rotation angle of 10 degrees, resonant frequency (top) and loss (bottom) extracted from rational fitting for achiral plasmonics at (a) $P_y = 390$ nm and (b) $P_y = 440$ nm. At rotation angle of 30 degrees, resonant frequency (top) and loss (bottom) extracted from rational fitting for achiral plasmonics at (c) $P_y = 360$ nm and (d) $P_y = 410$ nm.

EP can also be found for this chiral plasmonics. As shown in Figure 3.17(a,b), for a rotation angle of 10 degrees, changing P_y from 390 to 440 nm, there is a dynamic switch in the frequency and loss. This is similar for $\theta = 30$ degrees in Figure 3.17(c,d). Therefore, EP

is verified in this plasmonics metasurface with chiral effects. Chiral plasmonics at EP may serve as an EP-enhanced chiral sensors for molecules and biomedicine.
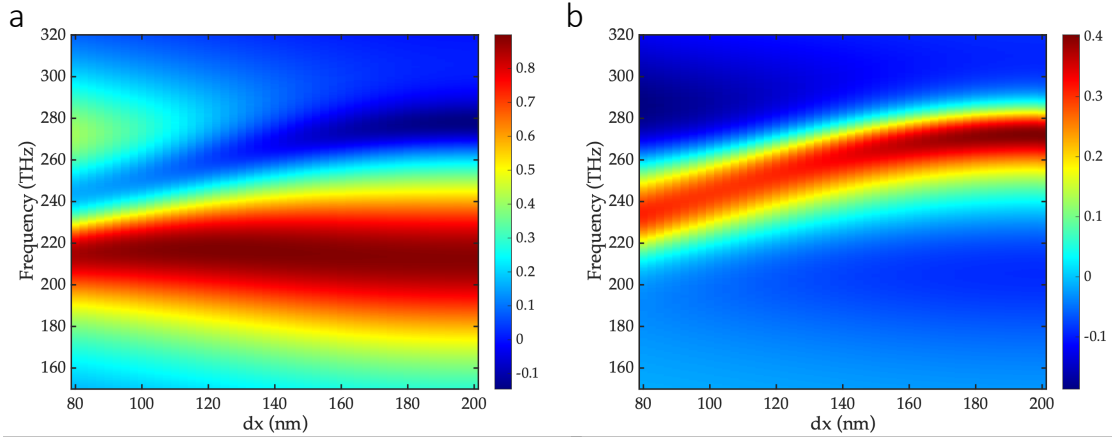
Figure 3.18: (a) Diattenuation as a function of dx and frequency. (b) Circular dichroism as a function of dx and frequency.

Figure 3.18(a) plots the simulated diattenuation as a function of position shift and frequency. This asymmetric transmission for linear polarizations (TE, TM) indicates that a polarizer nature for this chiral plasmonics metasurface. To characterize difference for asymmetric transmission of circular polarizations (LCP, RCP), circular dichroism (CD) versus dx and frequency is demonstrated in Figure 3.18(b). EP is again confirmed in a chiral plasmonics metasurface, and many intriguing questions like relation among EP and chirality wait to be investigated.

Aforementioned EP is only the EP in a chiral plasmonics metasurface. However, to evaluate the "chiral EP", Jones matrix needs to be used. The Jones matrix can be written as $T_{lin} = \begin{pmatrix} t_{xx} & t_{xy} \\ t_{yx} & t_{yy} \end{pmatrix}$, where the four components are the complex S21 with different polarization states. For instance, the subscript notation xy refers to input y polarization and output x polarization. For each point, the simulation is conducted four time to test two input polarizations and two output polarizations. The obtained complex determinant from Jones matrix is taken for rational fitting. Figure 3.19 shows the resonances information, and the switch of crossing and anti-crossing ambiguously ensure the existence of a "chiral EP" between $P_y = 300$ and 350 nm.

To conclude, EP in a chiral plasmonics metasurface is observed with a rotated two-bar structure. By using determinant from Jones matrix, the structure also demonstrates plasmonics "chiral EP". These findings may contribute to study on the EP, chirality, and sensing.
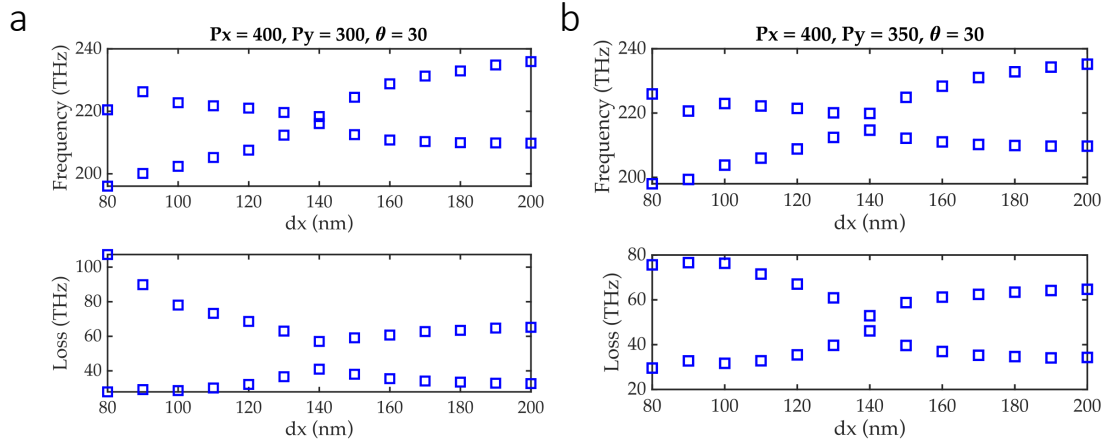
Figure 3.19: Plasmonics chiral EP. At rotation angle of 30 degrees, resonant frequency (top) and loss (bottom) extracted from rational fitting for achiral plasmonics at (a) $P_y = 300$ nm and (b) $P_y = 350$ nm. S21 for rational fitting is obtained Jones matrix.

3.5 Coupled plasmonics and photonics mode induced hybrid BIC and EP

Mode coupling has been the enduring topics from circuits, waveguides, resonators, metasurfaces, to quantum systems. Plasmonics and photonics mode are the two different resonances originate from dielectric and metal arrangements. Here we investigate the hybrid coupling between photonics mode and plasmonics mode using a dielectric metasurface involving additional metal particles. Hybrid bound state in the continuum (BIC) and exceptional point (EP) are observed through tuning either the plasmonics or photonics mode.

The plainest arrangement of realizing mode coupling effect can be the two closely positioned waveguides or resonators, through their evanescent fields. Many intriguing phenomena will occur with coupled modes, including the special conditions called exceptional points and bound states in the continuum, where the two eigenmodes become coalesced, and one eigenmode become lossless revealing zero linewidth, respectively. Mostly, EPs and BICs are demonstrated with pure photonics modes using dielectric resonators and metasurfaces, for instance, the famous whispering gallery modes resonators with PT symmetric setup or nanoparticle modulated mode interaction; in-plane symmetry and broken symmetry in dielectric metasurfaces result in BIC and quasi-BIC with high Q factor.

Recently, plasmonics modes have been managed to achieve both plasmonics BICs [20, 53] and plasmonics EPs. As for the BICs, silver grating coated by a layer of dielectric is utilized to form both photonics and plasmonics BICs by sweeping the incident angle. While plasmonics EP is experimentally verified with metasurface of shifted asymmetric gold bars by inspecting switch of the crossing and anti-crossing dynamics.

However, there are still limited research on the coupling between plasmonics and photonics mode, and it's of importance due to their different origins of resonance and discrepancy in optical loss. Hence, we explore the coupling effect between metal bar placed on the top of a dielectric metasurface, which leads to the condition of BIC and EP. From eigenmode analysis, photonics BIC is observed even in the symmetry-broken dielectric metasurface due to coupling induced compensation from the additional metal bar. Simultaneous coalescence of frequency and loss indicates the existence of a hybrid EP, that is, the photonics mode and plasmonics mode degenerates to behave as one single mode. At this kind of EP, mode hybridization is found to be the maximum with equal domination. Study on these photonics-plasmonics mode coupling effects may play a vital role in plasmonics lasers [54, 55, 56], reducing plasmonics loss, understanding coupling at EP, and, applications of hybrid structures.

Coupling between the photonics and plasmonics mode is implemented with a metasurface consisting of unit cell of two asymmetric silicon bars embedded in glass and an additional gold bar placed on the top surface of the glass host (Figure 3.20(a)). Periodic condition is applied in the xy plane. Refractive index of silicon and glass is chosen as 3.5 and 1.5 for their negligible loss, and for gold, the index is taken from Johnson and Christy [18]. The gold bar can be shifted away from the center in x and y direction to realize different coupling conditions for the photonics-plasmonics interaction. When there is no gold bar, the dielectric metasurface reveals photonics resonances, as shown by the blue lineshape in Figure 3.20(b). With the presence of gold bar, the photonics mode is perturbed and thus the peak splits into two parts, the smaller wavelength of which represents plasmonics mode with lower Q factor. Changing the position along y axis of the gold bar can continuously tune the photonics-plasmonics coupling strength, which is also observable through the transmission spectrum. Figure 3.20(c) plots the evolution of transmission with shift of the gold bar dy_{Au} ranging from -20 nm to 90 nm. Except for $dy = 20$ nm, there exists a dip similar to the red lineshape in Figure 1b. While at $dy = 20$ nm, the dip vanishes due to fulfillment of BIC condition, where one mode become lossless with zero linewidth. The asymmetric bars naturally support photonics quasi-BIC mode, that is, requirement of BIC is slightly broken. Here, additional introduction of the gold bar induced plasmonics mode makes up this deviation and again pushes the system to BIC through this hybrid mode coupling effect. A positive dy refers to that the metal bar is moved closer to the larger silicon bar, implying an asymmetric coupling between the two-bar quasi-BIC mode. This asymmetry plays an important role in realizing the BIC mode again, since the in-plane asymmetry of dielectric arrangement intrinsically hinders the formation of BIC. Rational fitting of the complex transmission can be employed to extract information of the hybrid mode coupling, as shown in Figure 3.20(d). It's easy to distinguish the evolution of plasmonics and photonics mode based on the high-loss of gold bar. At $dy = 20$ nm, rational fitting fails to extract two modes due to the disappearance of linewidth, indicating the emergence of BIC mode. This BIC mode happens in the development of photonics mode, and thus can be called as a hybrid coupling induced photonics BIC. Since the loss has a very large difference, the spectrum is expected to demonstrate Fano lineshape as shown by the red curve in Figure 3.20(b). For the point of $dy = -78$ nm, the
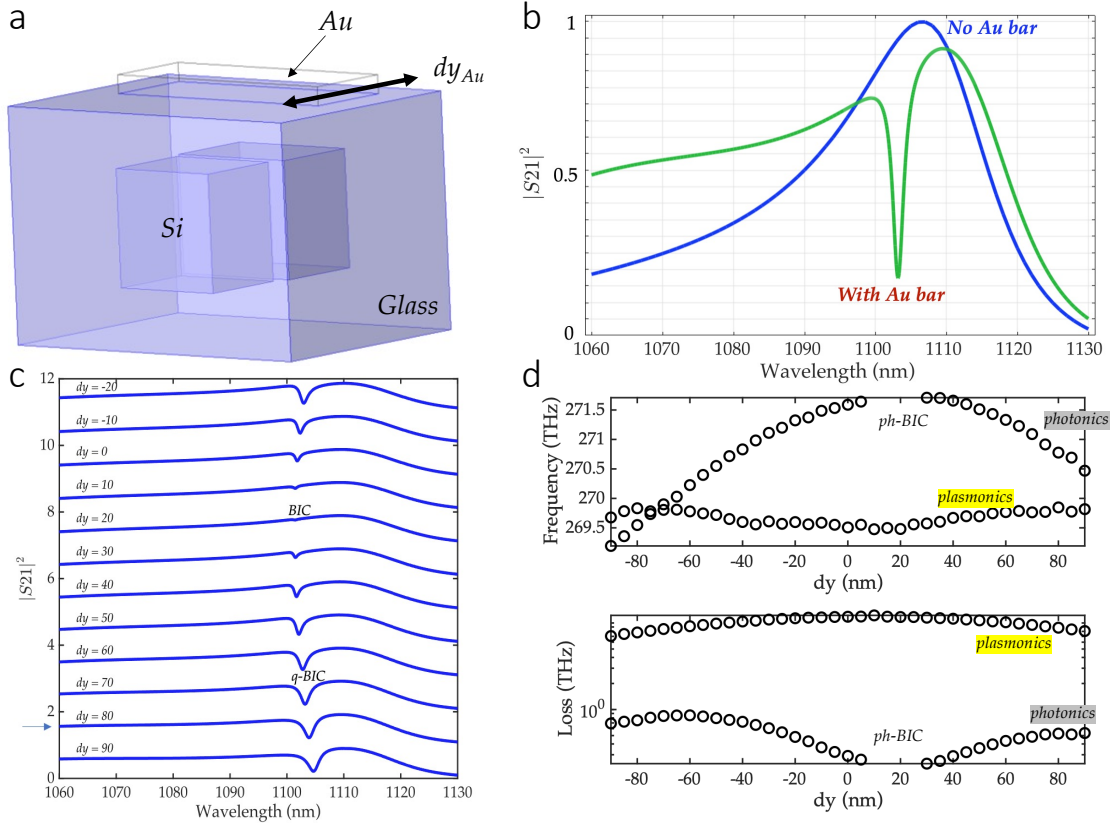
Figure 3.20: (a) Schematic of unit cell of the silicon-in-glass dielectric metasurface with an addition gold bar placed on the surface. The gold bar shifts in y direction. (b) Transmission spectrum for only the dielectric metasurface and after adding the gold bar. Hybrid mode coupling effect induces a Fano lineshape. (c) Transmission spectrum for different values of position shift of the gold bar in y direction (dy). BIC occurs at $dy = 20$ nm where the linewidth vanishes, while other values have a quasi-BIC feature. (d) Extracted frequency (top) and loss (bottom, in log scale) of the two modes in (c) from rational fitting. Around the photonics BIC at $dy = 20$ nm, loss is reaching zero.

photonics and plasmonics mode has the same frequency, Fano lineshape will degenerate to an electromagnetically induced transparency (EIT) lineshape. This hybrid-mode EIT and Fano may enrich similar observations in pure dielectric and plasmonics structures, and contribute to applications like bio-sensing and slow light.

The dielectric structure with two asymmetric bars embedded in glass is known to show two resonances, one of which originates from the silicon, and the other is attributed to the glass asymmetry. With the gold bar positioned at the BIC point of $dy = 20$ nm (Figure 3.21(a)), shift in x direction (dx_{Au}) can break this hybrid-mode coupling induced photonics
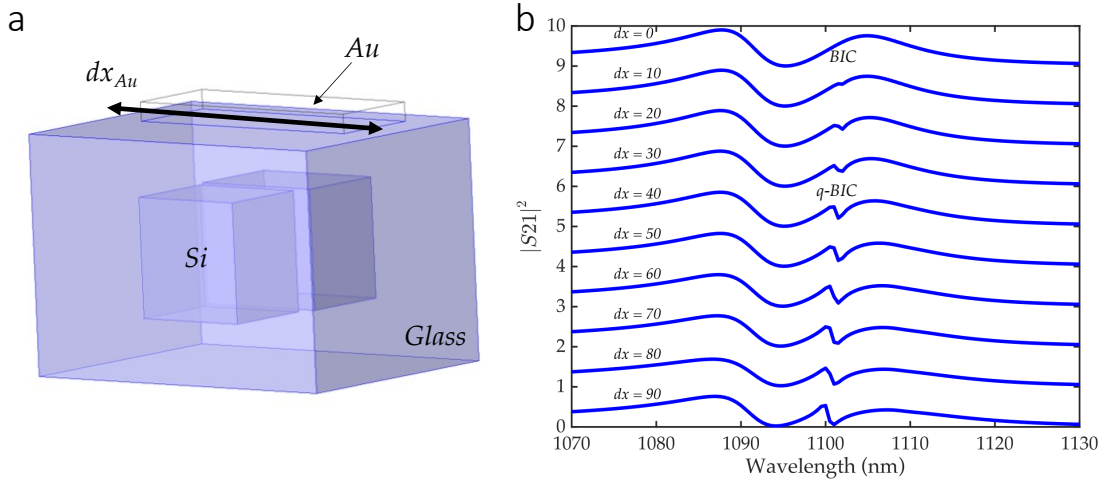
Figure 3.21: (a) Schematic of unit cell of the hybrid metasurface with gold bar shifts in x direction and $dy = 20$ nm. (b) Evolution of the transmission spectrum when increasing dx from 0 to 90 nm. Shift of the gold bar in x leads to hybrid-symmetry-breaking induced quasi-BIC.

BIC. In spectrum of Figure 3.21(b), $dx = 0$ there is a BIC and the photonics modes behave as unperturbed. And quasi-BIC peak gradually emerges with dx deviating from 0 to 90 nm. Asymmetry in y helps tailor plasmonics-photonics coupling to make up the asymmetry in the dielectric metasurface, forming the hybrid "symmetry" with no in-plane photonics symmetry required, while continuing to perturb in x direction again breaks this "symmetry" and results in the exposure of quasi-BIC involving interaction between plasmonics and photonics.

In addition to the BIC, it's fascinating to testify the possibility of realizing a hybrid plasmonics-photonics EP, where one photonics mode and one plasmonics mode share the same value of frequency and loss. Since the position shift of gold bar mainly affects the formation of BIC, parameters like asymmetric ratio and separation of silicon bars are utilized to fine tune resonance of photonics modes (Figure 3.22(a)). At $\alpha = 0.16$, by sweeping separation dy_{Si} and extracting from rational fitting, three eigenmodes and their frequencies (top) and losses (bottom) are plotted in Figure 3.22(b). It is observed that at $dy = 230$ nm, photonics (ph) mode 2 and plasmonics mode coalesce to one point with equal frequency and loss, which can be named as the plasmonics-photonics (pl-ph) EP. Usually, plasmonics mode features larger loss rate than photonics mode, so that formation of equal loss is very hard. Here the plasmonics mode has a frequency surge and then drops down, leading to the crossing with photonics mode 2. And for the loss trend, it first decreases and then increases, but always keeping a higher loss than the photonics modes except for the EP. Figure 3.22(c) plots the field distribution before EP and after EP for photonics mode 2 and plasmonics mode. From the mode distribution, the photonics or plasmonics mode cannot be classified
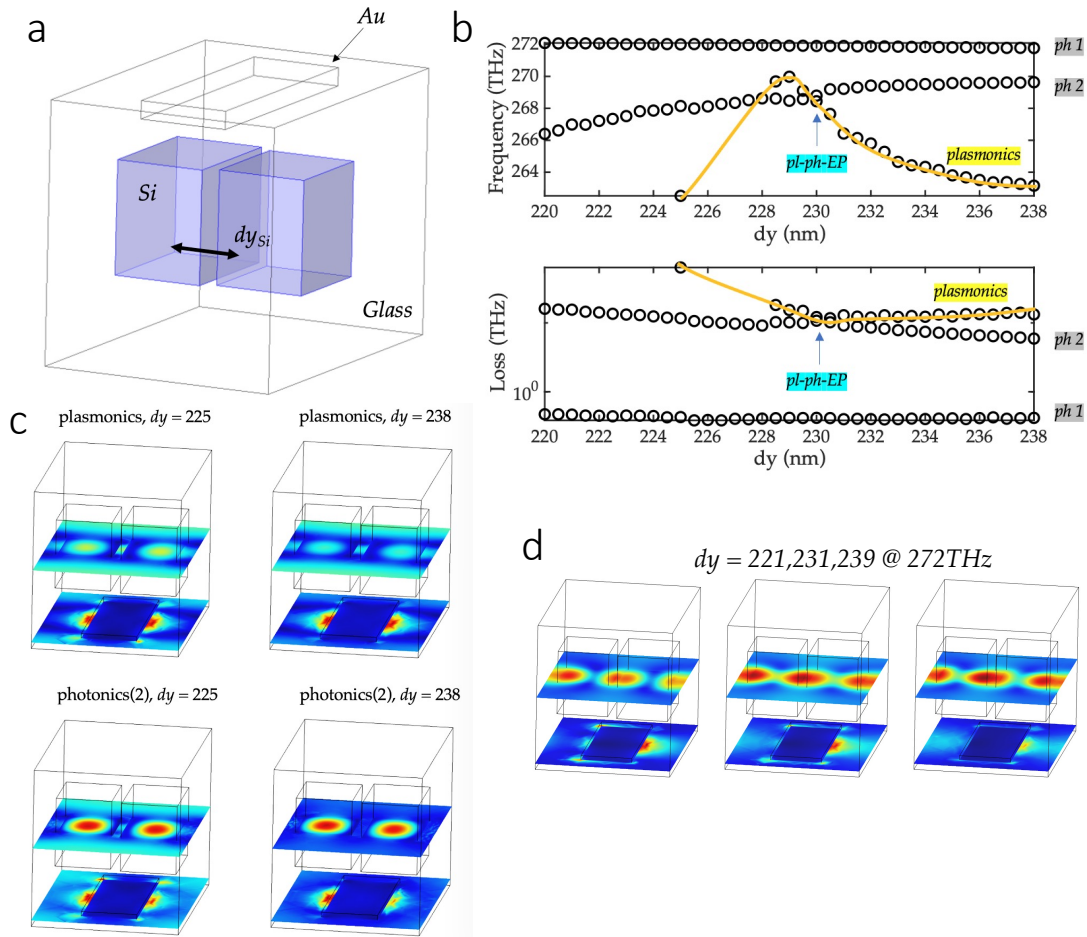
Figure 3.22: (a) Schematic of the unit cell of the metasurface for realizing hybrid plasmonics-photonics EP by fine tuning separation of silicon bars. (b) Extracted frequency (top) and loss (bottom, in log scale) of the three modes from rational fitting. Plasmonics-photonics (*pl-ph*) EP occurs at $dy = 230$ nm. Orange curve follows the trend of plasmonics mode. (c) Mode profile of the plasmonics mode and photonics mode 2 at $dy = 225$ nm and $dy = 238$ nm. (d) On-resonance mode profile of the photonics mode 1 at three different values of dy.

as a pure mode type, but a hybrid mode. For photonics mode 2, the resonance originates from silicon bars and then couples with gold bar, while for the plasmonics mode is induced by the gold bar, extending to the photonics mode. At EP, the two modes will be fully hybridized and equally dominant, and it's unable to distinguish the origin of each mode. Therefore, here the EP characterizes the maximum hybridization of photonics and plasmonics mode. Figure 3.22(b) also shows that the photonics mode 1 stays nearly unperturbed as a quasi-BIC mode by this hybrid coupling effect, as revealed by the smooth frequency and loss trend. Figure

3.22(d) demonstrates the filed distribution of this stable photonics mode, and the photonics quasi-BIC is induced in the glass and the gold bar shares an asymmetric mode profile.

In conclusion, by simply placing a metal bar on the dielectric metasurface, resonances from plasmonics mode and photonics mode are coupled and hybridized, leading to the generation of hybrid mode. Employing this plasmonics-photonics coupling effect, photonics BIC can be realized in the presence of silicon asymmetry, assisted by the plasmonics mode. Hybrid EIT and Fano lineshape is accompanied with slightly deviated from this BIC. Fine tuning of the dielectric arrangement results in a hybrid EP where the plasmonics mode and photonics mode coalesce to equal complex frequency. EP also indicates that hybridization among the two modes reaches the maximum. This study on special coupling conditions in plasmonics-photonics hybrid metasurfaces may contribute to development of hybrid sensors and lasers.

Chapter 4

Linear polarizer based on high contrast grating

4.1 Theoretical analysis of high contrast grating

Theoretical analysis of high contrast grating can be deemed as 1D periodic low-index and high-index region (waveguide array). The waveguide array structure in the x direction will allow several propagating modes in the high-index region [1, 7]. These modes are orthogonal without interaction and confined in the waveguides like optical cavities. At the top and bottom boundary planes, these array waveguide modes can couple to the plane waves and each other due to abrupt change in boundaries. When these modes are modes interfere with each other at the input/output planes, interesting phenomena will happen as the resonacnes in coupled cavities. Similar to a simple FP cavity, HCG supports a self-sustainable mode with the fulfilment of the round-trip condition. If the two modes interfere destructively/constructively at the HCG output plane, the transmission/reflection will then vanish, yielding 100% reflection/transmission. The high-transmission/reflection condition is different for TE and TM incident, thus contributing to the design of HCG polarizer.

4.2 Silicon nitride HCG

The HCG polarizer we investigate is based on the silicon nitride hosted by a glass substrate. It is selective for the transmission of TE or TM incident light, which can be characterized by the polarization extinction ratio (PER), definde as $PER = 10 \times \log\left(\dfrac{T_{TM}}{T_{TE}}\right)$ in dB scale. Figure 4.1 shows the schematic of a TM transmitted HCG polarizer.

HCG has a nature of polarization selective due to its 1D periodic along x axis and infinite in the y axis. Thus the incident wave will interact differently for the electrical field along x and y. This can be demonstrated by observing the $t_g - \lambda$ diagram of a typical HCG design, as shown in Figure 4.1. Under the operation wavelength of 940 nm (typical VCSEL
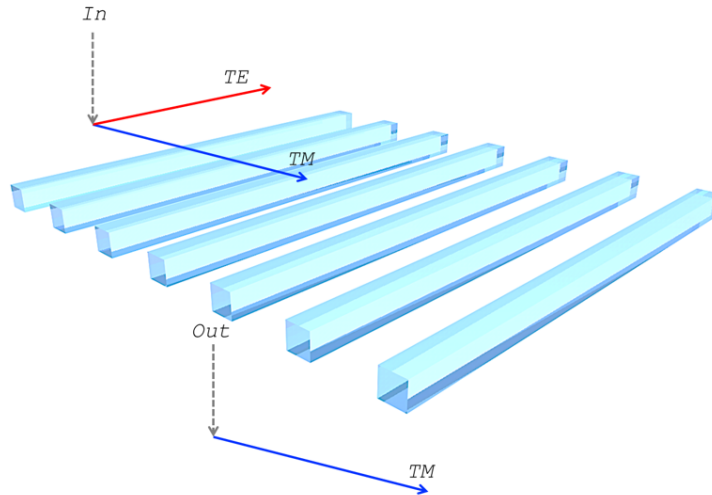
Figure 4.1: Schematic of a high contrast grating based linear polarizer for TM transmission and TE rejection.
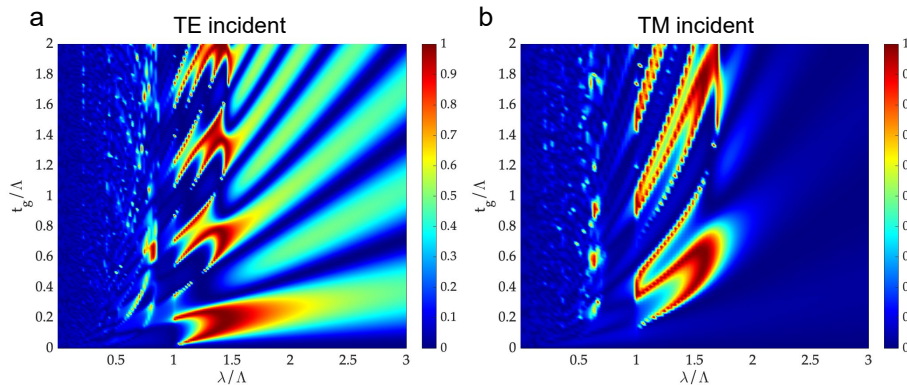
Figure 4.2: Transmission spectrum of a typical HCG at (a) TE and (b) TM incident.

wavelength), Figure 4.1(a) shows the transmission rate for TE incident wave and Figure 4.2(b) shows the TM transmission rate. Various designs can be accessed with high TE transmission and low TM transmission or vice versa.

Following the demonstrated polarization selective feature, the SiN HCG with high PER and high transmission can be realized in simulation. Figure 4.3(a,b) plot the PER and TM transmission as a function of duty cycle and HCG thickness. In Figure 4.3(a), the red region is good for TE polarizer and the blue region with negative PER is good for TM polarization. For TM operation, PER reaches over 60 dB and TM transmission is above 0.85, which is competitive for its performance. To inspect more carefully on the transmission selective
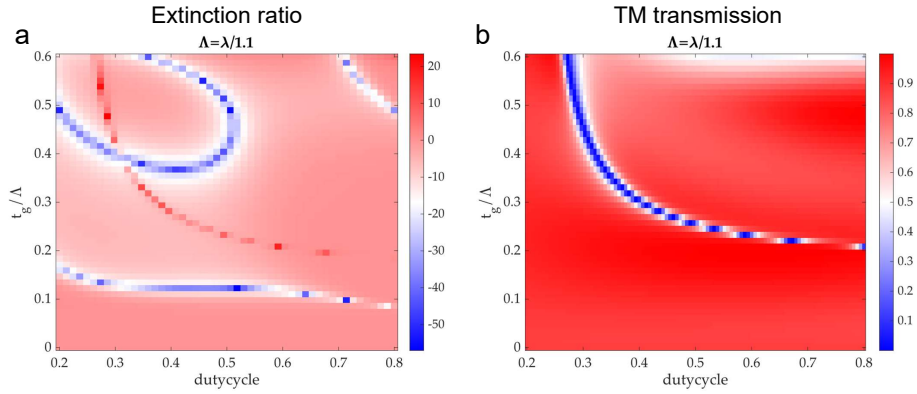
Figure 4.3: (a) PER as a function of duty cycle and thickness for SiN HCG with period of $\lambda/1.1$. (b) Corresponding TM transmission.
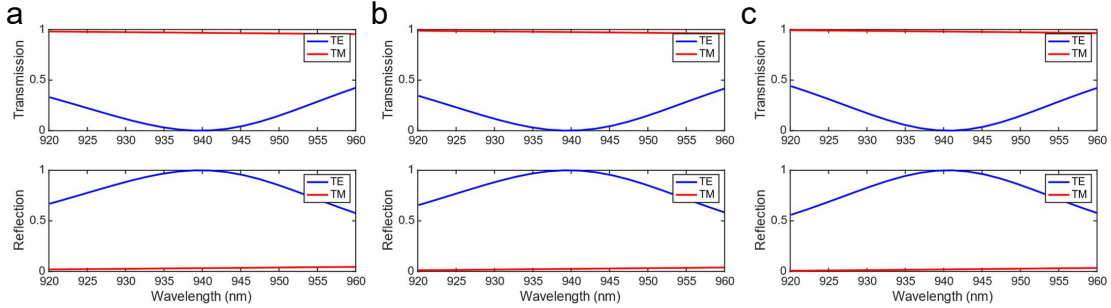
Figure 4.4: Transmission and reflection spectrum for SiN HCG polarizer with $t_g = 0.16\Lambda$. The duty cycle for (a-c) is 0.4, 0.46, 0.52, respectively.

feature of the SiN HCG, three designs at high PER region is selected and their corresponding transmission (reflection) spectrum is plotted in Figure 4.4. From the spectrum, the polarizer operates well at 940 nm, where a TE dip occurs with near-zero transmission and TM has nearly loseless transmission. This design is also very insensitive to change of duty cycle.

4.3 Metal grating with plasmonics resonance

Besides employing all-dielectric HCG, the possibility of metal grating for linear polarizer can be explored with the assistance of plasmonics resonances. There are two basic designs as shown in Figure 4.5. In the exposed design, the gold grating is surrounded by air and hosted by a glass substrate. And in the embedded case, the gold grating is coated by a host

material on the top, which can be different from the glass. The coating will contribute to other resonances, resulting in very different transmission spectrum for the two designs. Both designs have the desired polarizer performance for the large discrepancy in transmission.
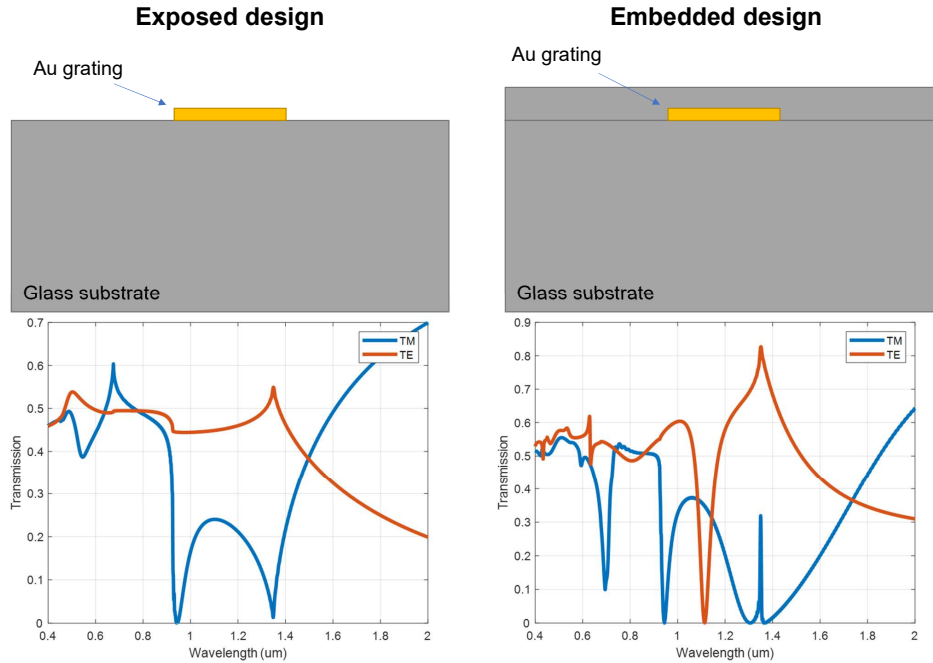
Figure 4.5: Exposed and embedded design for the Au grating polarizer. The gold grating is either exposed in the air ($n = 1$) or coated by other dielectric material. Below each design is the corresponding transmission spectrum for both TE and TM normal incident. The grating period is 925 nm with a bar width of 450 nm. The coating thickness is 60 nm at $n = 1.5$.

Figure 4.6 calculates the PER value for the two designs. In Figure 4.6(a), PER reaches over 35 dB around 940 nm and there is a second peak at 1350 nm, which corresponds to the two dips in TM transmission. While in Figure 4.6(b), PER can be larger than 50 dB with multiple peaks occurring, induced by the dip in TE mode and an induced-transparency lineshape around 1350 nm. The resonance dips can be tuned by controlling the period, bar width, top coating thickness and refractive index of the coating.

Over a broadband spectrum, the electric field profile is analyzed for the resonance dips in TM mode. For the one at shorter wavelength, a high-order mode is observed with the field showing multiple resonances around the metal grating. Typical plasmonics resonances
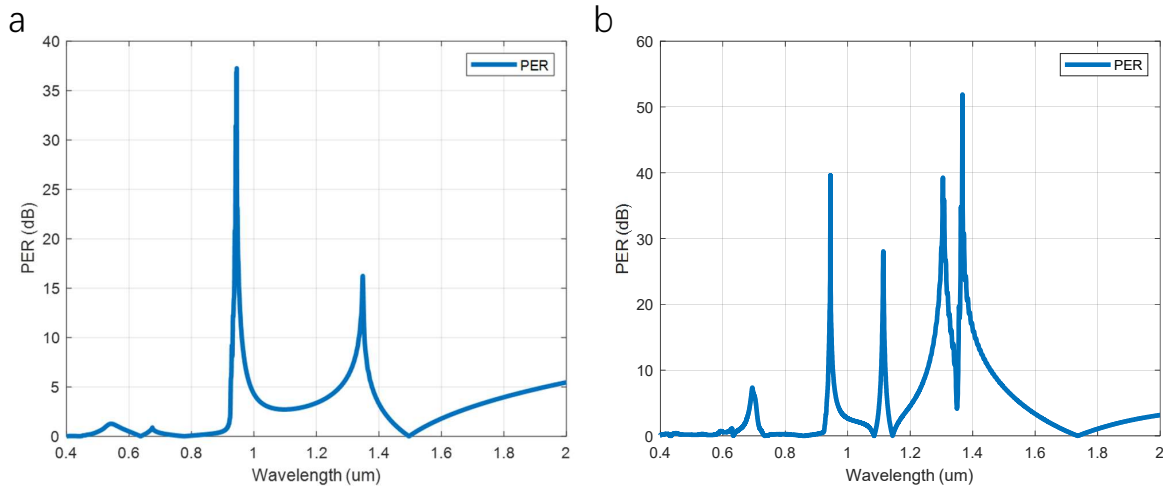
Figure 4.6: PER for the metal grating in (a) exposed design and (b) embedded design. The grating period is 925 nm with a bar width of 450 nm. The coating thickness is 60 nm at $n = 1.5$.
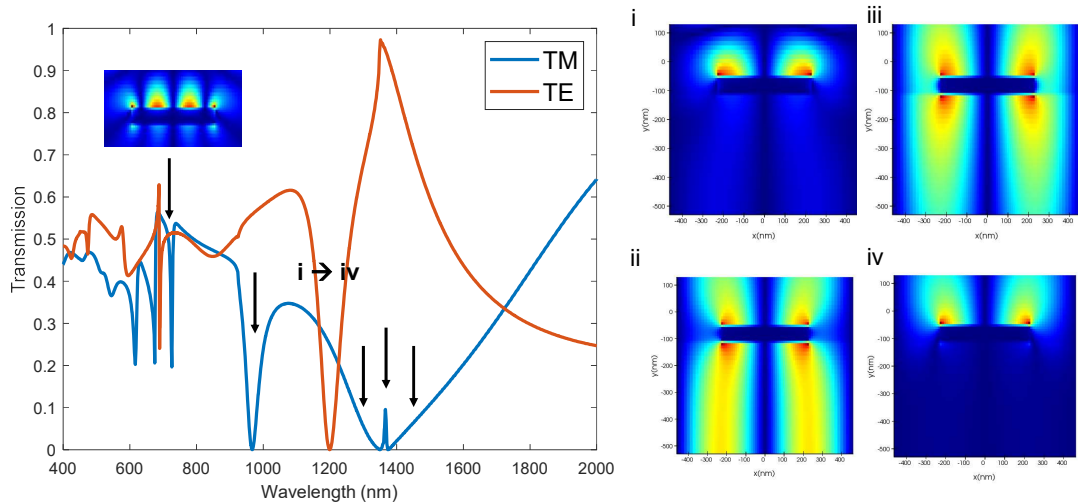
Figure 4.7: A broadband spectrum for embedded design with the top coating index at 1.6. Electric field distribution is plotted at dips in TE spectrum.

appears at i and iv, and field in ii, iii shows plasmonics modes coupled to the dielectric host and formation of photonics modes.

To decide on the parameters for fabrication, a sweep in period and bar width is conducted to evaluate the PER and passed transmission rate at 940 nm. Figure 4.8(a) shows the PER
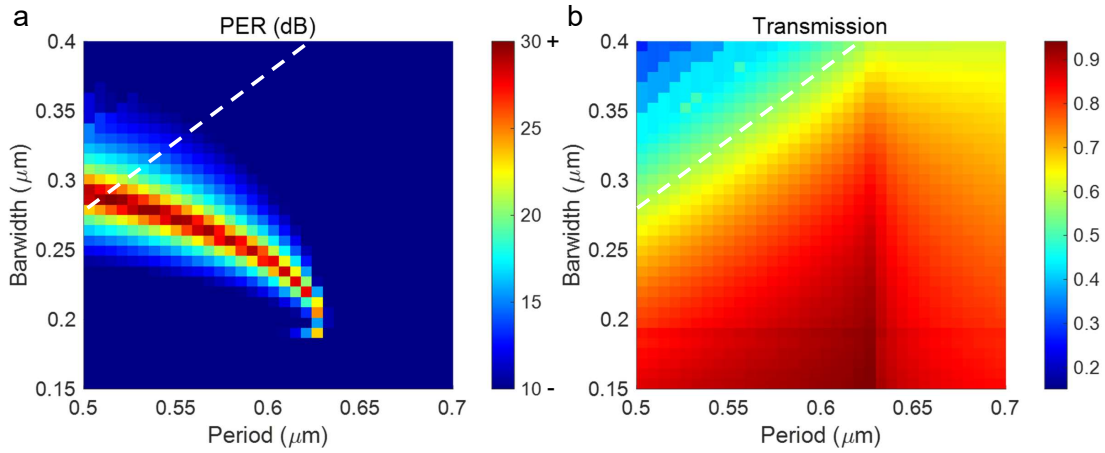
Figure 4.8: (a) PER and (b) passed transmission at 940 nm with sweep in period and bar width. The white dashed line is where the transmission is equal to 0.75.
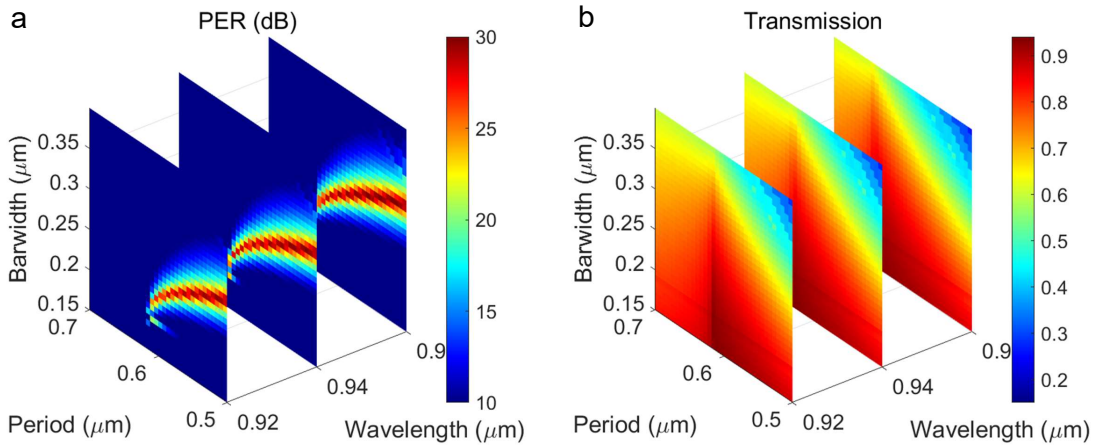
Figure 4.9: (a) PER and (b) passed transmission rate as a function of period and bar width at the wavelength of 920, 940, 960 nm.

as a function of period and bar width, and Figure 4.8(b) plots the corresponding passed transmission rate. The white dashed lines in both figures indicates a transmission rate of 0.75. Tolerance of employing gold grating can be further demonstrated from a wavelength view in Figure 4.9. Three slices at wavelength of 920, 940, and 960 nm shows the robustness of the high PER region, which does not shift much in the period-barwidth diagram. Thicker coating is also considered and leads to a Fano-like lineshape in the TM transmission as shown in Figure 4.10. As expected, increasing period from 600 to 700 nm results in a wavelength

shift. The broadband dip and asymmetric sharp dip in Figure 4.10(a) matches the two high-PER region in Figure 4.10(b). Fabrication of this metal grating can be done by choosing desired parameters and considering processing capability.
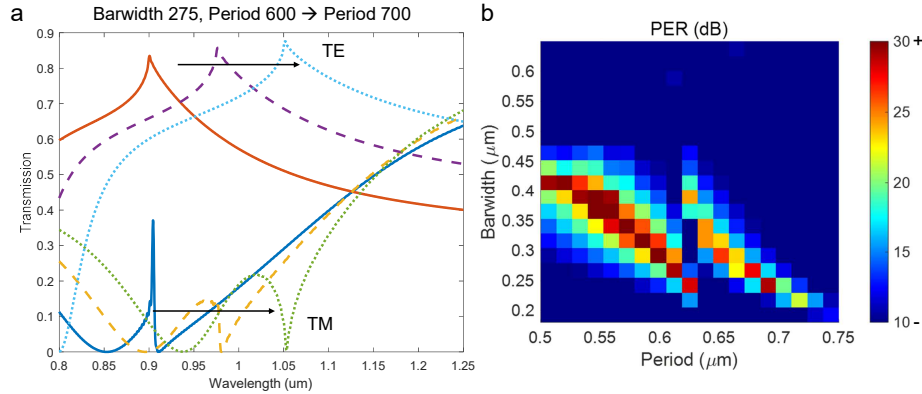
Figure 4.10: (a) Spectrum of gold grating with a coating thickness of 300 nm and refractive index of 1.5. The period ranges from 600 to 700 nm and the TM transmission shows Fano-like lineshape. (b) Sweep of period and bar width for high PER region.

4.4 Fabrication process and measurement

A full processing flow for the SiN HCG polarizer is shown in Figure 4.11. Fabrication of metal grating will involve lift-off process and is similar to the SiN one. To statr, the 6-inch glass wafer is cleaned with acetone and IPA to remove possible contamination. Then the SiN layer is deposited with a thickness of 350 nm using PECVD. Measurement under ellipsometer will be conducted to confirm the anticipated thickness and refractive index are reached. Before spin-coating of the photoresist, a thin layer of HDMS is coated on to the SiN to enhance adhesion of photoresist. With photoresist coated and baked, stepper is used to do photolithography. The next step is to develop the photoresist and move to RIE etch that etches down the exposed region of SiN. Finally, stripping with NMP is conducted to remove the remaining photoresist and additional O2 plasma can help clean the photoresist.

Figure 4.12 shows the HCG profile and cross-section view under SEM observation. Side wall and uniformity of the HCG meet expectation under this processing flow. A coarse measurement with microscope (Figure 4.13(a)) is conducted to test the polarization selective feature from these SiN HCG. The polarizer on the microscope is rotated by an angle of 90 degrees to observe the light intensity change on the CCD camera. Gray-scale value can be extracted with image processing software and averaged over a square region as shown in Figure 4.13(b,c). Then the transmission rate under each polarization state can be calculated and hence the PER. The resultant PER value is 20 dB for this specific sample. Although not
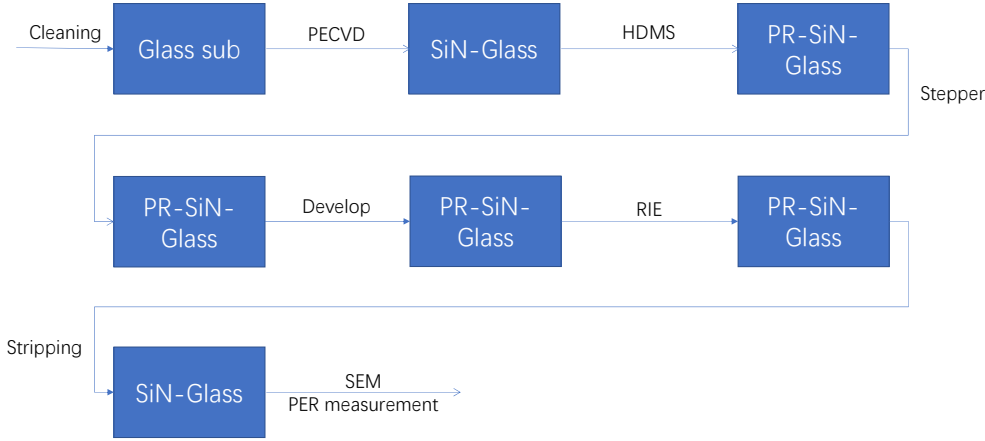
Figure 4.11: Flow chart for SiN HCG polarizer.
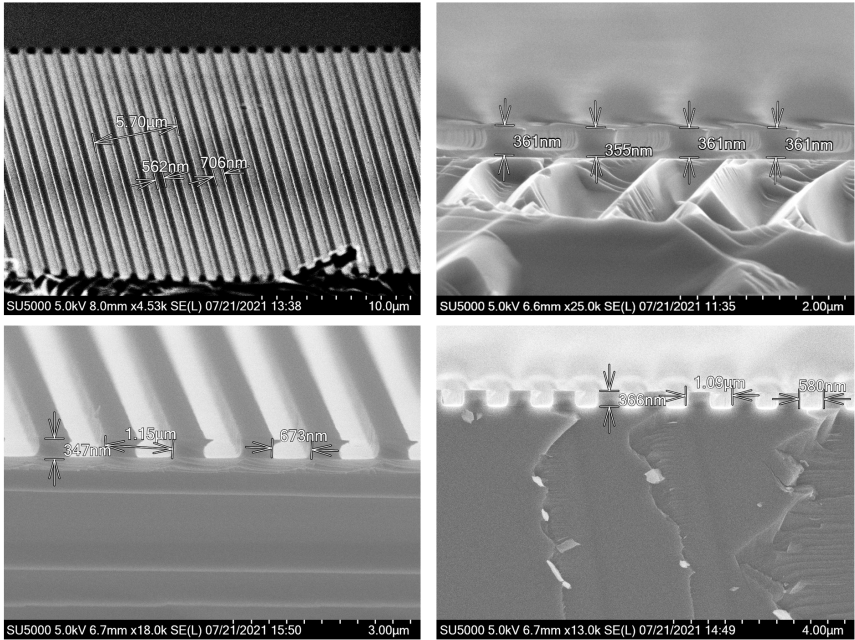
Figure 4.12: SiN HCG under SEM observation: profile and cross-section view.

a precise measurement, this method is fast and can be automated for large samples, and also provides a way to access the performance of HCG polarizer. Similarly, Figure 4.14 shows the measured PER and passed transmission rate for different designs on the glass wafer.
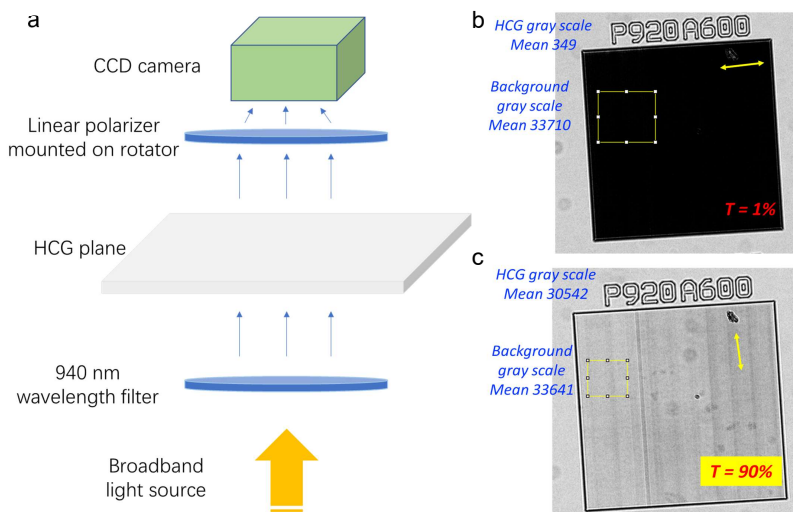
Figure 4.13: PER and transmission measurement of SiN HCG polarizer. (a) Schematic setup for the microscope incorporated with polarizer. (b) Microscopic image under TE detection. (c) Microscopic image under TM detection. The gray scale value is averaged over a rectangular region and the yellow arrows indicate the polarization state.
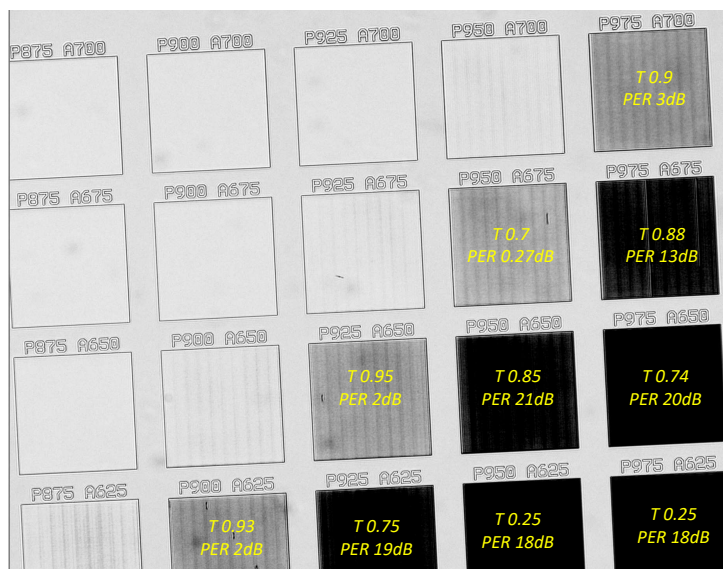
Figure 4.14: PER and transmission measurement of SiN HCG polarizer with different parameters on the glass wafer under microscope. The polarization is TE.

Chapter 5

Circular polarizer based on high contrast grating

5.1 HCG for polarization control

Polarization is an an essential property of light. The control of polarization is of broad scientific and technological interest for its applications in holography, structure light, imaging, and polarizers. The polarization state can be represented using polarization ellipse, in which the geometrical parameters of the ellipse, and its "handedness", is related with polarization state: the orientation angle, defined as the angle between the major axis of the ellipse and the x-axis, along with the ellipticity, the ratio of the ellipse's major to minor axis. To see the evolution of polarization state, Poincare sphere can be introduced where each point on the sphere represents a single polarization state. The Stokes vector can be easily converted to a state on the Poincare sphere. Due to the resonance induced phase and transmission difference for TE and TM incident, the output polarization state can be manipulated by just utilizing this 1D periodic structures in combination with rotation.

5.2 Simulation results

The basic principle of employing HCG as a circular polarizer is illustrated in Figure 5.1. An incident linearly polarized light can be decomposed into two orthogonally polarized light, i.e. x and y. When the intensity of transmitted light rate in x and y direction is the same, and the phase difference reaches 0.5π, the output light is a circular polarized light, with its direction depending on the sign of phase lag. For example, with a specific design of period $=$ 855 nm and duty cycle $= 0.55$, the transmission and phase for TE and TM can be calculated as shown in Figure 5.2(a). There are some points in phase that have a phase difference of 0.5π (the marker). The corresponding transmission is different for TE and TM, which indicates the incident light is not parallel to $\theta = 45°$. The calculated polarization angle is $\theta = \arctan(1.375) = 54°$. At this angle, the transmitted light will have the same amplitude
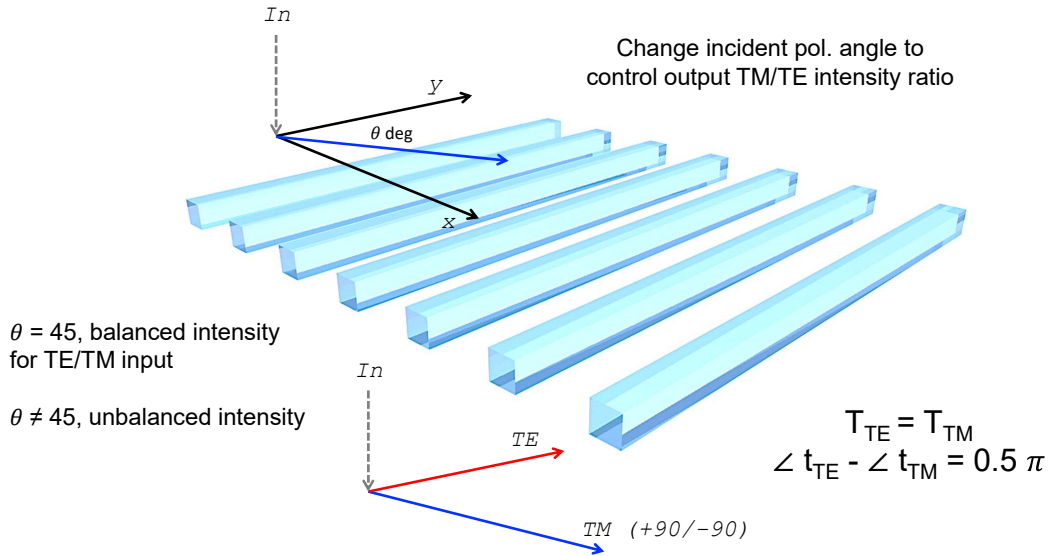
Figure 5.1: Schematic of a HCG circular polarizer. The incident light in linear polarization with an polarization angle of θ. The output circular polarization can be decomposed to TE and TM with the same amplitude but with a phase lag of $\pm 90°$.
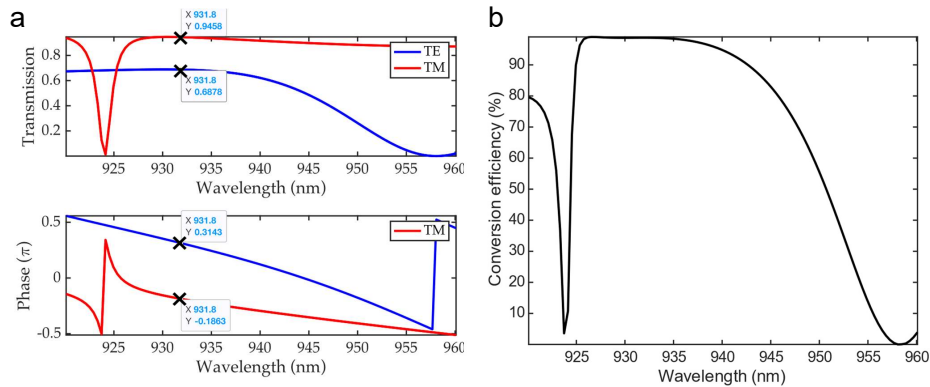
Figure 5.2: (a) Transmission and phase of TE and TM input for a HCG with period = 855 nm and duty cycle = 0.55. To fulfil the requirement for circular polarizer, the phase difference needs to be 0.5π and the incident polarization angle needs to compensate difference in transmission amplitude. (b) Corresponding conversion efficiency for circular polarizer over a wavelength domain. A 15 nm band with near-unity efficiency can be realized.

in both x and y direction, with a phase lag of 90 at the same time. The corresponding conversion efficiency that characterizes the portion of circularly polarized light in the output

is plotted in Figure 5.2(b), where near-unity efficiency can be realized over a span of 15 nm. Figure 5.3(a) evaluates another case with period of 950 nm and bar width of 300 nm. Figure
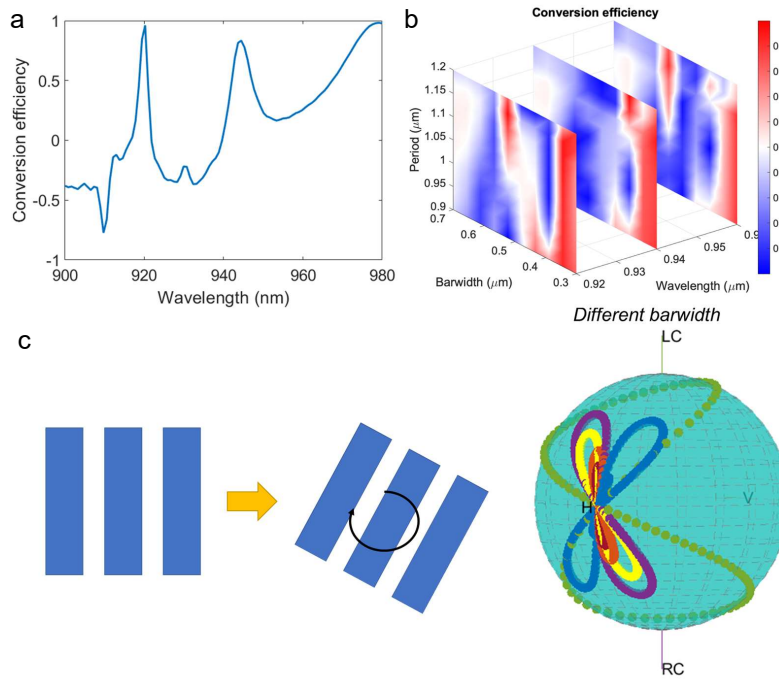
Figure 5.3: (a) Circular polarization conversion efficiency for a HCG with period of 950 nm and bar width of 300 nm. (b) Conversion efficiency as a function of period and bar width at different wavelength. (c) Rotation of the HCG profile results in an encircling effect in the polarization state on Poincare sphere. Different colors refer to different bar length.

5.3(b) plots the three wavelength slices at 920, 940, and 960 nm. The red region indicates a better performance for generation of circular polarization. In Figure 5.3(c), rotation of the grating plane leads to the change in output polarization state, as shown on the Poincare sphere, where the same color refers to one specific design. Rotation of 180° generates an "8"-like shape that centers a linear polarization point on the equator.

5.3 Perspective of flat-optics polarization control

It's interesting to note for HCG circular polarizers, when a mirror is placed after HCG to reflect circularly polarized light back on to HCG, the finally output light has different polarization state as shown in Figure 5.4. The comparison between input linear polarization and output linear polarization (two transmission of HCG and one reflection) is illustrated using polarization ellipse. For balanced TE/TM input, the input-output polarization is

orthogonal. While for unbalanced TE/TM input, the output polarization has some angle against the input state, but not at exact 45°. However, both operation can be employed as a optical isolator due to the difference in polarization angle.
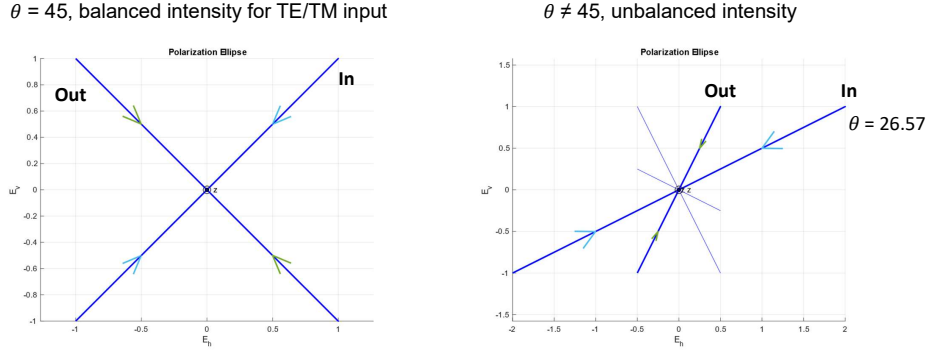
Figure 5.4: Input-output polarization state is given using polarization ellipse. For balanced TE/TM intensity, the input and output polarization are orthogonal. For unbalanced intensity, there is an angle between input and output state.

Apart from HCG, the birefringence metasurfaces play an important role in polarization control with more design capability and better performance. The birefringence metasurfaces are periodic in x, y direction, with the unit cell containing a silicon nanobar on the substrate. The lattice constant is 650 nm, and width, height of the bar is 180, 400 nm. The nanobar can be rotated by an angle of θ to tune its fast and slow axis. Employing this feature, full polarization generation may be possible by tuning the rotation angle (or the polarization angle of input light) and bar length. Figure 5.5(a) shows the output polarization state on a Poincare sphere when continuously changing the rotation angle of the nanobar. The input state is y polarized light with normal incident and at the angle of 79°, the output state becomes LCP. In Figure 5.5(b), different colors indicate different bar length, and each circle is induced by the rotation angle. As expected, full polarization state can be realized by tuning the two parameters of the birefringence metasurface. Similar principle can be applied to the oblique incident case.
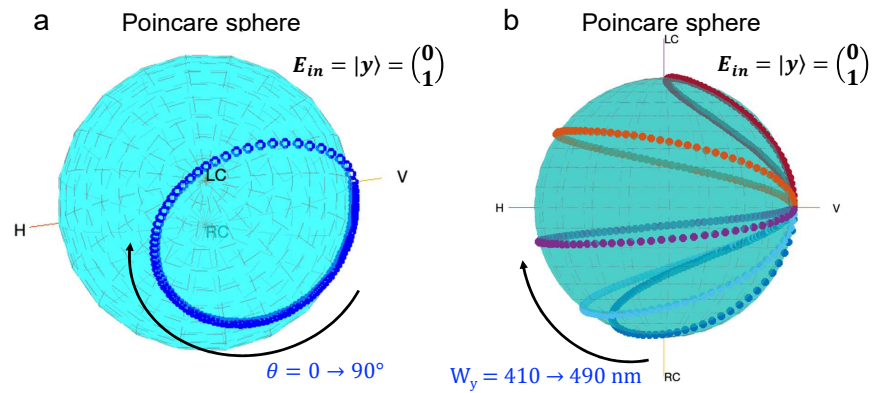
Figure 5.5: Output polarization state on the Poincare sphere of a birefringence metasurface. (a) Rotation of the nanobar results in the state encircling. (b) Changing both bar length and rotation angle can generate any arbitrary state.

Chapter 6

Conclusion

As a conclusion, this thesis investigates optical meta-structures for realization of exceptional points, bound States in the continuum, and polarization control. We employ asymmetry-induced quasi-BIC and thus enhanced field localization to enhance optical forces, chirality, and nonlinear harmonic generation. This kind of in-plane asymmetry is realized by making two bars in the unit cell different length, or etching cylindrical holes into the disk, which also can lead to chiral response. It's noteworthy that enhanced nonlinear chirality is also observed as illustrated with strikingly divergent second/third harmonic generation signals for LCP and RCP incident. For exploration of EPs, both EPs in transmission matrix and EPs in eigenmodes have been discussed. EP in an all-dielectric metasurface is applied for sensing in small index change and optical gyroscope with improved sensitivity. We also dive into the effects of hybrid modes for EPs and BICs where plasmonics modes and photonics modes couple with each other, leading to more possibilities in applications. For the work on HCG, both linear and circular HCG polarizers are designed with high extinction ration and high transmission. Plasmonics gratings have also been demonstrated their capability on polarization selection by taking advantage of plasmonics resonances. Full polarization control can be achieved with rotation of polarization angle or the HCG plane itself. We hope these studies and investigations may provide some insights into meta-structures and open new avenues towards applications and real-world devices.

Bibliography

[1]   Connie J Chang-Hasnain and Weijian Yang. "High-contrast gratings for integrated optoelectronics". en. In: *Advances in Optics and Photonics* 4.3 (2012), p. 379. DOI: 10.1364/AOP.4.000379. URL: https://www.osapublishing.org/aop/abstract.cfm?uri=aop-4-3-379.

[2]   Cheng-Wei Qiu et al. "Quo Vadis, Metasurfaces?" In: *Nano Letters* 21.13 (2021). PMID: 34157842, pp. 5461–5474. DOI: 10.1021/acs.nanolett.1c00828. eprint: https://doi.org/10.1021/acs.nanolett.1c00828. URL: https://doi.org/10.1021/acs.nanolett.1c00828.

[3]   Kane Yee. "Numerical solution of initial boundary value problems involving maxwell's equations in isotropic media". In: *IEEE Transactions on Antennas and Propagation* 14.3 (1966), pp. 302–307. DOI: 10.1109/TAP.1966.1138693.

[4]   Wikipedia contributors. *Finite-difference time-domain method — Wikipedia, The Free Encyclopedia*. [Online; accessed 19-October-2021]. 2021. URL: https://en.wikipedia.org/w/index.php?title=Finite-difference_time-domain_method&oldid=1038661340.

[5]   Hans-Jörg G. Diersch. "Fundamental Concepts of Finite Element Method (FEM)". In: *FEFLOW: Finite Element Modeling of Flow, Mass and Heat Transport in Porous and Fractured Media*. Berlin, Heidelberg: Springer Berlin Heidelberg, 2014, pp. 239–404. ISBN: 978-3-642-38739-5. DOI: 10.1007/978-3-642-38739-5_8. URL: https://doi.org/10.1007/978-3-642-38739-5_8.

[6]   Hou Tong Chen, Antoinette J. Taylor, and Nanfang Yu. "A review of metasurfaces: Physics and applications". In: *Reports on Progress in Physics* 79.7 (2016). ISSN: 00344885. DOI: 10.1088/0034-4885/79/7/076401. arXiv: 1605.07672.

[7]   Pengfei Qiao, Weijian Yang, and Connie J. Chang-Hasnain. "Recent advances in high-contrast metastructures, metasurfaces, and photonic crystals". In: *Adv. Opt. Photon.* 10.1 (Mar. 2018), pp. 180–245. DOI: 10.1364/AOP.10.000180. URL: http://www.osapublishing.org/aop/abstract.cfm?URI=aop-10-1-180.

[8]   Lingling Huang, Shuang Zhang, and Thomas Zentgraf. "Metasurface holography: from fundamentals to applications". In: *Nanophotonics* 7.6 (2018), pp. 1169–1190. DOI: doi:10.1515/nanoph-2017-0118. URL: https://doi.org/10.1515/nanoph-2017-0118.

[9]   Wei Ting Chen et al. "A broadband achromatic metalens for focusing and imaging in the visible". In: *Nature Nanotechnology* 13.3 (2018), pp. 220–226. ISSN: 17483395. DOI: 10.1038/s41565-017-0034-6. URL: http://dx.doi.org/10.1038/s41565-017-0034-6.

[10] Shuai Wang et al. "Arbitrary polarization conversion dichroism metasurfaces for all-in-one full Poincaré sphere polarizers". In: *Light: Science and Applications* 10.1 (2021). ISSN: 20477538. DOI: 10.1038/s41377-021-00468-y. URL: http://dx.doi.org/10.1038/s41377-021-00468-y.

[11] Zhuojun Liu et al. "High-Q Quasibound States in the Continuum for Nonlinear Metasurfaces". In: 253901 (2019), pp. 1–6. DOI: 10.1103/PhysRevLett.123.253901.

[12] Guixin Li, Shuang Zhang, and Thomas Zentgraf. "Nonlinear photonic metasurfaces". In: *Nature Reviews Materials* 2.5 (2017), pp. 1–14. ISSN: 20588437. DOI: 10.1038/natrevmats.2017.10. URL: http://dx.doi.org/10.1038/natrevmats.2017.10.

[13] Xuexue Guo et al. "Nonreciprocal metasurface with space–time phase modulation". In: *Light: Science and Applications* 8.1 (2019). ISSN: 20477538. DOI: 10.1038/s41377-019-0225-z. URL: http://dx.doi.org/10.1038/s41377-019-0225-z.

[14] Ying Li et al. "Transforming heat transfer with thermal metamaterials and devices". In: *Nature Reviews Materials* 6.6 (2021), pp. 488–507. ISSN: 20588437. DOI: 10.1038/s41578-021-00283-2. arXiv: 2008.07964. URL: http://dx.doi.org/10.1038/s41578-021-00283-2.

[15] Ashok Kodigala et al. "Lasing action from photonic bound states in continuum". In: *Nature* 541.7636 (2017), pp. 196–199. ISSN: 14764687. DOI: 10.1038/nature20799.

[16] Chia Wei Hsu et al. "Observation of trapped light within the radiation continuum". In: *Nature* 499.7457 (2013), pp. 188–191. ISSN: 00280836. DOI: 10.1038/nature12289.

[17] Kirill Koshelev, Andrey Bogdanov, and Yuri Kivshar. "Meta-optics and bound states in the continuum". In: *Science Bulletin* 64.12 (2019), pp. 836–842. ISSN: 20959281. DOI: 10.1016/j.scib.2018.12.003. arXiv: 1810.08698. URL: https://doi.org/10.1016/j.scib.2018.12.003.

[18] Andrey A. Bogdanov et al. "Bound states in the continuum and Fano resonances in the strong mode coupling regime". In: *Advanced Photonics* 1.01 (2019), p. 1. ISSN: 2577-5421. DOI: 10.1117/1.ap.1.1.016001. arXiv: 1805.09265.

[19] Kirill Koshelev et al. "Asymmetric Metasurfaces with High-Q Resonances Governed by Bound States in the Continuum". In: *Physical Review Letters* 121.19 (2018), p. 193903. ISSN: 10797114. DOI: 10.1103/PhysRevLett.121.193903. arXiv: 1809.00330. URL: https://doi.org/10.1103/PhysRevLett.121.193903.

[20] Shaimaa I. Azzam et al. "Formation of Bound States in the Continuum in Hybrid Plasmonic-Photonic Systems". In: *Phys. Rev. Lett.* 121 (25 Dec. 2018), p. 253901. DOI: 10.1103/PhysRevLett.121.253901. URL: https://link.aps.org/doi/10.1103/PhysRevLett.121.253901.

[21] Lujun Huang et al. "Sound trapping in an open resonator". In: *Nature Communications* 12.1 (2021), pp. 1–7. ISSN: 20411723. DOI: `10.1038/s41467-021-25130-4`. arXiv: `2103.11581`. URL: `http://dx.doi.org/10.1038/s41467-021-25130-4`.

[22] Kenneth B. Crozier. "Quo vadis, plasmonic optical tweezers?" In: *Light: Science and Applications* 8.1 (2019), pp. 4–9. ISSN: 20477538. DOI: `10.1038/s41377-019-0146-x`. URL: `http://dx.doi.org/10.1038/s41377-019-0146-x`.

[23] Hongbao Xin and Baojun Li. "Fiber-based optical trapping and manipulation". In: *Frontiers of Optoelectronics* 12.1 (2019), pp. 97–110. ISSN: 20952767. DOI: `10.1007/s12200-017-0755-z`.

[24] Ognjen Ilic and Harry A. Atwater. "Self-stabilizing photonic levitation and propulsion of nanostructured macroscopic objects". In: *Nature Photonics* 13.4 (2019), pp. 289–295. ISSN: 17494893. DOI: `10.1038/s41566-019-0373-y`.

[25] Harry A. Atwater et al. "Materials challenges for the Starshot lightsail". In: *Nature Materials* 17.10 (2018), pp. 861–867. ISSN: 14764660. DOI: `10.1038/s41563-018-0075-8`. URL: `http://dx.doi.org/10.1038/s41563-018-0075-8`.

[26] Daniel Andrén et al. "Microscopic metavehicles powered and steered by embedded optical metasurfaces". In: *Nature Nanotechnology* 16.9 (2021), pp. 970–974. ISSN: 17483395. DOI: `10.1038/s41565-021-00941-0`. arXiv: `2012.10205`.

[27] Ming Liu et al. "Light-driven nanoscale plasmonic motors". In: *Nature Nanotechnology* 5.8 (2010), pp. 570–573. ISSN: 17483395. DOI: `10.1038/nnano.2010.128`. URL: `http://dx.doi.org/10.1038/nnano.2010.128`.

[28] Leilei Xu et al. "Light-driven micro/nanomotors: From fundamentals to applications". In: *Chemical Society Reviews* 46.22 (2017), pp. 6905–6926. ISSN: 14604744. DOI: `10.1039/c7cs00516d`. URL: `http://dx.doi.org/10.1039/c7cs00516d`.

[29] Peter T. Rakich, Miloš A. Popovic, and Zheng Wang. "General treatment of optical forces and potentials in mechanically variable photonic systems". In: *Optics Express* 17.20 (2009), p. 18116. ISSN: 1094-4087. DOI: `10.1364/oe.17.018116`.

[30] Zhanghua Han et al. "Significantly enhanced second-harmonic generations with all-dielectric antenna array working in the quasi-bound states in the continuum and excited by linearly polarized plane waves". In: *Nanophotonics* 10.3 (2021), pp. 1189–1196.

[31] Can Huang et al. "Ultrafast control of vortex microlasers". In: *Science* 367.6481 (2020), pp. 1018–1021. ISSN: 10959203. DOI: `10.1126/science.aba4597`.

[32] Zhanghua Han and Yangjian Cai. "All-optical self-switching with ultralow incident laser intensity assisted by a bound state in the continuum". In: *Opt. Lett.* 46.3 (Feb. 2021), pp. 524–527. DOI: `10.1364/OL.415531`. URL: `http://www.osapublishing.org/ol/abstract.cfm?URI=ol-46-3-524`.

[33] Kristina Frizyuk et al. "Nonlinear Circular Dichroism in Mie-Resonant Nanoparticle Dimers". In: *Nano Letters* 21.10 (2021), pp. 4381–4387. ISSN: 15306992. DOI: `10.1021/acs.nanolett.1c01025`. arXiv: `2103.10544`.

[34] Robert W. Boyd. "Chapter 1 - The Nonlinear Optical Susceptibility". In: *Nonlinear Optics (Third Edition)*. Ed. by Robert W. Boyd. Third Edition. Burlington: Academic Press, 2008, pp. 1–67. ISBN: 978-0-12-369470-6. DOI: `https://doi.org/10.1016/B978-0-12-369470-6.00001-0`. URL: `https://www.sciencedirect.com/science/article/pii/B9780123694706000010`.

[35] Attilio Zilli et al. "Frequency Tripling via Sum-Frequency Generation at the Nanoscale". In: *ACS Photonics* 8.4 (2021), pp. 1175–1182. DOI: `10.1021/acsphotonics.1c00112`. eprint: `https://doi.org/10.1021/acsphotonics.1c00112`. URL: `https://doi.org/10.1021/acsphotonics.1c00112`.

[36] Ramy El-Ganainy et al. "The dawn of non-Hermitian optics". In: *Communications Physics* 2.1 (2019), pp. 1–5. ISSN: 23993650. DOI: `10.1038/s42005-019-0130-z`. URL: `http://dx.doi.org/10.1038/s42005-019-0130-z`.

[37] Mohammad Ali Miri and Andrea Alù. "Exceptional points in optics and photonics". In: *Science* 363 (2019), eaar7709. ISSN: 10959203. DOI: `10.1126/science.aar7709`. URL: `http://science.sciencemag.org/`.

[38] K. Özdemir et al. "Parity–time symmetry and exceptional points in photonics". In: *Nature Materials* 18.8 (2019), pp. 783–798. ISSN: 14764660. DOI: `10.1038/s41563-019-0304-9`. URL: `http://dx.doi.org/10.1038/s41563-019-0304-9`.

[39] Weijian Chen et al. "Exceptional points enhance sensing in an optical microcavity". In: *Nature* 548.7666 (2017), pp. 192–195. ISSN: 14764687. DOI: `10.1038/nature23281`. URL: `http://dx.doi.org/10.1038/nature23281`.

[40] Jan Wiersig. "Review of exceptional point-based sensors". In: *Photonics Research* 8.9 (2020), p. 1457. ISSN: 2327-9125. DOI: `10.1364/prj.396115`.

[41] Adi Pick et al. "Enhanced nonlinear frequency conversion and Purcell enhancement at exceptional points". In: *Physical Review B* 96.22 (2017), pp. 1–7. ISSN: 24699969. DOI: `10.1103/PhysRevB.96.224303`. arXiv: `1705.07390`.

[42] Xu Lin Zhang, Tianshu Jiang, and C. T. Chan. "Dynamically encircling an exceptional point in anti-parity-time symmetric systems: asymmetric mode switching for symmetry-broken modes". In: *Light: Science and Applications* 8.1 (2019). ISSN: 20477538. DOI: `10.1038/s41377-019-0200-8`. URL: `http://dx.doi.org/10.1038/s41377-019-0200-8`.

[43] Jörg Doppler et al. "Dynamically encircling an exceptional point for asymmetric mode switching". In: *Nature* 537.7618 (2016), pp. 76–79. ISSN: 14764687. DOI: `10.1038/nature18605`. URL: `http://dx.doi.org/10.1038/nature18605`.

[44] Qinghua Song, Mutasem Odeh, and Patrice Genevet. "Plasmonic topological metasurface by encircling an exceptional point". In: *Science* 1137.September (2021), pp. 1133–1137.

[45] Hossein Hodaei et al. "Enhanced sensitivity at higher-order exceptional points". In: *Nature* 548.7666 (2017), pp. 187–191. ISSN: 14764687. DOI: 10.1038/nature23280. URL: http://dx.doi.org/10.1038/nature23280.

[46] Weijian Chen et al. "Parity-time-symmetric whispering-gallery mode nanoparticle sensor [Invited]". In: *Photonics Research* 6.5 (2018), A23. ISSN: 2327-9125. DOI: 10.1364/prj.6.000a23.

[47] Mohammad P. Hokmabadi et al. "Non-Hermitian ring laser gyroscopes with enhanced Sagnac sensitivity". In: *Nature* 576.7785 (2019), pp. 70–74. ISSN: 14764687. DOI: 10.1038/s41586-019-1780-4.

[48] Yu Hung Lai et al. "Observation of the exceptional-point-enhanced Sagnac effect". In: *Nature* 576.7785 (2019), pp. 65–69. ISSN: 14764687. DOI: 10.1038/s41586-019-1777-z. URL: http://dx.doi.org/10.1038/s41586-019-1777-z.

[49] Jun Hee Park et al. "Symmetry-breaking-induced plasmonic exceptional points and nanoscale sensing". In: *Nature Physics* 16.4 (2020), pp. 462–468. ISSN: 17452481. DOI: 10.1038/s41567-020-0796-x. URL: http://dx.doi.org/10.1038/s41567-020-0796-x.

[50] Yanxian Wei et al. *Chiral polarizer based on encircling EP*. 2021. arXiv: 2109.14352 [physics.optics].

[51] P. Djorwe, Y. Pennec, and B. Djafari-Rouhani. "Exceptional Point Enhances Sensitivity of Optomechanical Mass Sensors". In: *Phys. Rev. Applied* 12 (2 Aug. 2019), p. 024002. DOI: 10.1103/PhysRevApplied.12.024002. URL: https://link.aps.org/doi/10.1103/PhysRevApplied.12.024002.

[52] Fabrizio Minganti et al. "Quantum exceptional points of non-Hermitian Hamiltonians and Liouvillians: The effects of quantum jumps". In: *Phys. Rev. A* 100 (6 Dec. 2019), p. 062131. DOI: 10.1103/PhysRevA.100.062131. URL: https://link.aps.org/doi/10.1103/PhysRevA.100.062131.

[53] Yao Liang et al. "Bound states in the continuum in anisotropic plasmonic metasurfaces". In: *Nano Letters* 20.9 (2020), pp. 6351–6356. ISSN: 15306992. DOI: 10.1021/acs.nanolett.0c01752.

[54] Rupert F. Oulton et al. "Plasmon lasers at deep subwavelength scale". In: *Nature* 461.7264 (2009), pp. 629–632. ISSN: 00280836. DOI: 10.1038/nature08364.

[55] Yin Liang et al. "Plasmonic Nanolasers in On-Chip Light Sources: Prospects and Challenges". In: *ACS Nano* 14.11 (2020). PMID: 33119269, pp. 14375–14390. DOI: 10.1021/acsnano.0c07011. eprint: https://doi.org/10.1021/acsnano.0c07011. URL: https://doi.org/10.1021/acsnano.0c07011.

[56]   Shaimaa I. Azzam et al. "Ten years of spasers and plasmonic nanolasers". In: *Light: Science and Applications* 9.1 (2020). ISSN: 20477538. DOI: 10.1038/s41377-020-0319-7. URL: http://dx.doi.org/10.1038/s41377-020-0319-7.